Summer 2016

Evaluation of 4h-Sic Photoconductive Switches for Pulsed Power Applications Based on Numerical Simulations

Rajintha Tiskumara
Old Dominion University, rtisk001@odu.edu

EVALUATION OF 4H-SIC PHOTOCONDUCTIVE SWITCHES FOR PULSED POWER APPLICATIONS BASED ON NUMERICAL SIMULATIONS

by

Rajintha Tiskumara
B.S. in Physics, July 2010, University of Peradeniya, Sri Lanka
M.S. in Physics, May 2013, Old Dominion University

A Thesis Submitted to the Faculty of Old Dominion University
in Partial Fulfillment of the Requirements for the Degree of

DOCTOR OF PHILOSOPHY

ELECTRICAL AND COMPUTER ENGINEERING

OLD DOMINION UNIVERSITY
August 2016

Approved by:

Ravindra Joshi (Director)

Linda Vahala (Member)

Jiang Li (Member)

Duc Nguyen (Member)

ABSTRACT

EVALUATION OF 4H-SIC PHOTOCONDUCTIVE SWITCHES

FOR PULSED POWER APPLICATIONS

BASED ON NUMERICAL SIMULATIONS

Rajintha Tiskumara
Old Dominion University, 2016
Director: Dr. Ravindra Joshi

Since the early studies by Auston, photoconductive semiconductor switches (PCSSs) have been investigated intensively for many applications owing to their unique advantages over conventional gas and mechanical switches. These advantages include high speeds, fast rise times, optical isolation, compact geometry, and negligible jitter. Another important requirement is the ability to operate at high repetition rates with long device lifetimes (i.e., good reliability without degradation). Photoconductive semiconductor switches (PCSSs) are low-jitter compact alternatives to traditional gas switches in pulsed power systems. The physical properties of Silicon Carbide (SiC), such as a large bandgap (3.1-3.35 eV), high avalanche breakdown field (~3 MV/cm), and large thermal conductivity (4-5 W/cm-K) with superior radiation hardness and resistance to chemical attack, make SiC an attractive candidate for high voltage, high temperature, and high power device applications.

A model-based analysis of the steady-state, current-voltage response of semi-insulating 4H-SiC was carried out to probe the internal mechanisms, focusing on electric field driven effects. Relevant physical processes, such as multiple defects, repulsive potential barriers to electron trapping, band-to-trap impact ionization, and field-dependent detrapping, were comprehensively included. Results of our model matched the available experimental data fairly

well over orders of magnitude variation in the current density. A number of important parameters were also extracted in the process through comparisons with available data. Finally, based on our analysis, the possible presence of holes in the samples could be discounted up to applied fields as high as 275 kV/cm.

In addition, calculations of electric field distributions in a SiC photoconductive semiconductor switch structure with metal contacts employing contact extensions on a high-*k* HfO_2 dielectric were carried out, with the goal of assessing reductions in the peak electric fields. For completeness, analysis of thermal heating in a lateral PCSS structure with such modified geometries after photoexcitation was also included.

The simulation results of the electric field distribution show that peak electric fields, and hence the potential for device failure, can be mitigated by these strategies. A combination of the two approaches was shown to produce up to a ~67% reduction in peak fields. The reduced values were well below the threshold for breakdown in SiC material using biasing close to experimental reports. The field mitigation was shown to depend on the length of the metal overhang. Further, the calculations show that, upon field mitigation, the internal temperature rise would also be controlled. A maximum value of 980 K was obtained here for an 8 ns electrical pulse at a 20 kV external bias, which is well below the limits for generating local stress or cracks or defects.

I dedicate this dissertation to the God, my advisor, and my family,
for all the blessings, strength, guidance, and support.

ACKNOWLEDGMENTS

I would like to first thank my research advisor, Dr. Ravindra Joshi, for all of the advice, guidance, and patience extended to me in the past several years. This work would not have been possible without his constant direction and motivation. I am also grateful to my dissertation committee members, Dr. Linda Vahala, Dr. Jiang Li, and Dr. Duc Nguyen, for their help, comments, and suggestions during my research.

I truly appreciate my family for believing in me and for giving me strength to keep working. I thank my parents for giving me a luxurious life and for their blessings with endless love. I know it has been hard for you to not to have me by your side, all of these years. I can never thank you enough for the sacrifices you had to make along the way to get me where I am today. I also want to thank my sisters for encouraging and helping me. A very special thank goes to Jayendrika, my sister, for all the love, care, and tolerance, and for being the best friend and the best roommate I could ask for.

I would like to express my gratitude to Dr. Lepsha Vuskovic, the Graduate Program Director, Department of Physics at ODU and to Dr. Svetozar Popovic for their invaluable support, guidance and advice given, since the day I started my graduate studies at ODU.

I am sincerely thankful to Interim Provost and President for Academic Affairs at Old Dominion, Dr. Chandra De Silva, for taking time out of his busy schedule to help me.

To the staff, faculty and graduate students at the Department of Electrical and Computer Engineering and also at the Department of Physics at ODU, thank you for your support and encouragement throughout the last few years.

I would like to extend my sincere gratitude to my undergraduate research advisor, Dr.

Frank Peiris, for providing me with continuous guidance in pursuing further studies as an academic researcher. Furthermore, the entire faculty at University of Peradeniya should be acknowledged for the support and encouragement provided at the undergraduate level which in turn inspired me to pursue graduate studies.

I thank Dr. Earl Godfrey and Dianne Godfrey for making me a home away from home. You both were there guiding me, strengthening me, and helping through even in the rough times, like my own parents. I will be forever grateful to you for your love, caring, and support. I am really thankful that I met you during this journey.

I am particularly grateful to my cousin Deepi and her husband Prashantha Ratnayake for their support in the pursuit of my dreams since the day I first came to the US. Thank you for advising me and supporting me and also for mentoring me to pass through the hard times.

I really am thankful to my dearest friend, Sean, for being there for me through thick and thin and also for being my pillar of support. I know I wouldn't have achieved this without you. Thank you for strengthening me, for pushing me to perform my very best in everything I do, for encouraging me, and especially for your patience.

Big thanks to Kurnia, Tasnuva, and Grace for encouraging me and being extremely supportive, each time I needed help. I especially thank Tasnuva for standing beside me through all the difficult times and being there for me, when I was in need of some good moral support.

I would like to thank all of my Sri Lankan friends in Hampton Roads, including Dasuni, Duminda, and Hashir for helping me since the day I first came to Norfolk. I also want to take this chance to thank Rajiv Ranasinghe for his guidance. Last but not least, I would like to thank each person who has helped me in any way throughout this journey. Thank you all.

TABLE OF CONTENTS

Page

LIST OF TABLES ix

LIST OF FIGURES x

Chapter

1. INTRODUCTION 1
    1.1 Motivation 1
    1.2 The Scope and the Organization of the dissertation 10

2. BACKGROUND AND LITERATURE REVIEW 12
    2.1 Introduction 12
    2.2 Photoconductivity and basic concepts 13
    2.3 Photoconductive semiconductor switches 20
    2.4 Classification of photoconductive semiconductor switches 24
    2.5 Photoconductive materials 30
    2.6 Transport in semi-insulating materials 44
    2.7 Other relevant issues for photoconductive switching 49

3. SIMULATION METHODS FOR PHOTOCONDUCTIVE SWITCH ANALYSES. 57
    3.1 Model analyses 57
    3.2 Mathematical model for one-dimensional (1-D) analysis 62
    3.3 Numerical implementation for drift-diffusion analysis 68
    3.4 COMSOL computation for inclusion of multi-dimensional and thermal analysis 75

4. RESULTS AND DISCUSSION 81
    4.1 Introduction 81
    4.2 Simulation results of steady state current-voltage response 81
    4.3 Simulations with high-k dielectrics and metal overhang in SiC samples 92

5. CONCLUSIONS AND SCOPE FOR FUTURE WORK 104
    5.1 Conclude Summary 104
    5.2 Scope for Future Work 106

REFERENCES 108

APPENDICES …… 120

VITA 122

LIST OF TABLES

Table		Page
2.1.	Properties of Si at 300 K	36
2.2.	Properties of GaAs at 300 K	38
2.3.	Comparison of the physical properties of Si, GaAs and SiC	39
2.4.	Some parameters of SiC polytypes	39
2.5.	Some parameters of GaN and SiC polytypes	42
3.1.	The parameters used in the simulation	70
4.1.	Simulation results for the trap densities and the locations below the conduction band-edge	83
4.2.	Impact-ionization parameters for the three traps	84

LIST OF FIGURES

Figure Page

1.1 The experimental J-F characteristics obtained for semi-insulating 4H-SiC photoconductive devices. Solid line is for sample SiC1, taken from a set of samples that were electron-beam irradiated; while dashed line is for sample SiC2 that was not irradiated 4

1.2. Schematic of the geometries of the 4H-SiC PCSS used in the simulations. (a) Basic geometry. (b) Mesa structure with metal extensions at both the anode and cathode ends, and (c) a similar PCSS mesa structure with metal overhang over HfO_2 material, (d) metal extensions over a thin HfO_2 layer that spans the entire length between the two electrodes.....8

2.1. Schematic diagram of the photoexcitation and photoionization processes 16

2.2. A direct transition from the valence band (VB) to the conduction band (CB) due to an absorption of a photon.....17

2.3. Schematic diagram of the indirect transition across the bandgap involve phonon 17

2.4. Mechanisms of electron-hole pair generation induced by absorption of a subband-gap photon, mediated by localized band-gap states 19

2.5. PCSS schematic showing the current, *I(t)*, applied voltage and device dimensions 22

2.6. Lateral geometry PCSSs 27

2.7. Vertical geometry PCSSs.....28

2.8. Lattice arrangement of different polytypes.....40

2.9. I-V characteristics for a deep (left) and shallow trap (right) respectively 47

2.10. Analysis model of a RCE photodetector. The active region of thickness “d” is a small bandgap semiconductor. The top and bottom distributed Bragg reflection mirrors consist of alternating layers of non-absorbing larger bandgap materials.....54

2.11. Wavelength dependence of η for RCE device having various top mirror reflectivities for fixed $L=2\ \mu m$, $R_2=0.9$ and $\alpha L=0$.....55

3.1. Schematic diagram showing the electroluminescence due to the impact ionization. (a) Impact ionization produces a new electron-hole pair; (b) the hole can recombine with an electron in an acceptor state; (c) the electron may then fall into this empty acceptor state, and

this results the radiative emission 60

3.2. Diagram of Anode hole injection process. An incident tunneling electron arrives at the anode with energy E_{gain} to thermalize. This energy is transferred to a deep valence band electron, thereby exciting it to the lowest available energy state, the anode conduction band 62

3.3. Numerical computation for the steady state analysis.....68

3.4. Schematic diagram of the 1-D 4H-SiC 69

3.5. Schematic diagrams illustrating the variation of potential energy of (a) Coulombic attractive center, (b) Coulombic neutral center, and (c) Coulombic repulsive center 71

3.6. Schematic diagram illustrating the Poole-Frenkel effect.....72

3.7. Energy diagram of the trapping center in the presence of the electric field. Arrows indicate the possible electron emission mechanisms: PF represents the thermal ionization over the lowered barrier, PAT represents phonon assisted tunneling, and DT represents the direct tunneling into the conduction band (CB).....74

3.8. Schematic of the basic geometry of the 4H-SiC PCSS as reported in Mauch et al.....75

4.1. Comparison between the simulation J-F results and the experimental data for semi-insulating 4H-SiC for sample without irradiation.....82

4.2. Schematic diagram of the traps in the SiC material.....83

4.3. Calculated internal electric field profiles for the SiC2 sample at two steady-state current densities of -4.54×10-3 A/m^2 and -7.29×10-2 A/m^2 85

4.4. Calculated Electron density variation for the SiC2 sample at two steady-state current densities of -4.54×10-3 A/m^2 and -7.29×10-2 A/m^2 86

4.5. Calculated internal electric field profiles for the SiC2 sample at different current densities.....87

4.6. Comparison between the simulation J-*F* results and experimental data for semi-insulating 4H-SiC SiC1 sample subjected to the 1MeV irradiation. Simulation results were obtained for different cases as discussed in the text 89

4.7. Electric field magnitude versus anode-cathode distance for different situations in the absence of any photoexcitation. A cathode-anode bias of 10 kV was applied. (a) The basic device structure, (b) mesa structure with metal extensions of L= 0.5 mm at both the anode and cathode ends on a 4 μm SiC layer, and (c) mesa structure having a 0.5 mm metal extension above a sandwiched HfO_2 layer.....97

4.8. Results for the peak electric field magnitude as a function of the metal extension length L. The two plots shown correspond to the metal overhang above either SiC or HfO2 as shown in Figure 1.2 (b) and 4.8 (c). A thickness of t=4 μm below the metal overhang was chosen for both the SiC and HfO_2 calculations 99

4.9. Peak electric field magnitudes as a function of the oxide thickness t. The two curves represent structures with the HfO2 layer covering the entire region between the electrodes, and a partial mesa coverage. A contact metal extension of L = 0.5 mm on each of the anode and cathode sides was used for both structures 100

4.10. Calculated results of the peak temperature versus time in the PCSS at a 20 kV bias with L = 0.5 mm and a uniform 0.5 μm HfO_2 layer spanning between the electrodes 103

CHAPTER 1

INTRODUCTION

1.1 Motivation

Both Silicon and semi-insulating GaAs photoconductive switches (PCSSs) have been used in many high power applications. However, the physical properties of silicon carbide (SiC), such as a large bandgap (3.1-3.35 eV), high avalanche breakdown field (~3 MV/cm), and large thermal conductivity (4-5 W/cm-K) with superior radiation hardness and resistance to chemical attack, make SiC an attractive candidate for high voltage, high temperature, and high power device applications [1-4]. An important advantage of SiC is the ability to grow a stable thermal oxide, enabling fabrication of MOS-based device structures. Silicon carbide has a number of different polytypes, and 4H-SiC, which is a wurtzite material with a hexagonal Brillouin Zone (BZ), is favored (for example, over 6H-SiC) because of the higher and more isotropic bulk mobility. The latter translates to lower on-resistance in power devices and higher current density (*J*) capability.

GaAs has been employed as a linear photoswitch material due to its high electron mobility and large dark resistivity. The large mobility reduces the optical energy requirements necessary to produce a given conduction resistance. SiC, on the other hand, has comparatively much lower electron mobility, yet it can be designed for linear mode operations without an increase in optical closure energy. This is possible because of the material characteristics itself. A very low mobility in SiC is more than compensated by the very high breakdown strength ($3x10^6$ V/cm) [5]. If the band gap or sub-band-gap radiation is used to illuminate the respective materials, only 34% of the optical energy is necessary to produce the same conduction resistance

in a SiC switch as compared to a GaAs switch. Thus, the linear SiC switch can be used at much lower optical power, making it a remarkable improvement in the specification of linear PCSS. The main disadvantage with SiC as a photoswitch material is the high trigger energies required for linear-mode operation. SiC switches require a much higher optical energy to reach low ON-state resistance compared with high-gain GaAs photoswitches [5,6].

Since the early studies by Auston [7], photoconductive semiconductor switches (PCSSs) have been investigated intensively for many applications owing to their unique advantages over conventional gas and mechanical switches. These advantages include high speeds, fast rise times, optical isolation, compact geometry, and negligible jitter. Another important advantage is the ability to operate at high repetition rates with long device lifetimes (i.e., good reliability without degradation). In particular, photoconductive semiconductor switches (PCSSs) are low-jitter compact alternatives to traditional gas switches in pulsed power systems [5]. The advantages of PCSSs make them a perfect choice for many important applications where switching accuracy and high electric field (*E*) capability are required, such as in microwave and millimeter wave generation, impulse ultrawideband radar, and pulsed power systems, particle accelerators, direct energy systems, high-voltage pulse generation, and electron-beam pumped lasers [6,8-11]**.** Although most PCSSs have been fabricated using Si or GaAs, these materials have critical intrinsic limitations for operation at high fields, high temperatures, and high radiation levels [12,13].

Hence, there has been a great deal of interest in the development of SiC power switches, owing to the excellent properties of SiC [14,15]. For example, SiC is resistant to chemical attack and radiation and is stable at high temperatures [4]. Besides, SiC is the only technology currently available that can achieve MegaWatt output power and MegaHertz repetition rates,

which are of practical interest [11,16]. For the same breakdown voltage, the on-state resistance of a SiC device is expected to be lower by two orders of magnitude than that for Si because smaller layer thicknesses and/or higher doping levels can be used [17].

A small on-state resistance, which is a critical parameter for reduced power dissipation, not only depends on the semiconductor material used, but also on the contact properties. The contact problems are exacerbated by the need for the high-temperature high power operation expected of SiC devices. However, the use of n^+-GaN subcontact current spreading layers for 4H–SiC PCSS devices have been shown [18] to alleviate this potential problem.

This contribution focuses on an analysis of the steady-state and time dependent current-voltage response of semi-insulating 4H–SiC to probe the internal mechanisms and transport processes. There appears to be a relative dearth of reports in the literature pertaining to high field electronic behavior in semi-insulating SiC devices, barring a few studies [19], as compared to the well-studied GaAs material system. Furthermore, a good physical understanding of the inherent physics is essential if one hopes to predict and tailor the electrical response of SiC photoconductive switches at high fields. Internal traps and defects in the SiC devices are known to play an important role in shaping the observed *J-E* response [20]. For instance, experimental steady-state curves, obtained by a group at Texas Tech University and shown in Figure 1.1, are for a set of 4H-SiC samples with Ohmic contacts deposited by sputtering 50 nm Nickel-Chrome on 10 nm Titanium. The area of the SiC samples was roughly 6.35 mm × 6.35 mm, of which the contact areal dimensions were 4.826 mm × 4.826 mm. The distance between the top and bottom electrodes was 0.454 mm, and included many of the other device details as discussed elsewhere [21]. Some of the SiC samples (e.g., SiC1 as shown in Figure 1.1) were irradiated with a high-energy electron beam (1 MeV) for 3.5 hours with a total fluence of 2×10^{18} electrons/cm^2 to add

additional deep trap states that allowed the device to be operated at high electric fields with low leakage currents [22,23].

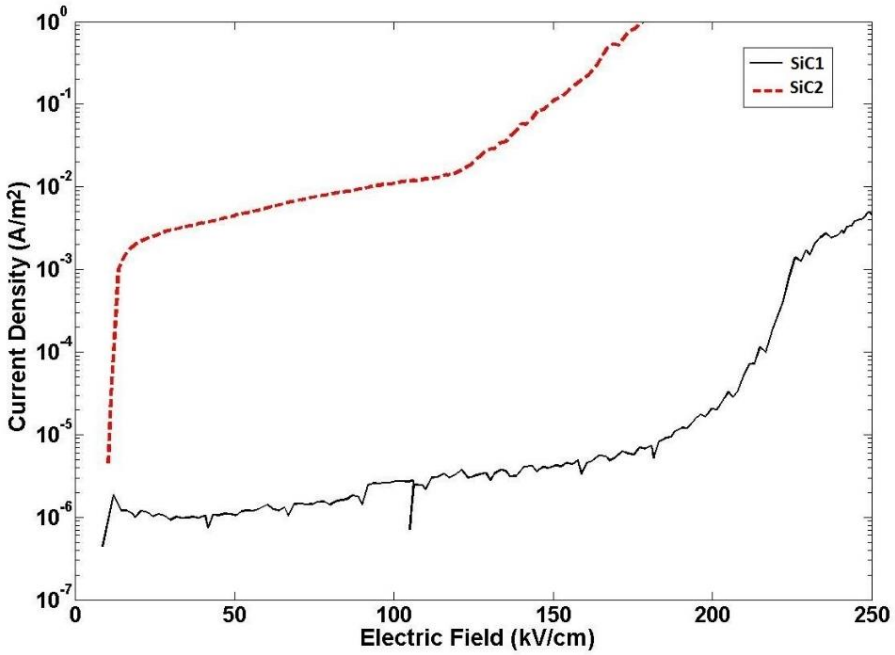

Figure 1.1. The experimental *J-F* characteristics obtained for semi-insulating 4H-SiC photoconductive devices. Solid line is for sample SiC1, taken from a set of samples that were electron-beam irradiated, while dashed line is for sample SiC2 that was not irradiated.

The experimental *J–E* curves indicate a nonlinear response, with space charge limited currents [24-26] expected to play an important part in molding the device characteristics. A cursory examination of the results of Figure 1.1 reveal the following features: (a) With negligible irradiation (sample SiC2), i.e., low levels of externally created traps, the current is seen to rise quite sharply by about three orders of magnitude at relatively low electric fields around 18 kV/cm. This trend is suggestive of a Mott-Gurney-like behavior [27], which is generally characteristic of space-charge transport in the absence of traps. However, at moderately higher electric fields (above ~22 kV/cm), the *J–E* curve of figure 1.1 is seen to exhibit a small, yet

nearly constant, slope. Due to the semi-logarithmic plot, this translates into a near exponential growth in current up to a field of about 130 kV/cm. At higher fields, a change in the slope is visible, and suggests the onset of another contributory process. (b) The samples in Figure 1.1 subjected to irradiation (denoted by SiC1), which can be assumed to have a much higher density of internal traps, exhibit much lower currents by comparison. This is expected, based on the theory of space-charge currents with electron trapping [24-26]. However, at fields just beyond 180 kV/cm, the measured currents rise sharply, a feature that is a likely signature of trap-filled conduction. More interestingly, though, current densities at much higher electric fields (i.e., values in excess of 225 kV/cm) seem to exhibit a slower rise at a nearly constant slope. This suggests an exponential-type current increase and marks the transition to another conduction regime.

Here, steady-state current conduction in semi-insulating SiC samples meant for high power photoconductive switches was probed, based on a one-dimensional (1D) model. A number of relevant processes, such as multiple defects, repulsive potential barriers to electron trapping, band-to-trap impact ionization, and field-dependent detrapping, were evoked and are included in a comprehensive model analyses. The roles of the various mechanisms and their respective electric field ranges of applicability are simulated. Simulated numerical results agree with the data for both the irradiated and the non-radiated 4H-SiC samples.

Calculations of electric field distributions within a SiC base photoconductive switch were also carried out to probe the effectiveness of strategies for mitigating the peak values. An issue of increasing concern, as power levels scale up and requirements move to larger switching voltages, is device reliability. In particular, recent work by Mauch et al. has shown crack formation in the SiC at the SiC/metal interface [21] in a variety of different device configurations

and structures. It has been hypothesized that the underlying cause of the observed cracks was either 1) the result of large current densities at the SiC/metal interface during operation, which could then also led to localized hot spots, or 2) the effect of high electric fields at the contact-SiC interface. Regardless of the origin, experimental optical microscope images confirm that the cracks form primarily near the surface and at points of greatest field enhancement [21].

High electric fields-driven device failures are well known. Detrimental effects can arise from the production of hot electrons [28] having sufficient energy to generate an electron-hole avalanche by impact ionization. Channeling of energy by the hot electrons increases the local temperatures. Thermal expansion can then lead to high stress or even to cracking in the vicinity of the hot spots. For completeness, it may be mentioned that a second (though not so well recognized) mechanism under high field operation is associated with the inverse piezoelectric effect (IPE) [29,30]. The basic source is the piezoelectric nature of a material that leads to strain under externally applied electric fields. The internal strain can create defects, in turn causing eventual degradation, and can increase the device resistance, due to time-dependent trap generation. This aspect would certainly be detrimental to photoconductive operation since low ON-state resistance values are typically desired. However, to clarify, it may be mentioned that there are differences between the hot electron (HE) scenario and the IPE. For example, at higher temperatures, the electron mean free path (which is dictated by phonon scattering) typically becomes shorter. Hence, a higher electric field (i.e., higher device bias voltage) is then necessary, in order to drive hot electrons beyond the impact ionization threshold, thus weakening the role of hot electrons. However, in the case of the IPE, higher temperatures would make it easier to cause stress and crack formation, as these processes are governed by Arrhenius-type activation energy barriers. In the present context, though, the IPE is not expected to be very

significant, since the piezoelectric constants for SiC are not very large, unlike some other wide bandgap materials like GaN. However, there could be a role if localized temperatures are not contained.

In any event, regardless of the exact mechanism, it is clearly beneficial to be able to mitigate the peak electric fields, or at least to re-shape their distribution towards greater uniformity with suppression of spatially localized peaks. Only then could one achieve the full performance potential of SiC devices for high power applications. One specific aim in the context of the observed SiC failures would be to reduce the peak electric field values in the neighborhood of the metal-semiconductor interface. Proper design of the edge terminations is necessary to reduce the well-known field crowding at the edges. Towards this end, a combination of two strategies is proposed. The first makes use of an extension of the metal contact to shape the potential, an idea originally proposed in the context of silicon planar diodes [31]. The concept is similar to the field plates used to mitigate the IPE in GaN High Electron Mobility (HEMT) structures [32], and also implemented in a number of other instances for GaAs- and GaN-based devices [33-35]. The extension of metal contacts should reduce the maximum electric field by offering an extended surface for termination of the field lines, thus effectively spreading the electric field over a larger distance, instead of having a concentrated field flux at the end-tip of the metal contact. Effectively, this would then lower the field crowding at the metal contact edge and would modify the field distribution. It may be mentioned for completeness that the metal contact extensions would typically come at the cost of additional parasitic capacitance. Though this might be an issue for the frequency response of transistors or amplifiers, in the present context of a PCSS this is of no relevance.

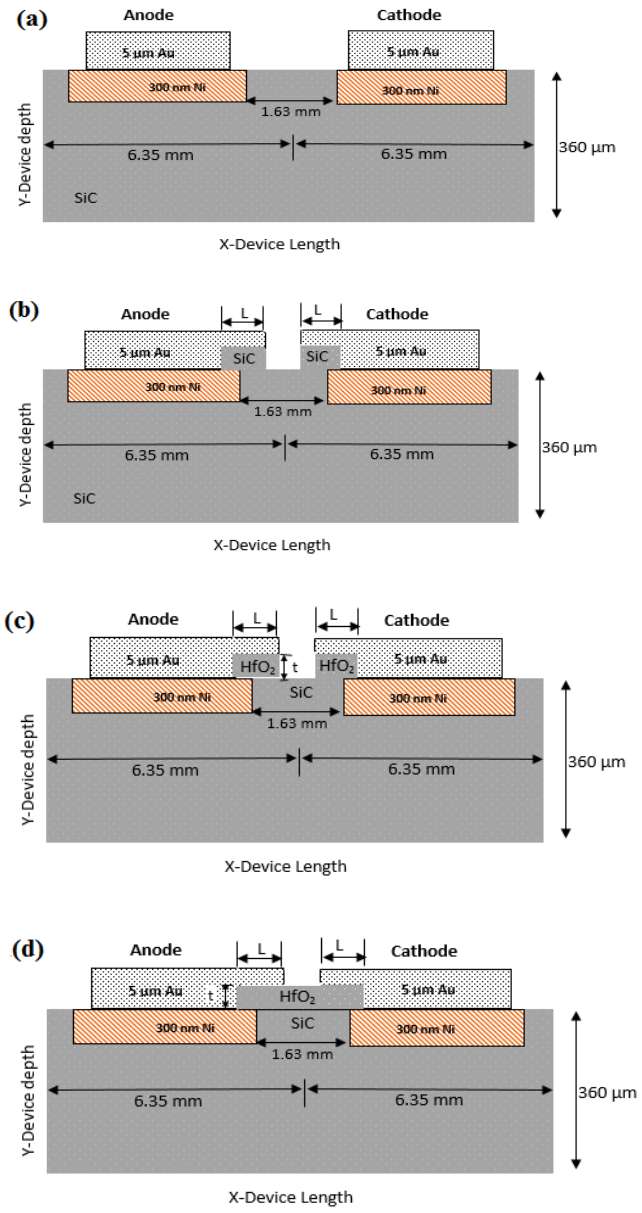

Figure 1.2. Schematic of the geometries of the 4H-SiC PCSS used in the simulations. (a) Basic geometry. (b) Mesa structure with metal extensions at both the anode and cathode ends, and (c) a similar PCSS mesa structure with metal overhang over HfO_2 material. (d) Metal extensions over a thin HfO_2 layer that spans the entire length between the two electrodes.

The second feature involves the use of high-*k* dielectric materials to cover the surface of the SiC PCSS in order to further mitigate the fields and thus also to reduce any potential for localized heating. A schematic (not to scale) of the proposed structure and simulated geometry is shown in Figure 1.1(c). It consists of a thin HfO_2 layer acting as a high-*k* dielectric, with the

metal in contact with the SiC and also present on the HfO_2 surface as an overhang. The basic PCSS dimensions and shape without any metal overhang or surface dielectric layer are shown in Figure 1.2(a). The sizes chosen in the figure correspond to the devices tested in a recent report by Mauch et al. [21]. The figure shows a 300 nm thick Ni-doped SiC layer just below the contacts. The doping was originally introduced in order to reduce the contact resistance of the PCSS. Figure 1.2(b) shows the use of a metal overhang on top of the SiC material, with the metal extension having a length *L* at each side.

Next, the use of a similar mesa-structure but with HfO_2 as a high-*k* dielectric sandwiched between the metallic contact extension and the SiC bulk is depicted in figure 1.2(c). An alternate structure employing HfO_2 is shown in figure 1.2(d). It is similar to that of figure 1.2(c), but in (d), the metal extensions lie over a thin HfO_2 layer that spans the entire length between the two electrodes.

The high-*k* dielectric can transmit or extract electric flux more efficiently. Hence, the peak fields (especially at the edges and sharp corners) can be expected to decrease due a combination of both the extended metal-plate overhang structure and the HfO_2 material. In addition, since HfO_2 is an insulator with a bandgap of about 5.5 eV, it presents a potential barrier to electronic transfer from SiC. Hence, carriers generated in SiC would be contained within that material, and possibilities of current flow and spillage into HfO_2 would be minimal. Furthermore, the higher bandgap of HfO_2, in comparison to SiC, would ensure that no photo-absorption would take place within the oxide dielectric layer. As regards high-*k* dielectrics, inorganic materials such as PZT [$Pb(Zr_{0.53}Ti_{0.47})O_3$] and Barium Strontium Titanate which might have been considered, but were not used here since they could present potential problems because of their hysteresis behavior. On the other hand, high-*k* materials such as HfO_2 or Ta_2O_5,

which are relatively hysteresis-free [36], would be ideal candidates for the present application. Hence, here HfO_2 was chosen as a candidate for numerical evaluations.

In this contribution, calculations of electric field distributions in a SiC PCSS structure with metal contacts employing contact extensions on a high-*k* HfO_2 dielectric have been carried out, with the goal of assessing reductions in the peak electric fields. For completeness, analysis of thermal heating in a lateral PCSS structure with such modified geometries after photoexcitation is also included.

1.2 The Scope and Organization of the Dissertation Research

This dissertation is organized as follows. Chapter 1 provides a brief introduction to the presented work, including the motivation for the project. Chapter 2 discusses theoretical principles of photoconductive switches, including characteristics of SiC material and classification of photoconductive switches. This chapter also describes the transport in semi-insulation materials. Lastly, Chapter 2 reviews other relevant issues for photoconductive switching, including single and double injection.

Chapter 3 focuses on the simulation methods for photoconductive switch analyses. This chapter includes details of the mathematical model used for the one-dimensional steady-state analysis. Numerical implementation for drift-diffusion analysis is also presented in this chapter. Further, a description of the Anode Hole model was mentioned. Also this provides a COMSOL computation for the inclusion of multi-dimensional and thermal analysis. This chapter also contains an introduction to and relevant discussion of the COMSOL Multi-physics software tool that was used for the two-dimensional electric field distributions and thermal analysis.

Chapter 4 presents the results from simulations using the models presented and discussed in Chapter 3. Values for the various parameters were calculated using the comparison of simulation results with the available experimental data. Reasons for the different behaviors of the curves are also discussed in this chapter. Finally, the results of the simulations with high-k dielectrics and metal overhang in SiC samples for reduced electric field profiles are deliberated.

Finally, Chapter 5 provides conclusions, as well as suggestions for future work that could be undertaken for further analyses and research evaluations.

CHAPTER 2

BACKGROUND AND LITERATURE REVIEW

2.1 Introduction

This chapter focuses on much of the background material on photoconductive switches. It begins with the simple concept of photoconductivity and the optical modulation of the conductivity of semiconductor materials. As already stated in Chapter 1, the primary goal of this dissertation research is to use SiC-based photoconductive semiconductor switches (PCSSs) for high power, high-voltage applications. The general utility and applications of photoconductive switches are briefly outlined in Section 2.2. The next section, 2.3, of the chapter focuses on some basic background on photoconductive switches. Section 2.4 outlines the different types of semiconductor switches, their modes of operation, geometries, and types of metal contacts. In section 2.5, details of the various semiconductor materials that could be used for such photoconductive applications are provided and discussed. Material requirements are discussed. The specific advantages of SiC material are outlined, and properties of SiC are reviewed in this section. Section 2.6 reviews the transport processes in PCSS devices with a focus on the role of contacts and related carrier injection, the influence of traps and their effects on carrier conduction, and the current-voltage response of the device. Other relevant issues such as generation-recombination processes are also discussed. Lastly, Section 2.6 touches upon the basic ideas of transport in semi-insulating materials. Finally, in Section 2.7, some of the issues relevant to high power applications based on SiC PCSS devices, including transit-time, recombination, conversion efficiencies, and resonant structures for optical absorption, are briefly discussed.

2.2 Photoconductivity and the Basic Concepts

Photoconductivity is the simple process of photon absorption by a semiconductor leading to the creation of mobile charge. In the presence of an externally applied voltage, the charge thus created by the photons can move, giving rise to conductivity. Thus, the optical source modulates the conductivity of the material. The process of optical absorption can involve two distinct routes: intrinsic absorption corresponding to the direct optical transition of electrons from the valence band to the conduction band, and extrinsic absorption involving transitions from either the conduction or valence bands to mid-gap defect levels. Since photons hardly have any momentum, the transitions are always direct. Hence, energies much higher than the bandgap are required for intrinsic absorption in indirect semiconductors such as Si, SiC etc. The optical absorption does not occur uniformly in a photoconductive material, but rather is dictated by the Beer-Lampert law [37], which predicts an exponential-type non-uniform behavior. Thus, the optical intensity $I(z)$ propagating into the material is given as: $I(z) = I(z=0) \exp(-\alpha z)$, where z is the normal distance from the incident surface into the absorbing material, and α is the wavelength-dependent absorption coefficient. The parameter α also depends on the material and generally increases with shorter wavelength associated with the larger density of states available for absorption at higher energies. In a relatively short device (with the switch thickness smaller than or equal to the absorption depth), or in situations relying on extrinsic absorption, this would ensure a fairly uniform carrier generation and conductivity modulation throughout the material.

The photoconductivity described above is used to drive photoconductive semiconductor switches (PCSSs), and an early review on this subject can be found in the book edited by C. H. Lee [38]. The device concept of a photoconductive switch is based on getting a semiconductor material to conduct electricity when it is turned on by light shining on the structure. Prior to the

optical turn-on, the device material does not conduct any electricity and has a very low value of "dark current." This low dark current signifies that the switch is in the OFF-state, but starts to conduct upon optical illumination. Usually in such PCSS devices, the electrical conduction ceases or rapidly decays once the light source is turned off. Under some situations, the electrical conduction can continue and can be long-lived; this is called a "latch-on" or "lock-on" effect [39]. The fundamental mechanism and inherent physical processes relevant to this effect are not completely understood to date.

The PCSS devices have primarily been used for two distinct types of applications: (a) in high power engineering and in pulsed-power systems, and (b) for ultrafast electronics and communications. The former class of applications requires the use of rugged devices that can withstand large (up to MV) voltages and can carry large currents (on the order of kA) in the ON state. In this arena, photoconductive switches offer an economic alternative to high voltage thermionic valves, triggered spark gaps, and thyristor stacks. The main advantages are that no losses are incurred by heaters, and that they offer a much longer working life and a photoconductive switch can readily be turned off. Other typical applications include uses for low-frequency high-voltage generators and impulse generators, and for power electronics where PCSS show significant advantages over thyristors and power Metal Oxide Semiconductor Field Effect Transistors (MOSFETS). Some other high power applications include microwave and millimeter wave generation, impulse and ultrawideband radar, pulsed power systems, particle accelerators, directed energy systems, and trigger generator systems [6,8-11]. The PCSS devices can be used in generating ultra-wideband signals where one is trying to produce only a few cycles per burst. Ultra-wideband is generally defined as a signal having a bandwidth that is >25% of the center frequency and whose power spectrum is continuous between the minimum

and maximum frequency. Generally a frequency of 1GHz or higher is needed, and switching speeds of tens to hundreds of picoseconds is required to precisely generate the signals. The PCSS devices are capable of such speeds and also of repetitive action.

The second class of applications are in the area of ultrafast but low-power electronics [40,41]. Such devices typically employ much smaller gaps between the two conducting electrodes to provide high speeds. The use of such ultrafast switching for electronic applications was made possible by the development of ultrashort pulse mode-locked laser systems. Such devices can be used for both the generation and detection of picosecond and subpicosecond electrical transients. In addition, differential photoconductive sampling techniques with a temporal resolution independent of the carrier lifetime have been demonstrated using such PCSS devices [42], and subpicosecond electrical pulses have been generated using asymmetric excitation of long-carrier-lifetime material [43]. It has also been shown that, based on the use of circuit ideas, one could implement pulse shaping to generate picosecond pulses [44].

2.2.1 Photoexcitation

Atoms and molecules have electrons bound in orbitals with specific energy levels. If a photon with energy hv is absorbed by an electron in an atom or a molecule, the electron may be excited to a higher energy level if the energy level difference between the initial and final states is equal to hv. This process is called photoexcitation and this is given in Figure 2.1. The vertical arrows show the transition. The solid circles and empty circles represent electrons and the vacancy left by the ionized or excited electron, respectively. The minimum energy needed to free an electron in an atom or a molecule is called the ionization energy of this electron. In the interaction of photons with atoms and molecules, electrons can be freed if the photon energy is

larger than the binding energy of these electrons, which is the process of direct photoionization [45]. These two are schematically explained in Figure 2.1.

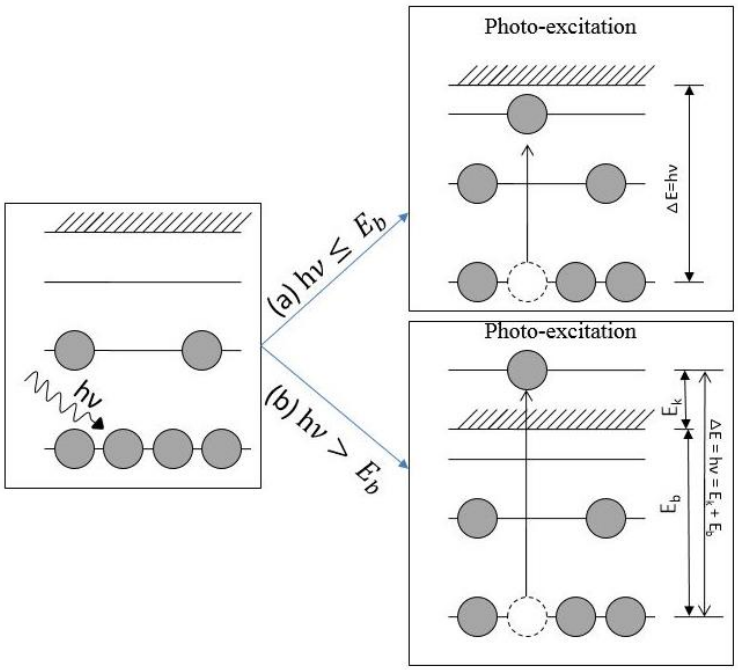

Figure 2.1. Schematic diagram of the photoexcitation and photoionization processes.

Photoexcitation can be mainly categorized into two sections: direct transition and indirect transition. In direct transition, phonons are not involved. The photon momentum is negligible compared with the electron momentum, so that when the photon is absorbed, it excites an electron from the valence band to the conduction band. The electron's *k*-vector does not change. A direct transition on *E*-*k* diagram is a vertical transition from an initial energy *E* and wavevector *k* in the VB to a final energy *E'* and wavevector *k'* in the conduction band where *k'*=*k* as illustrated in Figure 2.2.

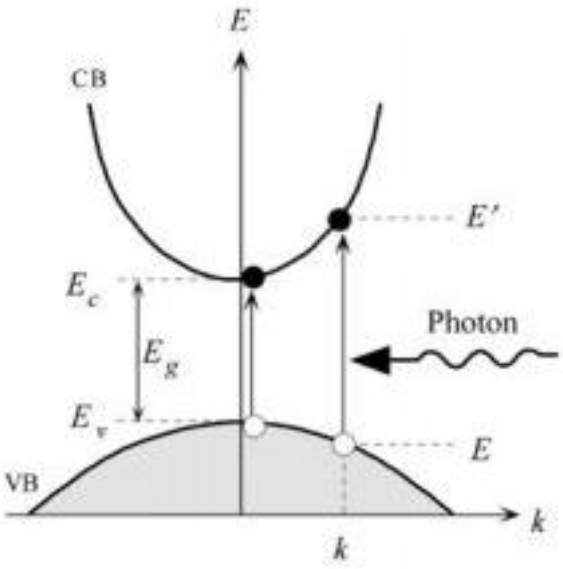

Figure 2.2. A direct transition from the valence band (VB) to the conduction band (CB) due to an absorption of a photon [46].

In indirect bandgap semiconductors such as Si and Ge, the photon absorption for photon energies near E_g requires the absorption and emission of phonons during the absorption process, as shown in Figure 2.3. The absorption onset corresponds to a photon energy of ($E_g - h\nu$), which represents the absorption of a phonon with energy $h\nu$.

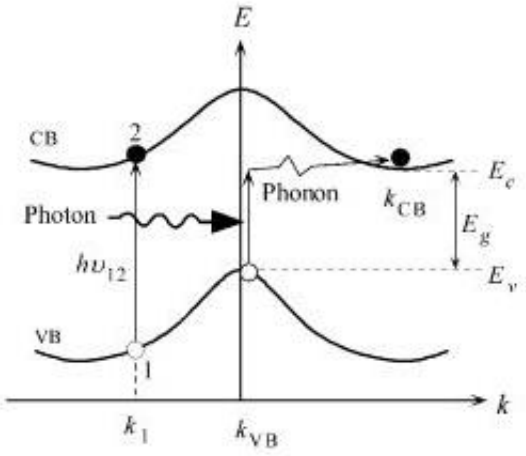

Figure 2.3. Schematic diagram of the indirect transition across the bandgap involving phonon [46].

The presence of localized electronic states in the band gap will increase the absorption of subband-gap photons. Therefore, absorption of subband-gap photons is very weak in single crystalline solids. Amorphous semiconductors have a considerable density of localized states, with energy in the gap giving rise to the absorption of subband-gap photons. Single subband-gap optical transitions in a semiconductor or insulator will generate an electron-hole pair.

The mechanisms of electron-hole pair generation induced by absorption of a subband-gap photon in an n-type semiconductor are illustrated in Figure 2.4. Mainly, there are three different mechanisms: (a), (b), and (c). In mechanism (a), a valence band electron absorbs a photon of energy hv and is promoted to an empty localized state at energy *E* in the band gap. The rate of this process per band-gap state at *E* can be denoted as $k(E - hv, E)\Phi$, where Φ being the light intensity. There will be two processes in this mechanism. The hole generated at $E - hv$ relaxes very quickly to the top of the valence band. The electron in the band-gap state at E can be thermally excited into a delocalized state at the bottom of the conduction band with a rate $\varepsilon(E, E_C)$. This rate is equal to $\beta_n N_C \exp[(E - E_C)/k_B T]$, where β_n is the rate constant for the capture of a conduction band electron in a band-gap state and N_C is the effective density of states at the bottom of the conduction band [47].

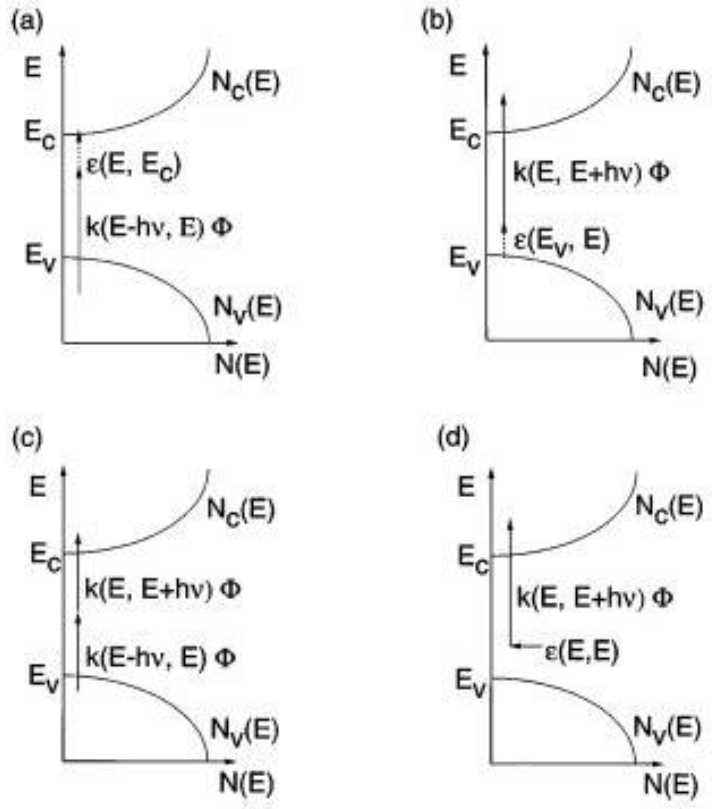

Figure 2.4 Mechanisms of electron-hole pair generation induced by absorption of a subband-gap photon, mediated by localized band-gap states [47].

As a result of this mechanism, an electron at the bottom of the conduction band and a hole at the top of the valence band are generated. Mechanism (b) explains the way that an electron from a localized state in the band gap at energy E optically excites into a conduction band state at $E + hv$. The rate per band-gap state is denoted as $k(E, E + hv)\Phi$. Thermally excited electrons from the top of the valence band will fill the empty states in the band-gap with the rate of $\varepsilon(E_V, E)$ [48]. In mechanism (c), an electron-hole pair is generated by the consecutive absorption of two subband-gap photons. In mechanism (d), an electron in an interfacial band-gap state will absorb a photon and this will result in an electron and an empty interfacial state.

2.3 Photoconductive Semiconductor Switches

2.3.1 Basic Background

Though the basic concept behind photoconductivity has been discussed above, it is perhaps germane to briefly review photoconductive switching devices, the different switch geometries, various modes of operation, and the type of contacts typically used. Since the early studies by Auston [7], photoconductive semiconductor switches (PCSSs) have been investigated intensively for many applications owing to their unique advantages over conventional gas and mechanical switches. An Auston switch [7] consists of a transmission line antenna with a gap that is bridged by a semiconductor and could be used for terahertz radiation. For such terahertz generation, a DC bias voltage is applied across the antenna [7]. When light from a pulsed laser with femtosecond pulses is focused on the gap, it excites charge carriers into the semiconductor's conduction band, which are subsequently accelerated by the bias voltage. The induced acceleration from the photocurrent causes the charge carriers to radiate in terahertz frequencies, generating a pulse lasting several picoseconds [49,50]. For use as a terahertz detector, the switch consists of the same geometry but without the applied bias voltage. Instead, the incident terahertz pulse itself provides the bias field for the charge carriers during the interval when the switch is activated by the (much shorter) laser pulse. The induced photocurrent can then be amplified and measured. To map the entire span of the terahertz pulse, the time delay between the femtosecond pulses at generation and detection can be varied. In particular, photoconductive semiconductor switches (PCSSs) are low-jitter compact alternatives to the traditional gas switches used in pulsed power systems [5]. The advantages of PCSSs make them a perfect choice for many important applications where switching accuracy and high electric field (E) capability are

required, such as in microwave and millimeter wave generation, impulse radar, pulsed power systems, high-voltage pulse generation, and electron-beam pumped lasers [6].

The speed of the switch mainly depends on the bulk properties of the semiconductor material. The primary advantage of photoconductive switches is that they can be scaled to large voltages and currents in a single device without sacrificing speed. Photoconductive switches are limited as power switches by the energy available from the exciting light source (or external electron beam). At least a micro-Joule of excitation energy is required per MegaWatt of switched power. The near-term applications of high power photoconductive switches require short electrical pulse lengths (~10ns), with fast rise times (~1ns), at low pulse repetition rates (~100Hz or lower). More specifically, some of the applications include electrical-discharge lasers, electron-beam pumped lasers, and electron-beam or light-ion-beam accelerator power supplies for inertial confinement. These applications require switching voltages ranging from tens of kilo-Volts to mega-Volts, at peak currents of from tens of kilo-Amperes to mega-Amperes. The jitter of the switch has to be less than 1ns. The scalability and the simplicity of photoconductors allow a single device to handle the voltages and current requirement.

Optical controllability of the photoconductive switch is advantageous, since the controlling (optical) system is isolated from the electrical power system. The optical excitation turns the switch on uniformly and simultaneously over the entire device. This is faster than any other switching mechanism, and therefore results in very low turn-on losses, which improves the switch efficiency. Further, optical switch control during conduction is possible because carrier losses due to recombination and sweep-out can be balanced and replenished by optical generation.

Furthermore, device scalability in terms of voltage, current, heat removal, and inductance is advantageous in pulsed-power applications. For a given optical energy deposited on the switch surface, the resistance is proportional to the square of the device length and is independent of width. The desired operating voltage will determine the switch length, while the switch width is determined by the desired current. Therefore, widening the photoconductor switch for a specific length results in several major advantages. Increasing width does not change the ″ON″ resistance of the device. The Joule heating per unit width, the current per unit width, the optical energy density on the material, and the total device inductance are all decreased, while the surface available for heat removal is increased. Hence, the average power and the peak power of the switch scale with the switch width. Figure 2.5 shows the schematic diagram of a photoconductive switch. Here, *l*, *w* and d_e represent the length, width, and thickness of the material, respectively.

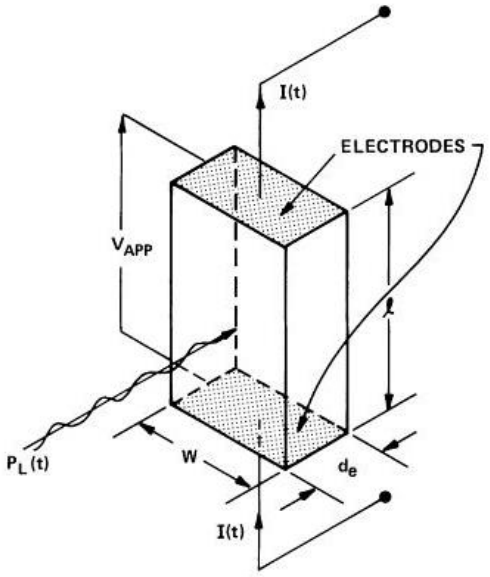

Figure 2.5. PCSS schematic showing the current, *I(t)*, applied voltage $V_{APP,}$ and device dimensions. [38].

2.3.2 Desired Switch Characteristics

In general, the following lists some of the desired characteristics of an efficient photoconductive switch:

- High hold-off voltage. This is useful for extending the limits of high-power applications.
- On-resistance much lower than load resistance. This simply translates into low losses during the conductive phase and the switching of maximum voltage to the load. This would also lower internal heating and thus circumvent device cracking or thermal runaway.
- Fast opening, which promotes quick response and high-frequency operation with rapid switching. The turn-off time is determined by the bulk recombination of the excited carriers or by carrier sweep-out.
- Fast closing, compared to conduction time for high speed operation. If we ignore limits that are due to circuit inductance and capacitance, the turn-on time of the switch is determined primarily by the excitation pulse length.
- Off-resistance much higher than load resistance, so that the switch can virtually isolate the input from the load side of the switched system. The off-state resistance of the switch is determined primarily by the dark resistivity of the photoconductive material and device dimensions. A higher bandgap promotes low carrier concentrations and hence, higher off-resistances.
- Constant on-resistance to avoid any current or voltage fluctuations or variations.
- Fast recovery for high repetition rates and quick subsequent switching.
- Switch should be jitter-free, to minimize deviation from the true periodicity of a presumed periodic signal in electronics and telecommunications.

- Good thermal conductivity to transport heat away from the device and to assist in thermal management, while reducing possibilities of second breakdown.
- The absence of internal inhomogeneities, such as traps and defects. Their presence tends to result in a variety of deleterious phenomena, such as persistent photoconductivity (PPC), low conversion efficiency, internal heating, increased noise through trapping-detrapping, and the development of spatially inhomogeneous electric fields with current filamentation.
- Simple structure and ease of fabrication for cost minimization.

2.4 Classification of Photoconductive Semiconductor Switches

2.4.1 Classification According to the Mode of Operation

2.4.1.1 Linear photoconductive semiconductor switch

In the linear mode, one absorbed photon will create one electron-hole pair. Hence, the electrical conductivity of the material will be linearly proportional to the total photon flux illuminating the semiconductor material. Also, the switch conductivity will approximately follow the shape of the optical drive pulse. As a result, linear switches allow precise control of high power impulses, with the closure time being limited only by the intensity of the light source. Such a switch will fully close at sufficient optical intensity and this will remain closed while illuminated. And the switch will open with a characteristic time constant, which is related to the carrier lifetimes after the optical pulse is removed. Theoretically, such switches can also open either by recombination of the charge carriers or by sweeping of the carriers out of the high field region [51]. Optical activation yields a very precise timing of closure, so that multiple switches

can be synchronized to almost arbitrary precision. The linear mode switching is essential in applications requiring fast turn-on and fast turn-off switches. Neutron irradiated or heavily chrome doped GaAs are often used in switches which will turn on and turn off in less than 200ps. The neutron irradiation results in limited damage within the detector and mainly creates defects and trap levels within the semiconductor bandgap. These traps facilitate indirect recombination of electron-hole pairs, thus providing for a rapid turn-off upon cessation of the external illumination. Thus, neutron irradiated GaAs devices are used to produce very fast radiation detectors. Recombination times of less than 100 ps have been observed in neutron irradiated GaAs. In a similar vein, chrome doped GaAs can be used to introduce midgap traps that enhance recombination and reduce the turn-off time [51].

2.4.1.2 Non-linear photoconductive semiconductor switch

As discussed above, a linear PCSS device is gated 'ON' by generating carriers in the bulk semiconductor material by applying photons of the proper wavelength. An electron-hole pair is generated for each absorbed photon, in the ideal case. On the other hand, a nonlinear PCSS device is gated 'ON' by optically generating a small number of carriers in the semiconductor bulk that are multiplied by an electric field avalanche mechanism. However, when the bias electric field across a GaAs switch exceeds around 4-8 kV/cm, a transition occurs to a nonlinear mode that exhibits high gain and extended conduction. This has been referred to as "lock-on" [51]. In lock-on, the field across the switch drops to 3-5KV/cm, but the current does not decrease and it continues to flow, as if the switch has locked on to some value of persistent current. In this mode of operation, if the laser pulse is strong enough, it can also determine the closing time of the switch, similar to the situation for the linear mode [51]. But the difference is

that, in this case, the switch will remain closed or 'locked-on' until the current is interrupted or disrupted by the circuit. In this lock-on situation, if the bias electric field is increased further, the optical pulse amplitude required for conduction can be decreased. It is assumed that the increased electrical energy made available to the mobile charge carriers upon an increase in the bias allows for a reduction in the optical trigger energy. However, it may be noted that the increase in the electric field does not increase switch trigger sensitivity.

In summary, when the nonlinear electric field threshold for switch material is reached, the turn-on speed of the switch is determined by the avalanche process, independent of the laser rise time. The pulse amplitude locks on to a characteristic electric field until the current through the switch is turned off. If the laser rise time is faster than the avalanche rise time and the laser amplitude is high enough, the optically generated carriers can dominate. Hence, the switch turn-on is faster than its characteristic avalanche time. But the switch will still lock on, even though the optical pulse from the laser may have ended. Reasons for the lock-on are not fully understood although a number of plausible theoretical explanations and hypothesis have been put forward to explain this non-linear switching behavior. Trap filling and impact ionization of traps are among some of the possible explanations [52,53].

2.4.2 Classification According to the Operating Geometry

2.4.2.1 Lateral geometry

Two simple pictures of the lateral geometry for a PCSS are shown in Figure 2.6, below. The incident photon source illuminates the device from the top, and the entire surface is thus exposed to the laser triggering. It is thus convenient to shine the light from one side, with

beam coverage over the entire front face, giving rise to large area illumination and efficient power conversion into a higher density of electron-hole pairs.

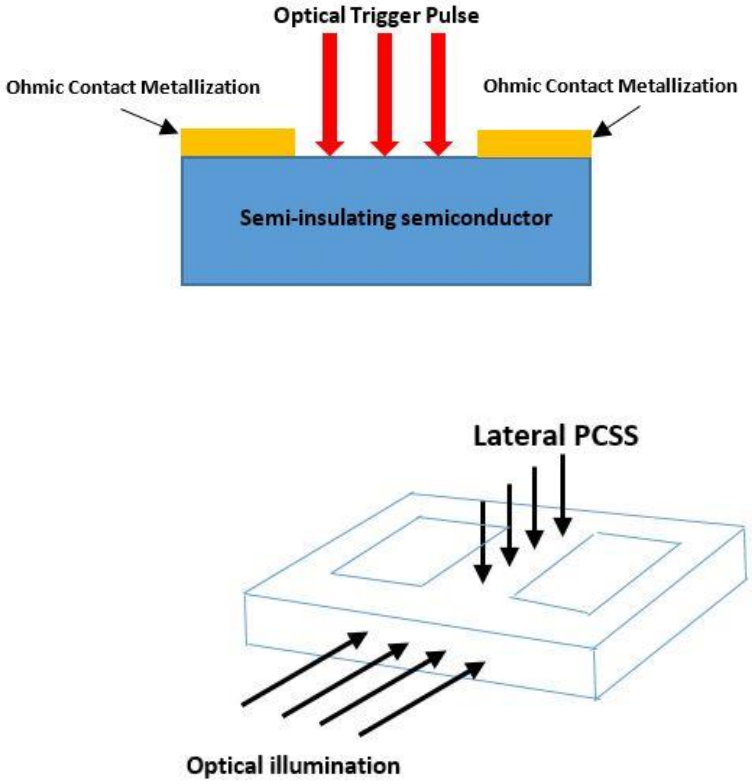

Figure 2.6: Lateral geometry PCSSs.

In this geometry, the optical radiation intensity will typically fall off exponentially with depth, in keeping with the Beer-Lambert law dependence. Hence, the highest density of photo-carrier will be generated close to the surface. Since the electrodes sit on the surface, the electric fields will naturally be the highest near the top surface region. Hence, the efficiency of collection of the electron-hole pairs by the anode and cathode, respectively, would be good.

2.4.2.2 Vertical geometry

An alternative for operating the PCSS could be the vertical geometry as shown in the diagrams of Figure 2.7. In this case, the laser illuminates the PCSS device from the sides.

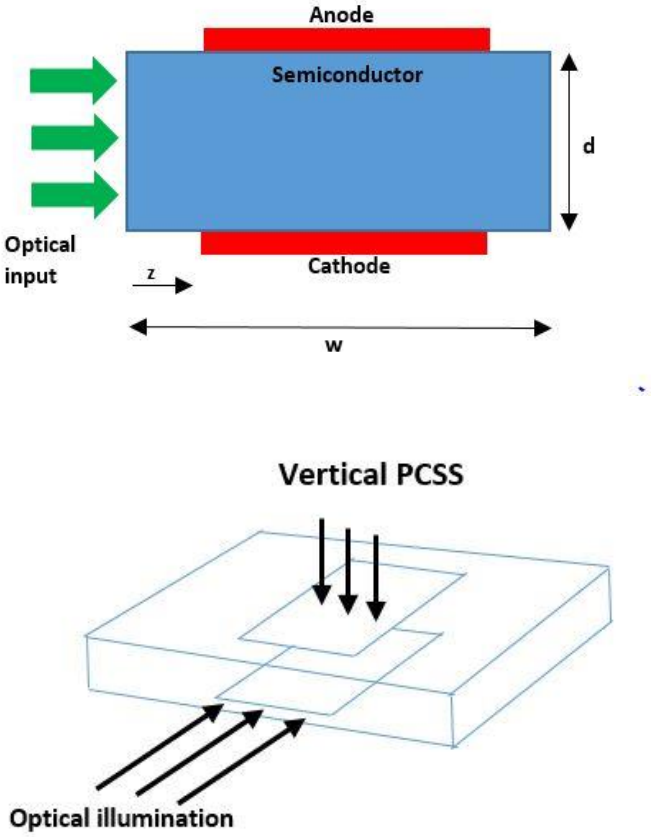

Figure 2.7. Vertical geometry PCSSs.

If the width *W* of the device is large, then quite conceivably, the absorption of light and generation of electron-hole pairs would not be very strong at the center where the electric field is expected to be the highest. Hence, the collection efficiency may not be very good, and the transit time may be slow. The latter would adversely affect the turn-on speed of the PCSS device. However, a potential advantage of this geometry is the relatively large distance around the

device that separates the anode metal from the cathode contact. As a result, surface flashover and breakdown through the surrounding air is likely to be small and well under control.

2.4.3 Classification According to the Device Contact

The behavior and electrical response of PCS are strongly affected by the type of contacts made to the semiconductor. Therefore PCS can be categorized according to the type of contact.

2.4.3.1. Devices with dual Ohmic contacts

The Ohmic contacts allow for symmetric conduction of current in either direction, and also provide for low contact resistance. The latter is very useful for photoconductive devices, since the goal is for the switch to act as an ideal short-circuit during the "closure" phase. Fabrication of Ohmic contacts is facilitated by the use of selected metals, depending on the semiconductor material. For example, Ni/AuGe for n-type GaAs, or Au-based Ohmic contacts to p-GaAs, etc. However, the problem of an Ohmic contact can be that it allows for both electron and hole injection. In terms of basic physics, this occurs because the potential barriers for both electrons and holes are moderate. As a result, the double injection phenomena can occur and can lead to the flooding of both electrons and holes within the device. Such a presence of both carrier types leads to strong increases in currents while reducing the voltage drop across the device. An S-shaped internal instability can then, potentially, be created that can lead to filamentary current formation and possible device failure.

2.4.3.2. Devices with one Ohmic (injecting) and one Schottky (blocking) contact

The scheme can be employed if the goals are to suppress double-injection and to gain stability. In these situations, the photocurrents would tend to be lower than in the case of dual Ohmic contacts, but at the benefit of better device stability.

2.4.3.3. Devices with both Schottky contacts

This type of contacts lead to a response where the injection from the contacts is very weak. Physically, this occurs because the potential barriers for injection into the semiconductor for both electrons and holes are fairly large. Practically, this is attained by selecting the proper metallization. For example, use of Ti/Pt/Au on GaAs leads to Schottky contacts. As a result, the current through the device is almost solely controlled by the external laser excitation.

2.5 Photoconductive Materials

The material necessary to fabricate the PCSS should be a high-resistance or semi-insulating semiconductor that provides a large or insulator-like ‘off' resistance when not illuminated. In the ideal case, the voltage applied to a semiconductor switch should be distributed uniformly between the electrodes across the switch medium. When a laser pulse illuminates the semiconductor between electrodes, the optical energy should change the conductivity of the inter-electrode switch medium very quickly, either linearly or nonlinearly. In the optically controlled linear photoconductive mode, one electron-hole pair is created for each input photon, whereas in the nonlinear or optically initiated conducting mode, nonlinear processes (such as impact ionization) within the switch can create multiple electron-hole pairs that would subsequently generate a large number of electron-hole pairs [51].

Historically, both Silicon and semi-insulating GaAs photoconductive semiconductor switches [5, 39, 54-59] have been used in many high power applications. Other than these materials, InP, ZnSe, [60-64] and also Diamond [65] have also been used in photoconductive switches.

GaAs has been employed as a linear photo-switch material due to its direct bandgap, high electron mobility, and large dark resistivity. The large mobility reduces the optical energy requirements necessary to produce a given conduction resistance. Its direct bandgap, as compared to Si or SiC, implies that a higher optical conversion efficiency is made possible. SiC, on the other hand, has comparatively much lower electron mobility but has a high drift velocity at high electric fields and can be designed for linear mode operations without an increase in optical closure energy. Besides, SiC has a very high breakdown strength ($3x10^6$ V/cm) [14], which would allow operation at much higher voltages for high power applications. If the band gap or sub-band-gap radiation is used to illuminate the respective materials, only 34% of the optical energy is necessary to produce the same conduction resistance in a SiC, as compared to a GaAs, switch. Thus, the linear SiC switch can be used at much lower optical power; this is a remarkable improvement in the specification of linear PCSS. The main disadvantages with SiC as a photoswitch material are the high trigger energies required for linear-mode operation. SiC switches require a much higher optical energy to reach low ON-state resistance, compared with high-gain GaAs photo-switches [14,16]. Though most PCSS have been fabricated using Si or GaAs, these materials have critical intrinsic limitations for operation at high fields, high temperatures, and high radiation levels [12,13].

Hence, there has been a great deal of interest in the development of SiC power switches [2, 14]. Besides, SiC is the only technology currently available that can achieve Mega-Watt

output power and Mega-Hertz repetition rates, which are of practical interest [16]. For the same breakdown voltage, the on-state resistance of a SiC device is expected to be lower by two orders of magnitude than that for Si, because smaller layer thicknesses and/or higher doping levels can be used. A small on-state resistance, which is a critical parameter for reduced power dissipation, not only depends on the semiconductor material used, but also on the contact properties. The contact problems are exacerbated by the need for the high-temperature high power operation expected of SiC devices. However, the use of n^+-GaN subcontact current, spreading layers for 4H–SiC PCSS devices, has been shown [18] to alleviate this potential problem.

The semiconductors are intentionally undoped to achieve low leakage currents and large conductivity modulation capabilities. One scheme employed in the past has relied on using semi-insulating (SI)-GaAs, marginally doped with Si and compensated with deep-level Cu or Fe acceptors [66]. The Bistable Optically Controlled Semiconductor Switch (BOSS) [67-70] is a good example of such an intentionally doped switch. The BOSS device utilizes the excitation of electrons from deep centers, such as those provided by copper in copper-compensated silicon-doped semi-insulating GaAs (Cu:Si:GaAs), to induce photoconductivity. The small cross section for electron trapping into a Cu center allows for long conduction times without continuous laser radiation. Also, the BOSS device can be interrupted on command by the application of a second laser pulse of longer wavelength. This laser pulse floods the valence band with free holes, thus inducing a rapid quenching of the photoconductivity over a time scale given by the electron-hole pair lifetime of the material, which can be as short as the subnanosecond range.

However, semi-insulating SiC is an upcoming material and is becoming a viable candidate because of its stable characteristics at high temperature, its high band gap, and its large electron saturation velocity [52,71]. Large bandgap (3.1-3.35 eV), high avalanche breakdown

field (~3 MV/cm) and large thermal conductivity (4-5 W/cm-K) with superior radiation hardness and resistance to chemical attack are some of the physical properties of SiC [72]. Another important advantage of SiC is the ability to grow a stable thermal oxide, enabling fabrication of MOS-based device structures. SiC PCSSs also offer other advantages, both at low field and in high voltage pulse formation configuration. A number of recent studies have been devoted to the analysis of SiC PCSS [53,73]. Silicon carbide has a number of different polytypes, and 4H-SiC, which is a wurtzite material with a hexagonal Brillouin Zone (BZ), is favored (for example, over 6H-SiC) because of its higher and more isotropic bulk mobility. The latter translates to lower on-resistance in power devices and higher current density (*J*) capability. As regards parameters for the photoconductive switches, one typically needs to consider the aspects discussed below.

1. The material bandgap, E_g

This parameter controls the leakage current and the intrinsic carrier concentration. Low leakage currents maintain a high-impedance *OFF* state. Further, this places an upper limit on the operating temperature and controls the cutoff wavelength of the input optical excitation. Furthermore, direct bandgap materials enhance the conversion efficiency, since the entire optical energy goes into placing electrons in the lowest conduction band for subsequent current flow. In an indirect bandgap material, the optical excitation places electrons in a higher lying conduction band, from where they cascade down to the lowest valley for current conduction. This cascade down to the lowest valley effectively results in a loss or wastage of useful energy.

2. The breakdown field and dielectric strength

These parameters are useful for extending the limits for high-power, high-voltage applications. The material should be able to bear a high electric field and should have a large breakdown/blocking voltage capability. If the breakdown field strengths are not high, then the semiconductor would not be able to hold off a large voltage during its OFF-state.

3. Thermal conductivity

Material should have a good thermal conductivity in order to enhance the internal heat dissipation, thereby ensuring that the device temperatures do not become excessively high. An efficient dissipation would enhance the power handling capacity of the switch, and would also ensure that detrimental thermal effects, such as the generation of local stress or cracks or defects or thermal runaway and second breakdown [74,75], would not occur.

4. Saturated drift velocity

The saturated drift velocity v_{dsat} is the maximum speed with which electrons can travel. This parameter controls the speed of the device response, as well as the current density levels since the current density J is related to the drift velocity as: $J = q\, n\, v_{dsat}$, where n is the density of the mobile carriers.

5. Ionization breakdown threshold

The ionization breakdown threshold generally dictates the highest possible operating electric field. Since the voltage magnitude is simply the integral of the electric field over distance, this means that the maximum applied bias is directly dependent on the peak ionization

threshold. Any internal fields that exceed the ionization breakdown value would lead to impact ionization and potential avalanching that would flood the device with carriers and destroy the switch, due to excessive currents and heating.

In addition to band-to-band ionization, there can also be trap-to-band impact ionization in materials or devices that happen to have traps present. For example, an energetic electron could detrap an electron from a defect. While this would help enhance the photocurrent and would help keep the device operating in the non-linear mode with current gain, there is the danger that it could lead to potential instability or reduce the photoconductive decay. In addition, the impact ionization (both band-to-band and trap-to-band) could produce enhanced noise. However, as the switching signals have relatively large magnitudes, the noise would not likely be a significant issue in the present context.

6. Low system losses

The need to minimize optical losses, such as those encountered during optical fiber transmission, constitutes another important consideration in the efficient design of photoconductive switches. Since the lowest optical losses in communication systems and fiber optic cables occur at wavelengths of around 1.55 μm, semiconductors that have energy gaps in this range are often the materials of choice. Thus, for example, InP is one such material, and there are others (e.g., GaAs) that are also close enough to this value.

7. Other parameters of some interest or consequence

In addition to the above parameters, a number of other aspects also influence or affect the performance of the photoconductive switches. For example, a multitude of traps at different

energies within the conduction band would lead to recombination during the ON state, thereby reducing the current delivered to the external circuit. In addition, there would be a range of emission and trapping time constants associated with the various traps that would lead to a multi-exponential decay in time-dependent currents.

While the midgap states can lead to recombination, there can also be optical transitions from the filled midgap states to the conduction band, or between the valence band and the empty midgap states. Such transitions would help increase the material conductivity during the switch turn ON phase.

2.5.1 Silicon

Silicon has been one of the most widely used semiconductor materials. Silicon has a band gap of approximately 1.1eV, which can absorb Nd:YAG laser light at wavelength, λ = 1.06 μm. The absorption depth at this wavelength is 1mm. Silicon is an indirect bandgap material, and, as a result, has a long (microsecond to millisecond) carrier lifetime t_R. This long carrier lifetime is useful for producing wide electrical pulses using narrow nanosecond optical pulses. Having a high leakage current and bad thermal conductivity are the major drawbacks of Si [51]. Properties of Silicon at 300K are presented in Table 2.1, below.

Table 2.1: Properties of Si at 300 K [76]

Properties of Si	**Value**
Band Gap	1.12 eV
Critical breakdown field strength	$3x10^5$ V/cm

Properties of Si	Value
Electron mobility	1500 $cm^2/V/s$
Hole mobility	600 $cm^2/V/s$
Saturation velocity	$2x10^7$ cm/s
Thermal conductivity	1.45 watt/cm°C
Intrinsic carrier concentration	$1.6x10^{10}$ cm^{-3}
Work function	4.8 eV
Dielectric constant	11.8

2.5.2 GaAs

GaAs is a direct bandgap material with a bandgap of nearly 1.42eV. This bandgap corresponds to an optical absorption of approximately 890 nm [51]. GaAs material can be switched with a 1.06μm light source using extrinsic generation of carriers. It is suitable for high-voltage applications due to its high resistivity ($\rho>10^8$ ohm/cm). The material is also less susceptible to thermal runaway than Si. The larger bandgap of GaAs results in a lower leakage current and also a higher dark resistivity. Carrier lifetimes in GaAs can be on the order of pico- to a few nanoseconds, since this is a direct bandgap material, a property that is useful for fast turn-off to provide sharp and narrow electrical pulses. Therefore, GaAs switches can be used in applications where nanosecond closure times are required. The highest breakdown fields that have been reported for GaAs PCSS devices have been around 0kV/cm. Some useful properties of GaAs are listed for convenience in Table 2.2.

Table 2.2: Properties of GaAs at 300 K [76]

Properties of Si	**Value**
Band Gap	1.43 eV
Critical breakdown field strength	$4x10^5$ V/cm
Electron mobility	8500 $cm^2/V/s$
Hole mobility	400 $cm^2/V/s$
Saturation velocity	$1x10^7$ cm/s
Thermal conductivity	0.46 watt/cm°C
Intrinsic carrier concentration	$1.1x10^7$ cm^{-3}
Work function	4.7 eV
Dielectric constant	10.9

2.5.3 SiC

Silicon carbide is a wide bandgap single crystal semiconductor with an indirect band structure. This material is formed by stacking silicon and carbon atoms in combination, resulting is several different 'polytypes', based on the stacking sequence. Over 200 different polytypes of SiC have been identified [77,78]. The polytypes are named, based on their crystal structure, as either cubic (3C-SiC) or hexagonal (6H-SiC) or a hybrid (e.g, 4H-SiC).

Table 2.3: Comparison of the physical properties of Si, GaAs and SiC [79]

Relative properties	**Si**	**GaAs**	**3C-SiC**
Band gap at 300K (eV)	1.1	1.4	2.2
Dielectric strength (10^6 V cm^{-1})	0.3	0.4	4
Thermal conductivity W/(cm.K)	1.5	0.54	5
Saturated electron drift velocity ($1x10^7$ cm/s)	1	2	2.5
Melting temperature (^{0}C)	1420	1238	>1800
Physical stability	Good	Fair	Excellent

The two hexagonal polytypes (4H-SiC and 6H-SiC) and one cubic polytype (3C-SiC) are the most common polytypes. The 4H-SiC and 6H-SiC samples are commercially available in wafers up to 150 mm diameter. SiC has a higher breakdown field and that is ten times that of GaAs. Compared to Si and GaAs, SiC has a higher electron saturated drift velocity and higher thermal conductivity [76]. Table 2.3 gives a comparison of the relative properties of Si, GaAs and SiC. The basic parameters of the SiC polytypes 6H, 4H, and 3C are listed in Table 2.4.

Table 2.4: Some parameters of SiC polytypes [80]

Parameter	**4H-SiC**	**6H-SiC**	**3C-SiC**
Band gap	3.2	3.0	2.3
Lattice constant, A	a=3.09, c=10.48	a=3.09, c=15.12	4.34
Thermal conductivity W/cm deg	3-5	3-5	5
Critical breakdown field strength mV/cm	2-3	2-3	>1.5

Parameter	4H-SiC	6H-SiC	3C-SiC
Electron mobility$cm^2/(V.s)$ at 300K	800	200-300	1000
Saturation rate, $1x10^7$ cm/s	2	2	2.7
Hole mobility $cm^2/(V.s)$ at 300K	60	50	40

Figure 2.8 shows different polytypes' lattice arrangements. Depending on the polytype crystal structure, the band gap varies from 2.2 to 3.3 eV, while the breakdown electric field varies from 2.5 to 5 MV/cm. The drift velocity value is around $2x10^7$ cm/s, whereas the thermal conductivity is 4.9 W/cm°K [76].

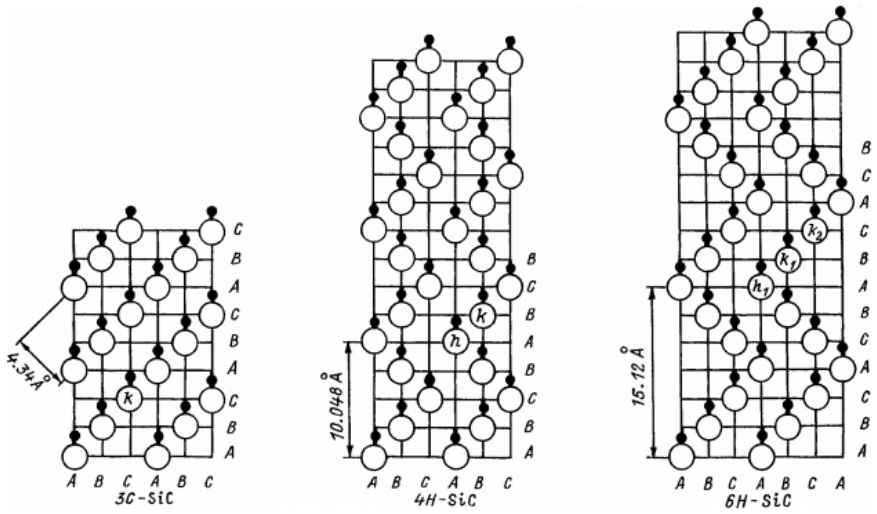

Figure 2.8. Lattice arrangement of different polytypes [81].

The 6H SiC polytype has a bandgap of approximately 3.02 eV. This corresponds to an optical absorption threshold of approximately 410 nm. There are large concentrations of deep levels within the bandgap (e.g., deep levels that are created through external electron or neutron irradiation). Therefore, 6H SiC can be switched with a 1.06 μm or a 532 nm light source, producing a route to extrinsic carrier generation from transitions between the deep levels and either the conduction or valence bands. 4H-SiC is typically grown via two primary methods: either by physical vapor transport (PVT) or by high temperature chemical vapor deposition (HTCVD) [82].

Silicon carbide, as an indirect bandgap semiconductor, offers some benefits when tuning the excitation wavelength. Absorption in silicon carbide does not exhibit a sharp transition at the band edge. Usually, it is expected that above bandgap light is absorbed mostly at the surface with little penetrating into the bulk material. For SiC, however, it has been shown [16] that above bandgap light can still penetrate hundreds of micrometers into the material. This makes it possible to tune a laser source to a specific application, maximizing absorption depth and carrier generation within an optically controlled device [72].

The physical vapor transport (PVT) growth technique usually yields n-type 4H and 6H-SiC crystals. This is a result of the presence of nitrogen as an unintentional n-type dopant in the PVT growth crucible. The nitrogen originates from the adsorption of air by graphite parts and the SiC powder source. Nitrogen (N) is a shallow donor that substitutes on the three (two) inequivalent Carbon sites in the 6H (4H)-SiC. The three nitrogen donor levels typically reside at 80 (h), 137 (k1) and 142 (k2) meV below the 6H-SiC conduction band [83]. Here, h and k correspond to the hexagonal and cubic inequivalent sites. In 4H-SiC, the nitrogen donor levels reside at 92 (k) and 52 meV below the conduction band [84]. The nitrogen impurity density

depletes exponentially during crystal growth. Boron is another impurity present in the growth chamber, due to graphite parts. Boron is a p-type dopant that substitutes primarily at silicon sites with energy levels of 300 – 330 meV and 650 meV above the valence band for the 6H and 4H-SiC polytypes, respectively.

2.5.4 GaN

Gallium Nitride is another attractive wide bandgap semiconductor material for the high power switching application. Gallium Nitride (GaN) is thermodynamically stable in both the wurtzite and zincblende crystalline structure. GaN is usually grown by epitaxy. The growth substrate material determines the crystalline structure of the GaN epitaxial layer. The GaN structure will be wurtzite if it is grown on silicon, silicon carbide, or sapphire substrates and zincblende if it is grown on GaAs substrates. The GaN wurtzite "a" and "c" lattice constants are 3.189 and 5.185 Angstroms, respectively. The GaN wurzite is composed of two interpenetrating hexagonal closed packed (hcp) sublattices. GaN offers higher breakdown field, saturated electron velocity, and electron mobility, compared to silicon carbide. In addition, GaN has a direct bandgap.

Table 2.5: Some parameters of GaN and SiC polytypes [2]

Properties	**6H-SiC**	**4H-SiC**	**2H-GaN**
Bandgap (eV)	3.0	3.2	3.4
Lattice Constant (A)	a=3.08	a=3.08	a=3.189
	c=15.12	c=10.08	c=5.185

Properties	6H-SiC	4H-SiC	2H-GaN
Breakdown Field (MV/m)	2.5	2.2	3.0
Saturation Electron velocity (10^7 cm/s)	2.0	2.0	2.5
Electron Mobility (cm^2/V-s)	415 perp. C 87 parall. C	947 perp. C 1141 parall. C	400
Hole Mobility (cm^2/V-s)	80	120	30
Dielectric Constant (ε_r)	10.0	10.0	9.5
Thermal Conductance (W/cmK)	3-5	4.8	1.3
Coefficient Thermal Expansion (10^{-6}/K)	4.5		5.6
Density (g/cm^3)	3.2	3.2	6.1
Melting Point (C)	2830	2830	2500
Direct / Indirect Bandgap	I	I	D

GaN melts at a high temperature (2500 ◦C) under high nitrogen pressure (45 kbar) [85]. As a result, crystals of GaN cannot be grown by the standard Czochralski or Bridgeman methods used to grow Si and GaAs boules.

GaN is n-type, due to unintentional impurities. The primary unintentional n-type impurities in GaN are oxygen and silicon. Oxygen and silicon are shallow donors in GaN that reside 0.02 - 0.03 eV below the conduction band [2,86]. The nitrogen vacancy (VN) has been

shown to be a shallow donor at 0.07 eV below the conduction band [86]. The dominant shallow acceptor appears to be the gallium vacancy (VG). Iron is a deep acceptor (0.5 – 0.6 eV below conduction band) in GaN [87]. Semi-insulating GaN is obtained by compensating the shallow oxygen donors with deep iron acceptors. However, iron densities of $10^{17} – 10^{18}$ cm^{-3} are required to compensate for oxygen densities of 10^{15} - 10^{16} cm^{-3}, indicating that only a small fraction of the iron atoms are active [88]. A comparison of some of the transport properties for GaN is given in the Table 5.

2.6 Transport in Semi-Insulating Materials

A perfect insulator exists when there is no conduction of current. Considering a perfect insulator, free of traps with a negligible concentration of free carriers at thermal equilibrium and neglecting the diffusion currents, the current density can then be written as:

$$J = \rho \upsilon = Q/t \quad , \tag{2.1}$$

where ρ is the average injected free charge concentration, υ is the average drift velocity of the free electrons, and Q is the total injected free charge per unit area between the cathode and the anode. The total charge put unit area on the plate of a parallel plate capacitor is given by:

$$Q_0 = C_0 V, \quad and \quad C_0 = \varepsilon / L \quad , \tag{2.2}$$

where ε is the dielectric constant of the medium between the plates and L is the distance between the plates. Using the two above equations, the current density can be written as:

$$J = \varepsilon \upsilon V / L^2 \, . \tag{2.3}$$

The electron drift velocity for relatively low electric fields is: $\upsilon = \mu E = \mu (V / L)$, where μ is the electron mobility and E is the electric field between the cathode and the anode. Substituting Eq. 2.2 into Eq. 2.3 yields the result:

$$J = \varepsilon\mu (V^2 / L^3) \quad . \tag{2.4}$$

This represents the highest one carrier injection current that a given insulator with a specific cathode to anode spacing can carry.

2.6.1 Insulator with Traps

The existence of electron traps in the insulator results in greatly reduced current at low voltages. This is because the injected carriers get captured by electron traps that are initially empty to start with, and thereby restrict (or nearly halt) the current flow through the device. For non-degenerate semiconductors, the free electron concentration at thermal equilibrium is given by:

$$n_0 = N_C \exp[(F_0 - E_C) / kT] \quad , \tag{2.5}$$

where N_C is the effective density of states in the conduction band, E_C is the lowest level of the conduction band energy, k is Boltzmann's constant, F_0 is the Fermi level and T the temperature in Kelvin. The concentration of the filled traps, $n_{t,0}$ is then given by [24]:

$$n_{t,0} = \frac{N_t}{1+\left(\frac{1}{g}\right)\exp[(E_t - F_0)/kT]} , \tag{2.6}$$

where N_t is the concentration of traps and g is the degeneracy factor for the traps. A crucial

factor to remember is that this theory does not consider the change in the trap cross section with respect to the electric fields, so the trapping cross-section is assumed to be constant. Thus, a balance between the free and trapped electrons is reached in order to provide thermal equilibrium conditions. Thus:

$$n = n_i + n_0 = N_C \exp[(F - E_C)/kT] \ , \tag{2.7}$$

$$n_t = n_{t,i} + n_{t,0} = \frac{N_t}{1+\left(\frac{1}{g}\right)\exp[(E_t - F)/kT]} \ , \tag{2.8}$$

where n_i is the average excess injected free electron concentration and $n_{t,i}$ is the average, injected, excess trapped electron concentration.

2.6.2. Shallow Traps

An electron trap at energy level E_t is said to be shallow if E_F lies below E_t. Therefore, from equation 2.6 [24], one gets:

$$\frac{n}{n_t} = \frac{N_C}{gN_t} \exp\left(\frac{E_t - E_C}{kT}\right) = \theta \quad , \tag{2.9}$$

where θ is a constant. The shallow traps of concentration N_t substantially affect the space charge limited injection current if θ <<1. If the Fermi level E_F is below the trap level, as is the case for shallow traps, its location keeps on increasing as carrier injection increases. At some voltage *V*, the E_F level will cross the trap level E_t. This crossover will change the slope of the *I-V* characteristics so that now, most of the trap levels will be filled completely. Hence, all of the injected charge will directly account for the increased current flow. The voltage at which this happens is called *VTFL*, and this phenomenon is known as the Trap Filling Limited (TFL) law

(Figure 5(left)).

For a shallow trap level case, one gets:

$$V_x = (en_0L^2/\theta\varepsilon) \quad . \tag{2.10}$$

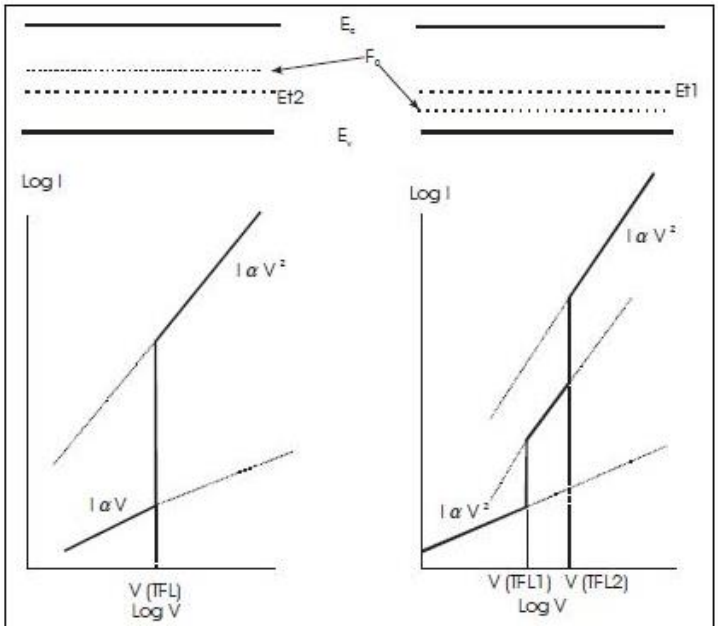

Figure 2.9. I-V characteristics for a deep (left) and shallow trap (right) respectively [24].

2.6.3 Deep Traps

An electron trap is said to be deep if E_F lies below E_t , i.e., $\frac{E_t - F_0}{kT} < 1$. In thermal equilibrium, the number of traps not occupied by electrons (i.e., that are occupied by holes) is given by [24]:

$$p_{t,0} = N_t - n_{t,0} \cong \frac{N_t}{g} \exp\left(\frac{E_t - F_0}{kT}\right) \quad . \tag{2.11}$$

As mentioned for the shallow trap case, Ohm's law will apply until the thermally free carrier concentration, n_0, is higher than the injected free electron charge, n_i. Once these two

become comparable, there will be an upwards shift to the quasi Fermi level from the Fermi level. Since the free electron concentration $n = n_i + n_0$ doubles at the crossover point, there will be a shift in the quasi Fermi level location precisely by 0.7kT. This motion is sufficient to fill all the deep traps. The crossover voltage V_x is:

$$V_x \cong \frac{Q_{TFL}}{C_0} \cong \left(\frac{epL^2}{\varepsilon}\right) , \tag{2.12}$$

where the subscript TFL is used to denote the trap filled limit.

The behavior of the deep and shallow trap levels is shown in Figure 2.9. In both cases one starts with Ohm's law characteristics. In the case of deep traps (Figure 2.9, left), the crossover voltage $V_x$is obtained when n_i becomes equal to n_0. Then, this characteristic coincides with the trap free square law. In case of shallow traps, after following Ohm's law, the current follows the square law given by equation 2.12. Once the Fermi level crosses energy level E_{t2}, the characteristic merges with the trap free square law.

2.6.4 Field-Dependent Emission and Capture at Deep Traps

The electron capture rate is defined as the rate at which electrons are captured from the conduction band by traps. This can be represented as follows:

$$dn/dt = -C_n\, n\, N_n \ , \tag{2.13}$$

where n is the free electron density in the conduction band, N_n is the density of empty electron traps, and C_n is the electron capture rate constant (or simply the electron capture coefficient). The capture cross-section of an electron trapping center is defined as a cross-section through which a

moving electron must come to the center to be captured. The density of empty traps N_n can alternatively be expressed as: $N_n = N_T - N_T^-$, where N_T^- is the density of traps occupied by electrons, and N_T is the total density of traps (filled and unfilled by electrons). For an emission process, the rate can be expressed as:

$$dn/dt = e_n N_T^- \quad . \tag{2.14}$$

Electron capture coefficient C_n can become field-dependent, due to an applied electric field. Therefore, the field dependent capture coefficient can be expressed as:

$$C_n(F) = C_n R_C(F), \tag{2.15}$$

where $R_C(F)$ represents a field-dependent ratio factor. In addition, the emission from traps can also be field-dependent. These will be discussed in Chapter 3 in detail.

2.7 Other Relevant Issues for Photoconductive Switching

A couple of issues relevant and germane to electrical transport and current flow in semi-insulating semiconductors are discussed in this section, for completeness.

2.7.1 Single and Double Injection

As evident from the discussion of the above section, traps can play an important role in fashioning the current-voltage behavior of semi-insulating semiconductors. The filling or emptying of traps can modulate the conductivity and can cause sharp changes in the current. The theory and description of these issues in the previous section was primarily based on single

carrier current injection and flow in a solid. More detailed discussion of such aspects, for an arbitrary distribution of traps in energy and in space, can be found in the literature [89]. In such situations, the voltage-current characteristics of insulators and high-resistance semiconductors include certain ranges of the second voltage in which the current changes are quite substantial. The traps-filled-limit voltage [90] of single injection is the voltage necessary to overcome the barrier to current flow created by charged traps, and was discussed in the previous section.

In double injection, charge carriers of both types (i.e., holes and electrons) are present. The problem then becomes much more complicated because, in this case, the recombination which controls the current-voltage (*J*-*V*) characteristics may either be bimolecular (direct band to band recombination), or may occur through one or more sets of localized traps (indirect recombination). In these situations, the electrons are injected from one contact while the holes are injected from the other. As a result, in the material, the space charge will be partially cancelled by the presence of carriers of both signs. Thus, it is expected that more current would flow in the device than that for the single injection condition. In double-injection devices, electrons and holes are injected simultaneously from two contacts on opposite sides of a sample. Lampert [24] analyzed double injection in a perfectly compensated semiconductor. Ashley [91] expanded this treatment to include an arbitrary occupancy of the recombination centers, a feature essential for a realistic representation of many semiconductors. The double-injection breakdown voltage [92] has been shown to be the value at which both carrier types begin to participate in the current flow mechanism. At this voltage, Lampert [92] has shown that the time of transit between an electrode carrier has become approximately equal to its lifetime. Lampert's model assumes that the semi-insulator contains a single recombination center, which, in equilibrium, is totally occupied by electrons. Since an electron is supposedly capable of recombining only with

an unoccupied center, an injected electron has an essentially infinite lifetime. Consequently, no recombination occurs and the equilibrium recombination-center occupation density is not appreciably disturbed.

Double injection in semiconductors has often been treated by making the problem one-dimensional and finding a numerical solution. The theoretical problem is difficult to treat analytically, since the general expressions for space charge and the recombination kinetics result in non-linear differential equations that are intractable in closed form. Simplifying assumptions involve the use of space-charge neutrality [92,93] or simple recombination kinetics, or both. An analytical solution for the case of low injection into a semiconductor was presented by Ashley and Milnes [91] and was verified by a further numerical solution.

An important effect in the presence of double-injection is the onset of "filamentary currents." Barnett and Milnes [94] have described and verified a theory of filamentary conduction. Various experimental results have also been presented in support of the theoretical basis for filamentary behavior. The physical effect is the bunching of electrons and holes into small filaments of small diameter. The concentration of current flow into such small regions (or pipes) can lead to excessive Joule heating and a high production of heat per unit volume. This can then cause deleterious internal temperature increases within a device and can lead to the generation of local stress or cracks or defects, thermal runaway associated with decreases in thermal conductivity with increasing temperature [74], or other high temperature effects [75]. N analysis of current filamentation due to double-injection and the inherent instabilities in device operation was first discussed by Ridley [95]. It was shown that a bulk differential negative resistance causes the material to be intrinsically unstable, and any voltage or current fluctuation can cause a splitting of the material into regions having different electrical properties from one

another. It was shown that stable states can be reached by the formation of current filaments, in the case of current-controlled differential negative resistance. The principle of least entropy production was shown to lead to the formation of current filaments with an optimum size.

One route for the transition to a filamentary mode is due to double injection. The current magnitude in the device increases as both electrons and holes begin to contribute. This is usually initiated above a certain threshold voltage or current, when the traps within the material get filled and saturated by the carriers flowing in the conduction and/or valence bands. This trap filling increases the carrier lifetimes to the point where this value begins to exceed the device transit time. The flood of both electrons and holes then leads to charge cancellation, and so the net charge density begins to drop. The voltage across the device, therefore, will begin to reduce somewhat. The net effect is a rise in current but with a slight fall in the voltage. A negative differential resistance thus occurs.

2.7.2 Structure for Increased Absorption

The photoconductive switch basically produces an electric current by absorbing photons and converting the energy into electron-hole pairs. For achieving high efficiency, there is a need to harvest as much of the incident radiation as possible and produce the highest photocurrent. Several techniques have been proposed to increase photo-absorption. Most of them rely on employing suitable materials having specific thicknesses in order to tailor the reflection characteristics. This aspect is briefly discussed here. More recent and novel techniques have been proposed that make use of nanoparticle clusters or nano-plasmonic arrays for tailoring the material permittivity [96-98] which influences the reflection coefficients.

Some features of a resonant cavity enhanced (RCE) photo-device are discussed here for completeness. One of the desired features for photodetectors is high quantum efficiency. The quantum efficiency "η" of a photodetector is defined as the probability that a single photon incident on the device generates an electron hole pair which contributes to the detector current [99]. When many photons are present, which almost always is the case, "η" is defined as the ratio of current to photon flux.

The basic idea is shown in Figure. 2.10. It involves placing the photo-switch inside a Fabry-Perot cavity. Placing the device inside a microcavity can have two major advantages. Due to the wavelength selectivity of the microcavity, only resonant wavelengths are admitted or emitted. Resonant radiation undergoes multiple reflections within the cavity, causing its intensity to be amplified. The wavelength selectivity and field amplification of the resonant cavity thus favors absorption and enhances conversion efficiency. Such devices are commonly referred to as resonant cavity enhanced (RCE) devices. RCE photodetectors adopt the highly wavelength selective response of the cavity in which they are situated. They also benefit greatly from the increased amplitude of the resonant field (or in an equivalent picture, the multiple passes of each resonant photon), allowing much thinner absorption regions to achieve nearly unified quantum efficiency. Thinner absorption regions allow higher transit time limited bandwidths, due both to shorter transit distances.

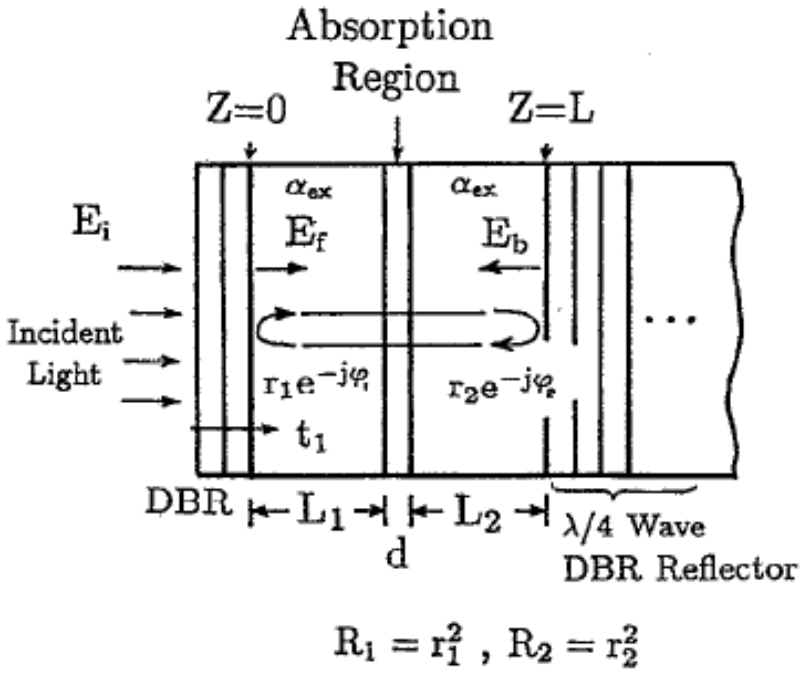

Figure 2.10. Analysis model of a RCE photodetector. The active region of thickness "*d*" is a small bandgap semiconductor. The top and bottom distributed Bragg reflection mirrors consist of alternating layers of non-absorbing larger bandgap materials [100].

Expressions for the conversion efficiency "η" have been worked and reported in the literature [100]. For instance, the efficiency is given as:

$$\eta=[\exp(-\alpha_{ex}L_1)+\exp(-\alpha_{ex}L_2)R_2\exp(-\alpha_c L)][(1-R_1)\{1-\exp(-\alpha d)\}]/[1-2(R_1R_2)^{1/2}\exp(-\alpha L)\cos(2\beta L+\psi_1+\psi_2)+R_1R_2\exp(-2\alpha L)]. \quad (2.16)$$

In the above equation, L_1 and L_2 are the distances on either side of the absorbing layer, as shown in Figure 2.10. In the present situation, $L_1 = L_2 = 0$. In the above equation: $\beta = 2\pi n/\lambda$, where n denotes the refractive index and λ the wavelength of the incident photons. Also, R_1 and R_2 are the reflection coefficients at the z=0 and z=L interfaces, as shown in Figure 2.10, $\psi_{1,2}$ are the associated phase factors, α is the wavelength-dependent absorption coefficient, and *d* is the

thickness of the absorbing layer. Since $L_1 = L_2 = 0$, the term α_{ex} in the above equation drops out, while $\alpha_c \sim \alpha$, and $d \sim L$. As a result:

$$\eta \sim [1+R_2 exp(-\alpha L)][(1-R_1)\{1-exp(-\alpha L)\}]/[1-2\,(R_1R_2)^{1/2}\, exp(-\alpha L)\, cos(2\beta L+\psi_1+\psi_2)+R_1R_2 exp(-2\alpha L)]. \quad (2.17)$$

A representative schematic of the wavelength-dependent efficiency for such a RCE device is shown in the figure below.

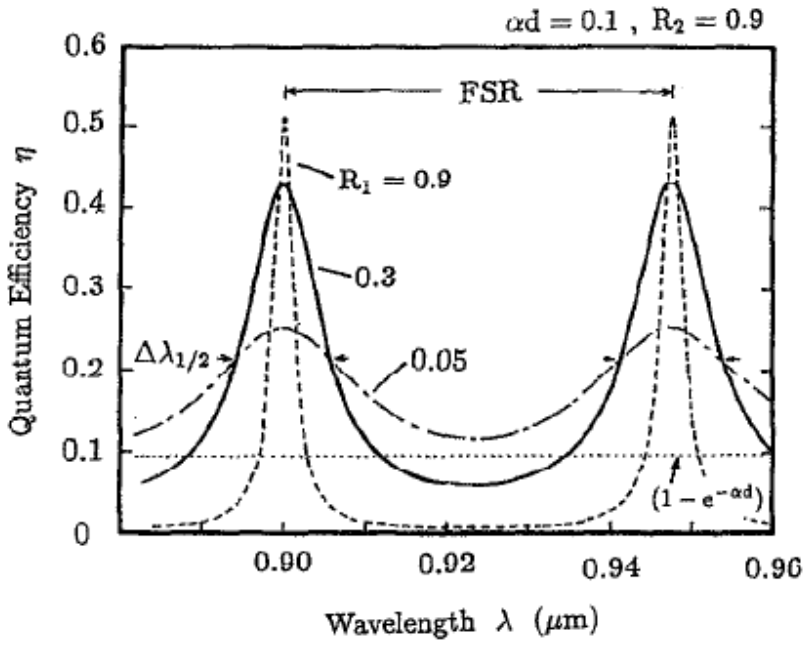

Figure 2.11. Wavelength dependence of η for RCE device having various top mirror reflectivities for fixed L=2 μm, R_2=0.9 and αL=O. [100].

As apparent from the figure above, for high reflectivity values, the quantum efficiency η can be increased by a large amount above the mean value without using any absorption enhancements. Furthermore, these enhancements occur at selective wavelengths. Hence, for a practical photo-

switch, one needs to tailor and design the RCE structure at the wavelength of the external photoexcitation.

CHAPTER 3

SIMULATION METHODS

FOR SIC PHOTOCONDUCTIVE SWITCH ANALYSES

3.1 Model Analysis

This chapter evaluates a 4H-SiC photoconductive switch for pulsed power applications. The transition of carriers from one state (say, non-conducting in the valence band) to another state (e.g., conducting in the conduction band) can be obtained by thermal or optical excitation. Once the carriers are excited into the free-states, they can contribute to the conductivity of the material until they are captured or recombine, or until they are swept out of the semiconductor system. The distribution and motion of carriers within a semiconductor device structure can be obtained by solving the continuity equation for electrons and holes, rate equations for trapping and detrapping kinetics, drift/diffusion current equations for transport, and the Poisson's equation [76,102], given as follows:

$$\frac{\partial n}{\partial t} = G_n - U_n + \frac{1}{q}\nabla.\overrightarrow{J_n} \tag{3.1}$$

$$\frac{\partial p}{\partial t} = G_p - U_p + \frac{1}{q}\nabla.\overrightarrow{J_p} \tag{3.2}$$

$$\frac{\partial n}{\partial t} = \left(c_{ni}n + e_p\right)N_{Ti} - (c_{ni}n + c_{pi}p + e_n + e_p)n_{Ti} \tag{3.3}$$

$$\vec{J}_n = q\mu_n n\vec{E} - qD_n\nabla n \tag{3.4}$$

$$\vec{J}_p = q\mu_p p\vec{E} - qD_p\nabla p \tag{3.5}$$

$$\nabla.\vec{E} = \frac{q}{\varepsilon}\left(p - n + {N_i}^+ - {N_i}^-\right). \tag{3.6}$$

Here, the subscript *i* will denote the i[th] trap. Equation (3.3) represents the rate equations for trapping and detrapping kinetics. This is important when the change in the electron occupancy of the deep traps is significant. The generation rate, *Gn* in equation 3.1, includes an intrinsic ionization process (electron and hole pair generation) [103], photon ionization including two-photon processes [104,105], and electron emission from all the traps. This can be written as:

$$G_n = \alpha_i + \frac{\beta h\nu\phi^2}{2} + \sum e_{ni} n_{Ti} \ . \tag{3.7}$$

The recombination rate, *Un*, consists of direct band-to-band indirect recombination [106], Auger recombination [107,108], and electron capture at all the traps. This can be represented as:

$$U_n = K_d np + \sum c_{ni} n(N_{Ti} - n_{Ti}) + K_a n^2 p. \tag{3.8}$$

Similarly, the generation rate, *Gp*, and recombination rate, *Up*, for holes can be given as,

$$G_p = \alpha_i + \frac{\beta h\nu\phi^2}{2} + \sum e_{pi}(N_{Ti} - n_{Ti}), \tag{3.9}$$

$$U_p = K_d np + \sum c_{pi} p n_{Ti} + K_a n^2 p. \tag{3.10}$$

The capture parameters are functions of the thermal velocity of free carriers [109] and can be written as:

$$c_n = \sigma_n < v_n >, \tag{3.11}$$

$$c_p = \sigma_p < v_p > . \tag{3.12}$$

where σ_n and σ_p are capture cross sections of electrons and holes, respectively. The optical emission at the traps is related to the external photon flux [103],

$$e_n^0 = \sigma_n^0 \tag{3.13}$$

$$e_p^0 = \sigma_p^0, \tag{3.14}$$

where σ_n^0 and σ_p^0 are optical ionization cross sections for electrons and holes, respectively. The thermal capture and emission can be connected by the principle of detailed balance at thermal equilibrium [110],

$$e_n{}^t = (c_n{}^t N_C/g)\exp(-\Delta E_T/kT), \tag{3.15}$$

$$e_p{}^t = (c_p{}^t N_v/g)\exp(-\Delta E_T/kT), \tag{3.16}$$

where ΔE_T represents the energy gap. $\Delta E_T = (E_C - E_T)$ for electrons and $\Delta E_T = (E_T - E_V)$ for holes.

Impact ionization is an essential charge generation mechanism. This results from a collision between a highly energetic conduction-band electron and a valence band electron which is ionized over the band gap which leaves two conduction electrons and a hole. The ionizing electron gains its energy typically in a high electric field. This scattering process can be divided into electron-initiated and hole-initiated ionization. In an electron initiated impact ionization event, an electron with an energy greater than the impact ionization threshold can make the transition to a secondary electron and a secondary electron-hole pair. Analogously, the process can be initiated by holes. The corresponding inverse process is called Auger recombination.

The ionization rate α is defined as the number of electron-hole pairs generated by a carrier per unit distance traveled. The ionization rate of electrons and holes will denote as α_n and α_h respectively. Impact ionization can only occur when the particle gains at least the threshold energy for ionization E_i from the electrical field. It can be derived that minimum energy of $1.5E_g$ is needed where the E_g is the bandgap and the effective masses of both holes and electrons are assumed to be equal. In general, the ionization rates $\alpha_{n,h}$ depend on the probability for the

carriers to reach this threshold energy. Further, this is not only a function of the local electrical field but also of the "history" of the particle [111,112].

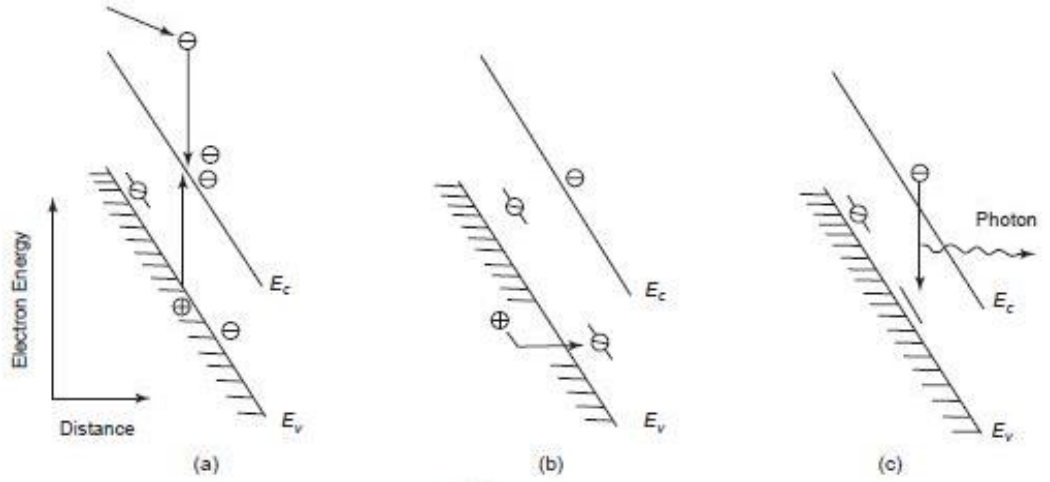

Figure 3.1. Schematic diagram showing the electroluminescence due to the impact ionization. (a) Impact ionization produces a new electron-hole pair; (b) the hole can recombine with an electron in an acceptor state; (c) the electron may then fall into this empty acceptor state, and this results the radiative emission [113].

Electroluminescence can also be the result of impact ionization. Electrons in the conduction band that are accelerated under a sufficiently high field may obtain enough energy to cause impact ionization in the material, resulting in electron-hole pairs, Figure 3.1 (a). Then, the created holes may be trapped at an empty accepter state (Figure 3.1(b)), while the electrons in the conduction band will move. These electrons will move until they find an empty accepter sites, and then will recombine with holes in there, resulting in radiative emission. This is shown in Figure 3.1 (c).

3.1.1 Anode Hole Injection Model

During high-field electron transport, holes in the anode are generated when a significant fraction of the injected hot-electrons lose their kinetic energy either by emitting surface plasmons

or by directly exciting the anode electrons via interband transition or intraband transition [114]. Therefore, the threshold energy for surface plasma excitation and the threshold energy for direct interband electron excitation will be considered. When the electron energy at the anode is comparable to the surface plasmon threshold energy, energy loss via surface plasmon decay becomes more effective than direct excitation [114,115]. When an electron enters in the conduction band of the anode, it loses its energy via direct ionizing collision with a bound electron in the valence band (VB) and creates an electron-hole pair. The rest of the energy of this primary incident electron is shared between the generated electron-hole pair. Back injection into the oxide occurs over the interfacial barrier or via tunneling, althrough it depends upon the energy of the generated hole. The anode hole injection model describes a physical process in which the injected electrons exiting from the cathode lose their energy through impact ionization in the anode to create electron-hole pairs. A fraction of the tunneling electrons reaching the anode are able to elastically transfer their energy to a deep valence-band electron. Such an electron will promote to the lowest available electron energy state, which is the conduction band edge of the anode. This creates a hot hole which tunnels back into the oxide, and thus a trap is created inside the oxide layer. Over time, these traps form percolation paths and lead to oxide breakdown [116-118].

The hole tunneling current density is given as: $J_p=\alpha_p J_n \Theta_p$, where J_n is the incident electron tunneling current density, α_p is the probability for a hole to be generated, and Θ_p is probability for the generated hole to tunnel through the barrier. The quantum efficiency of the hole generation process is:

$$\frac{Jp}{Jn} = \alpha p \Theta_p = \alpha p \exp(-\frac{\hat{B}}{E}\Phi_p^{3/2}) \,, \tag{3.17}$$

where $\hat{B} = 8\pi\sqrt{2m_{p,ox}}/3hq$, $m_{p,ox} = 0.2m_0$ and $\Phi_p = E_{g,SiO_2} - q\Phi_b - E_{gain}$.

In the Fowler-Nordheim (FN) tunneling regime ($V_{ox} > \Phi_b$), the energy gained by the electron, E_{gain} before arrival at the anode can be given as $E_{gain} = q\Phi_b + qE\lambda\{1 - \exp[-\frac{1}{\lambda}(t_{ox} - \frac{\Phi_b}{E})]\}$, where λ is the mean free electron scattering length [95,96]. This is shown in Figure 3.2 (a). In the direct tunneling regime ($V_{ox} < \Phi_b$), electrons do not experience scattering in the oxide, thus the arrival energy of the electrons at the anode, $E_{gain} = q\mathrm{V}_{ox}$. This is illustrated in Figure 3.2 (b).

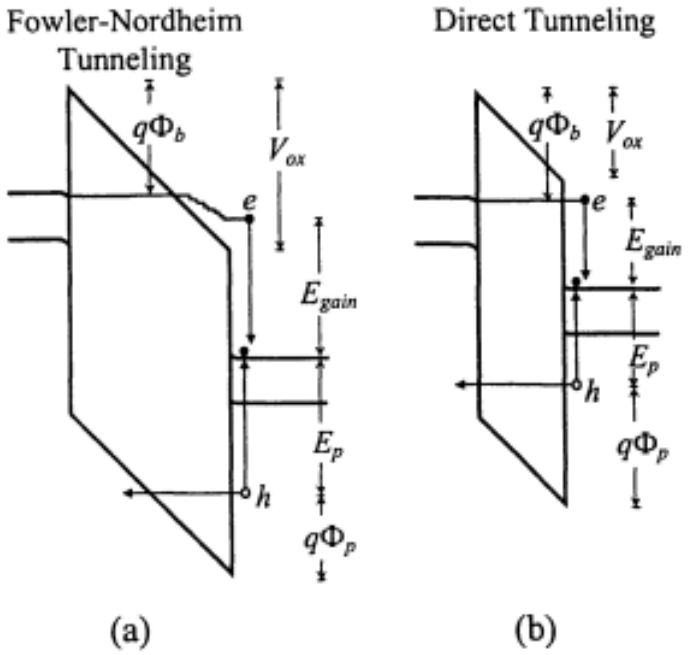

Figure 3.2. Diagram of Anode hole injection process. An incident tunneling electron arrives at the anode with energy E_{gain} to thermalize. This energy is transferred to a deep valence band electron, thereby exciting it to the lowest available energy state, the anode conduction band. This excitation creates a hot hole capable of tunneling back into the oxide [116].

3.2 Mathematical Model for One-Dimensional (1D) Analysis

An analytical theory of space-charge-limited current in high resistivity semiconductors with discrete trapping levels was discussed several years ago by Lampert et al. [24-26]. The

term "relaxation semiconductor" has often been used to define such semiconductors for which the dielectric relaxation time can exceed the recombination lifetime. A more complete description of the current transport was based on computer modeling approaches [119, 120]. In the Mark and Lampert model, trapping of the injected carriers causes the current to remain well below the value in a trap-free insulator, until the applied voltage is high enough to inject enough excess carriers to fill the traps. At this point, called the traps-filled-limit-voltage (V_{TFL}) by Lampert, a rapid increase of current with voltage is predicted, until the current reaches a value corresponding to the trap-free space-charge-limited current and varies as the square of the voltage. A number of investigations were carried out on semi-insulating materials, particularly CdS and GaAs, but as pointed out by Bube [121], they have generally yielded values for trap densities which were much lower than those determined by other experimental methods. It was, therefore, suggested [121] that the sudden increase in current does not take place at V_{TFL}, but at a lower voltage, due to contributions from impact ionization. A similar suggestion has been that impact ionization of impurities, rather than band-to-band ionization, is responsible for the observed *I-V* characteristics [122-124]. Various regimes and additional processes have been identified [125]. Experimental results by Willing and Maan in semi-insulating GaAs [126] have revealed an onset of field-enhanced trapping at lower fields. Furthermore, they observed [126] that the capture coefficient did not saturate at high fields, but instead decreased at high fields, thus yielding local maxima.

For a simple analysis under steady-state equilibrium conditions, based on a 1D rate equation for electrons, one can obtain the following equation for one trap at low electric fields:

$$dn/dt = e_{n0} N_T^- - c_n n (N_T - N_T^-) = 0 \quad , \tag{3.18}$$

where n, N_T and N_T^- are the electron, total trap, and occupied traps densities, respectively, while e_{n0} represents the electron emission rate, and c_n the electron capture cross-section. Thus: $e_{n0} = c_n\, n\, (N_T - N_T^-)/N_T^- \equiv c_n\, P_0$. In equilibrium, the value of $n(N_T - N_T^-)/N_T^- = N_C\, exp[(E_T - E_c)/(k_B T)]$ where E_T and E_c are the energy levels of the trap and the conduction band edge, respectively, and T is the temperature in Kelvin, and k_B the Boltzmann constant. With an electric field F applied, c_n can become field-dependent, and hence symbolically changes as: $c_n(F) \rightarrow c_n\, R_C(F)$, where $R_C(F)$ represents a field-dependent ratio factor. Field-dependent enhancements of the capture coefficient are possible if the trapping process entails a repulsive potential barrier. This occurs because in such a situation, an applied external field increases the average kinetic energy of the electrons, making it easier for them to surmount the potential barrier. Alternatively, on the basis of the Lucovsky model [127], increased quantum mechanical tunneling of electrons through the potential barrier would also increase the capture coefficients. Thus, electron capture rates could increase with field, as long as the field magnitudes were not very large. Such electric field dependence of electron trapping is important and has been shown to lead to domain formation and current oscillations in semiconductor materials. This was later supported by the work of Sacks and Milnes [128]. However, at much higher electric fields, carrier heating would cause the capture rate to decrease, since a long sequence of phonon emissions would then be required for the eventual and successful trapping of mobile electrons. Such a lowering of the capture rate at high fields has been probed in the literature [129-132] and should lead to a maxima for the field-dependent $R_C(F)$ function. It may be mentioned in this context that such behavior would not be valid for hydrogenic traps. However, since one expects deeper defect energies in the wide bandgap SiC material, the existence of such repulsive deep levels is a possibility.

At higher fields, the simple equation 3.18 should be modified to incorporate a field-dependent factor $R_C(F)$ as: $e_{n0} N_T^- = c_n R_C(F) n (N_T - N_T^-)$. This would then yield the following expression for the occupied trap density: $N_T^- = R_C(F) n N_T/[P_0 + R_C(F) n]$. Using the expression for N_T^- in the Poisson equation leads to:

$$dF/dx = - q[n + N_T^-]/\varepsilon_s = - q n \{1 + R_C(F) N_T/[P_0 + R_C(F) n] \}/\varepsilon_s \ . \qquad (3.19)$$

At low electric fields, $R_c(F)$ is expected to be very small due to the repulsive potential barrier for trapping, and so $dF/dx \sim -q n/\varepsilon_s$ represents a Mott-Gurney-like behavior, leaving the traps with virtually little influence on the current conduction. For high electric fields, $R_c(F) > 1$, and one roughly gets: $dF/dx = - (q n/\varepsilon_s) R_C(F) N_T/[P_0 + R_C(F) n]$. So a high field (and hence strong voltage drop) would appear across the device. As a result, the *J-E* curve with traps would shift to higher fields (i.e., move to the right of Mott-Gurney curve) and would have smaller current values. Equation (3.19) can easily be extended for the case of *N* multiple traps at different energies to yield:

$$dF/dx = - q n \ \sum_{i=1}^{N} \{1 + R_{Ci}(F) N_{Ti}/[P_{0i} + R_{Ci}(F) n] \}/\varepsilon_s \ . \qquad (3.20)$$

Additionally, emission from traps can also be field-dependent. In the direction of the applied field, the potential barrier is lowered, and hence, an electron requires less energy to escape from the trap. This field-assisted emission is known as the Poole-Frenkel effect [103,133], and the barrier decreases by an amount $\Delta\varphi_{PF}$. In a simple one-dimensional treatment, the barrier decrease can be given as $\Delta\varphi_{PF} = [(q^3F)/(\pi\varepsilon)]^{1/2}$. As a result, the rate of electron emission from a trap is enhanced by the field, with $e_n(F) \sim e_n(F=0) \exp[\Delta\varphi_{PF}/(kT)]$. A more rigorous three-

dimensional analysis of emission [134] leads to the following, slightly modified expression of the emission rate: $e_{n3D}(F) \sim e_n(F=0)\ \{½ + [(\gamma-1)\exp(\gamma) + 1]/\gamma^2\}$, where $\gamma = \Delta\varphi_{PF}/(kT)$. In addition, the applied field increases the probability for trapped electrons to escape into the conduction band via both elastic and inelastic tunneling [135]. Hence,high field effects on electron emission need to be included in the rate equation analysis, especially in the context of high power devices. This is easily accomplished through the inclusion of a field dependent ratio factor, i.e., $e_n(F) \sim R_E(F)\ e_n(F=0)$, and leads to: $N_T^- = R_C(F)\ n\ N_T/[\ R_E(F)\ P_0 + R_C(F)\ n]$. Hence, the spatial dependence of the electric field from Poisson's equation is:

$$dF/dx = -\ q\ n\ \sum_{i=1}^{N} \{1 + R_{Ci}(F)\ \ N_{Ti}/[\ R_{Ei}(F)\ P_{0i} + R_{Ci}(F)\ n]\ \}/\varepsilon_s \quad . \qquad (3.21)$$

In a situation involving a defect with a repulsive potential and trap density N_{T1}, and another with an attractive potential (i.e., a shallow hydrogenic trap) at a density N_{T2}, the above is modified to:

$$dF/dx = -\ q\ n\ [\ \{1+R_{C1}(F)\ \ N_{T1}/[R_{E1}(F)\ P_{01} + R_{C1}(F)\ n]\} + N_{T2}/[\ P_{02} + n]]/\varepsilon_s\ . \quad (3.22)$$

The above treatment can be extended to include both attractive and repulsive traps, field-dependent emission, and band-to-trap impact ionization. Algebraic manipulation leads to the following general equation for the case of a semi-insulating semiconductor with N different repulsive defects and M separate attractive traps, and trap-to-band ionization:

$$dF/dx = -\ (q\ n/\varepsilon_s)\{1 + \sum_{k=1}^{N} c_k R_{Ci}(F) N_{Tk}/[c_k P_{k0} R_{ek}(F) + c_k R_{Ck}(F)\ n + n\ R_{iik}(F)] +$$

$$+ \sum_{l=1}^{M} c_l N_{Tl}/[c_l P_{l0} R_{el}(F) + c_l\ n + n\ R_{iil}(F)]\} \quad , \qquad (3.23)$$

where $R_{iik}(F)$ and $R_{iil}(F)$ are field dependent impact-ionization factors for electron collision-induced impact ionization from traps with repulsive and attractive potentials, respectively.

Here, the field dependent impact-ionization factors $R_{iip}(E)$ were taken to be a function of the local electric field. A similar approach had been used for band-to-trap processes in SiO_2 [136], another wide-bandgap material. Conceptually, the process is similar to that of electron ionization from the subbands of quantum well superlattices. Strictly, computations of the threshold energy for impact-ionization require momentum and energy conservation, taking account of the detailed bandstructure. However, for simplicity, the threshold values were taken to be fitting parameters. Similarly, empirical forms were assumed for the impact-ionization factors $R_{iip}(F)$ of the type $R_{iip}(F) \sim R_{0p}\, exp(\alpha_p |F|)$, and values of R_{0p} and α_p were extracted from comparisons to the data. A more exact approach could perhaps include details of the electron distribution function at each location (i.e., discretized position within a device) via a Monte Carlo (MC) scheme with inclusion of internal scattering processes and the bandstructure. For example, the energy-dependent ionization rates discussed by Robbins [137] could be folded into a MC simulation.

Finally, for completeness, a brief discussion of carrier drift velocity is presented, since it influences the current density, in addition to the local electron density. For 4H-SiC material, the electron drift velocity v_{dr} was taken to be [138]:

$$v_n(F) = [\mu_{n1} |F| + \mu_{n0} |F| (|F|/F_0)^{\theta} + v_{sat} (|F|/F_1)^{\eta}]/[1 + (|F|/F_0)^{\theta} + (|F|/F_1)^{\eta}] , \qquad (3.24)$$

where $\eta = 3$, $\theta = -1.95$, $F_1 = 2.8 \times 10^7$ V/m, $F_0 = 3.05 \times 10^6$ V/m, $\mu_{n0} = 4 \times 10^{-3}$ m^2/Vs, and $\mu_{n1} = 0.68 \times 10^{-3}$ m^2/Vs.

3.3 Numerical Implementation for Drift-Diffusion Analysis

Several assumptions have been made in order to perform the one-dimensional simulations based on the drift-diffusion approach discussed in Section 3.2. Under the steady state condition, the diffusion is neglected. Also, only one type of carrier was considered, which wereelectrons. Implementation of the semiconductor equations for transport for the purposes of obtaining numerical analyses was based on the equations given in the previous section. A central difference technique was used to solve the differential equations. The program was written using the MATLAB software, and a block diagram for the numerical computation by the technique is shown in Figure 3.3.

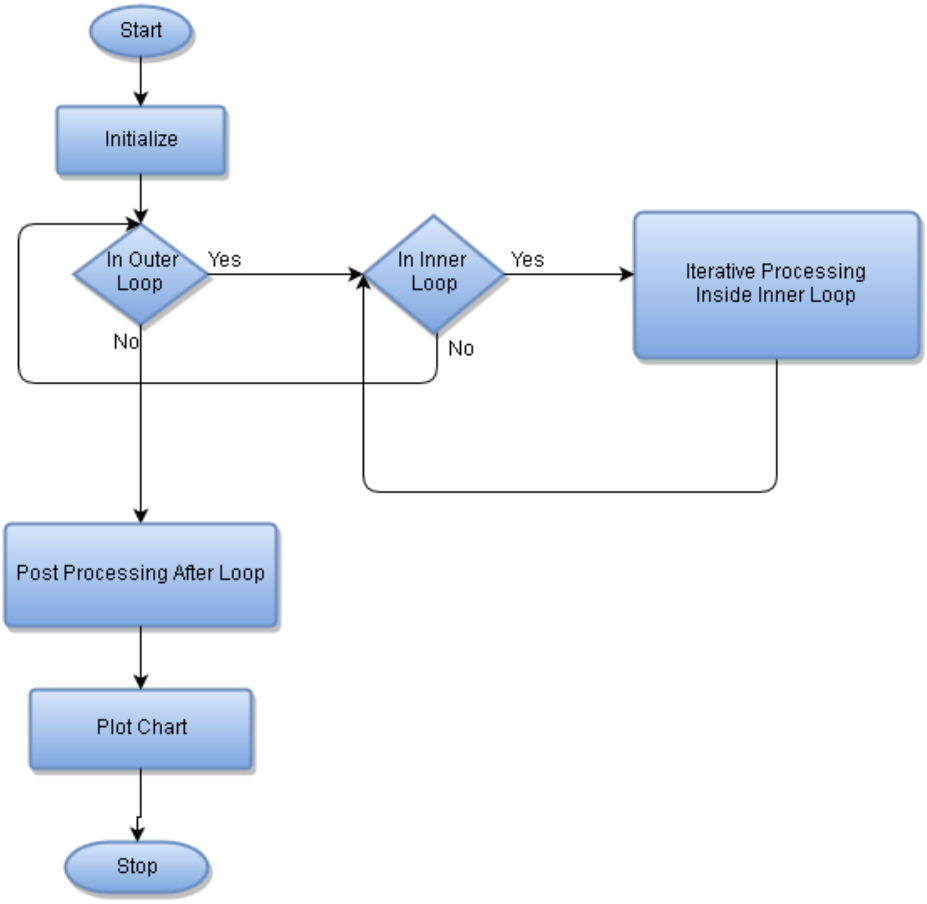

Figure 3.3. Numerical computation for the steady state analysis.

As shown in Figure 3.3, for a corresponding current density, the *J* value of the average electric field value was calculated. Here, the average electric field was found, assuming that the whole system is a one dimensional grid with N points. Figure 3.4 shows the schematic diagram which has been used in order to evaluate the current voltage characteristics of the 4H-SiC photoconductive switch.

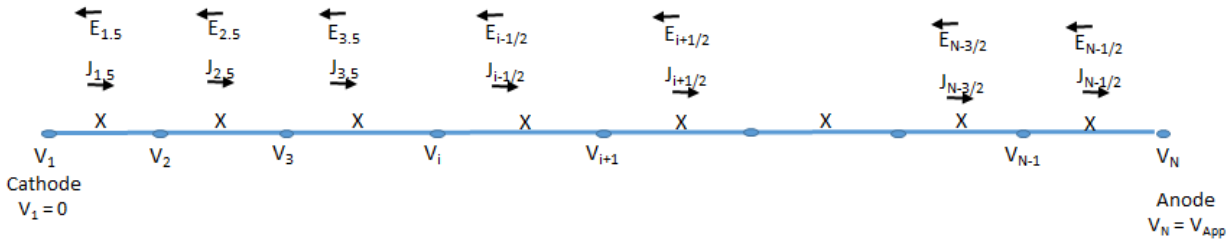

Figure 3.4. Schematic diagram of the 1-D 4H-SiC.

Initially, all voltages are zero at t=0, i.e., $V_i = 0$ for all points *i*. The Scharfetter-Gummel scheme was used for current computations. This scheme treats the current density *J* and the electric field to be constant between *N* grid points, and these are designated as $J_{i-½}$, $J_{i+½}$, and $E_{i-½}$, $E_{i+½}$ etc. [139].

The parameters used in the simulation are listed in Table 3.1. Analysis of high field effects on the steady-state current-voltage response of semi-insulating 4H-SiC was carried out with several models. First, a model with one trap and linear velocity ($v=\mu E$) was considered. Then, keeping the $v=\mu E$, multiple traps were considered. Further, $v=v(E)$ selected and the number of traps was varied. Moreover, multiple traps with impact ionization for traps with repulsive potentials, as well as attractive potentials and the Pool-Frenkel effect, were considered.

Table 3.1. The parameters used in the simulation

Parameter name	**Value**
Permittivity, $\boldsymbol{\varepsilon_s}$	8.54x 10^{-11} F/m
Permittivity of SiC, $\boldsymbol{\varepsilon_{SiC}}$	9.7
Temperature, T	300 K
Boltzmann Constant, k_B	1.38×10^{-23}
Reflectivity, r	0.5
Electron charge, q	1.6×10^{-19} C
A_0	1.2×10^{6}
Length of the material, L	4.54×10^{-4} m

Trapping causes spatial localization of electrons and holes at certain sites and hence, stops the carriers from contributing to electrical conduction. Any site which is created by localized states and is capable of capturing carriers is called a trap or a trapping center. These traps can have a charge, depending on the occupancy of the charge. This charge will determine the behavior of the trap. Thus there are three types of traps: coulombic attractive centers, coulombic neutral centers, and coulombic repulsive centers. The energy profiles near the trapping sites are different for the different kinds of traps, as shown in Figure 3.5, below.

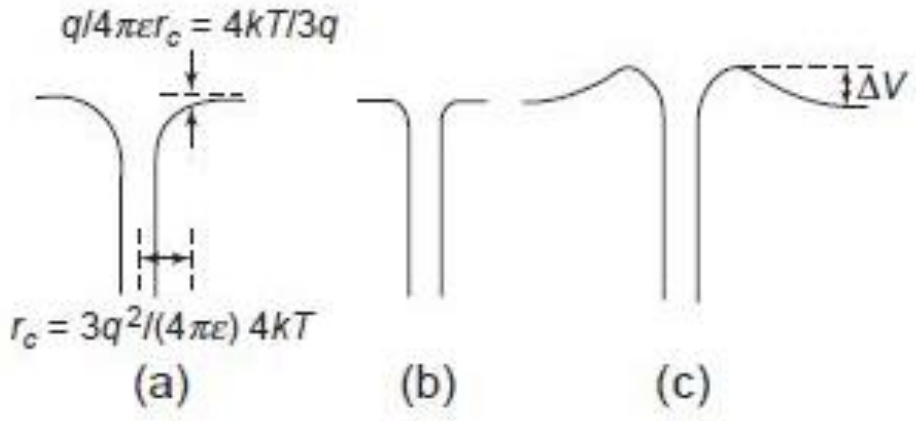

Figure 3.5. Schematic diagrams illustrating the variation of potential energy of (a) coulombic attractive center, (b) coulombic neutral center, and (c) coulombic repulsive center [113].

The capture cross-section of a center is determined by the variation of potential energy around the center. For repulsive centers, the capturing action is repulsive. An electron approaching a center that has already captured an electron will see a repulsive potential barrier. This approaching electron will have to overcome this potential barrier, thermally, or tunnel through before being captured. Figure 3.5(c) shows that when the free electron reaches the potential top (ΔV), it sees an attractive potential field. This kind of trapping process indicates that the repulsive centers will have small capture cross-sections and will be very sensitive to temperature. Further, the increasing electric field will increase the number of high-energy electrons to overcome the repulsive potential barrier and be trapped. This phenomenon is known as field-enhanced trapping. In general, the trapping cross-sections follow the following relation:

$\sigma_{attractive} > \sigma_{neutral} > \sigma_{repulsive}$.

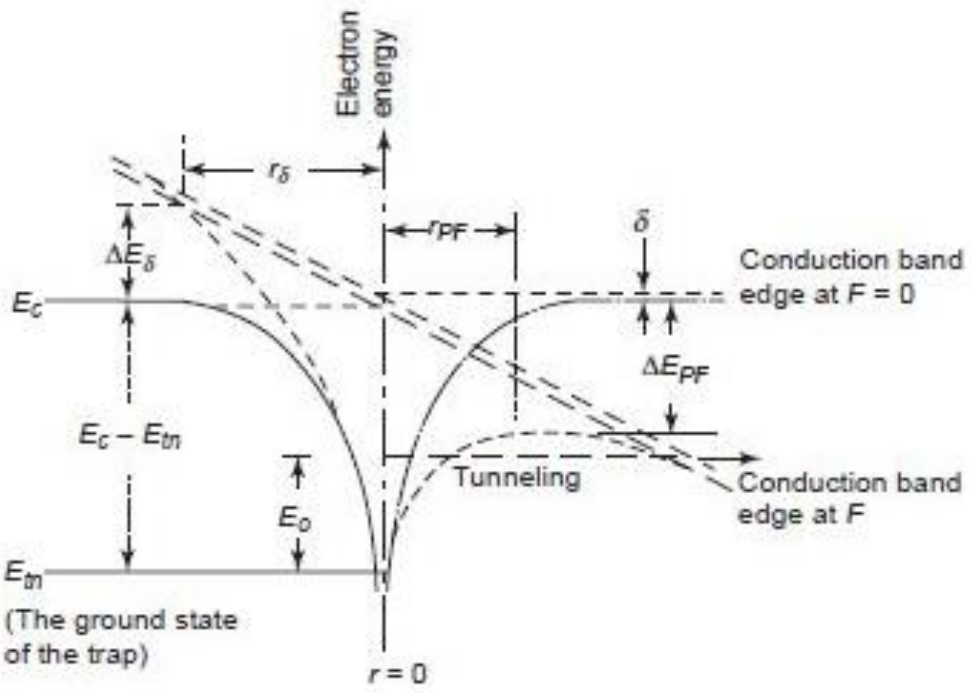

Figure 3.6. Schematic diagram illustrating the Poole-Frenkel effect [113].

In addition to trapping, there can also be carrier detrapping (or release) from the traps. One such process is the Poole-Frenkel mechanism, shown schematically in Figure 3.6. The application of an external electric field will lower the Coulombic potential barrier, as seen in Figure 3.6. Thus, this will effectively lower the trap barrier. The Poole-Frenkel effect is also known as the internal Schottky effect. The mechanism of this Poole-Frenkel effect includes the field enhanced thermal excitation (or detrapping) of trapped electrons or holes, which is very similar to the Schottky effect in the thermionic emission. But for the Poole-Frenkel trapping barrier, the positive charge is fixed, while the positive charge is a mobile image charge for the Schottky barrier. Further, the results in the barrier lowering, due to the Poole-Frenkel effect, are twice that that of the Schottky effect. The effect of an applied field in lowering the potential barrier for a trapped electron to escape in a one-dimensional model is illustrated in Figure 3.6.

The solid line represents the Coulombic barrier without a field, and the dashed line shows the effect of an electric field on the barrier. The slope of the double dashed line is proportional to the applied field [113]. The amount of the barrier lowering due to the Poole-Frenkel effect can be written as:

$$\Delta E_{pF} = (\frac{q^3 F}{\pi \varepsilon})^{1/2} = \beta_{pF} F^{1/2}, \tag{3.25}$$

where β_{pF} is called the Poole-Frenkel constant.

$$\beta_{pF} = (\frac{q^3}{\pi \varepsilon})^{1/2}. \tag{3.26}$$

The Poole–Frenkel effect is effective only for traps that are neutral when filled and positively charged when empty. Traps that are neutral when empty and charged when filled will not face this effect due to lack of coulombic interaction. The Poole-Frenkel model can be used to interpret high-field transport phenomena in insulators and semiconductors. [140-143]. The Poole-Frenkel effect is observed when electric conduction is bulk limited, whereas the Schottky effect can be observed when electric conduction is electrode-limited. A trapped electron can be thermally released in the forward direction of the applied field and also in the reverse direction, but the probability of the reverse direction will be smaller. The probabilities for a trapped electron to be thermally released in the forward and the reverse direction are field dependent.

Frenkel derived the expression for the barrier lowering which is given in the equation (3.25), using a one-dimensional model [133, 141], as:

$$\sigma = \sigma_0 \exp\left(\frac{\beta_{pF} F^{\frac{1}{2}}}{2kT}\right), \tag{3.27}$$

where σ_0 is the low-field conductivity. Three-dimensional treatment gives field and temperature dependent conductivities, and this will be different from the Poole-Frenkel relation (3.27). This three dimensional treatment can be presented as follows [142]:

$$\text{for } \alpha F^{1/2} \leq 2\gamma, \qquad \sigma = \sigma_0 \left(\frac{4\gamma}{\alpha^2 F}\right) \sinh(\alpha^2 F/4\gamma), \tag{3.28}$$

and for $\alpha F^{1/2} \geq 2\gamma$,

$$\sigma = \sigma_0 \left(\frac{1}{\alpha^2 F}\right) \left[\left(\alpha F^{\frac{1}{2}} - 1\right) \exp\left(\alpha F^{\frac{1}{2}} - \gamma\right) - 2\gamma \exp(-\alpha^2 F/4\gamma) + \exp(\gamma)\right], \tag{3.29}$$

where $\alpha = \beta_{pF}/2kT$ and $\gamma = \delta/2kT$.

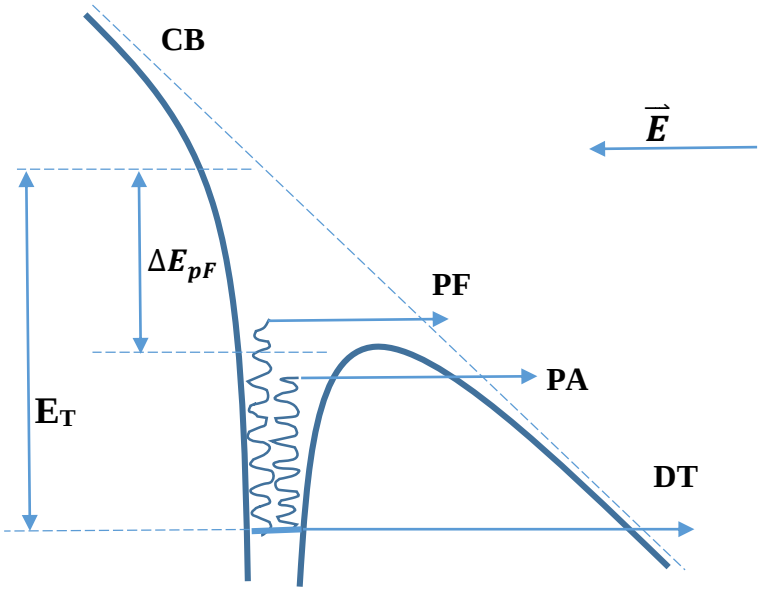

Figure 3.7. Energy diagram of the trapping center in the presence of the electric field. Arrows indicate the possible electron emission mechanisms: PF represents the thermal ionization over the lowered barrier, PAT represents phonon assisted tunneling, and DT represents the direct tunneling into the conduction band (CB) [144].

It is obvious that, at low fields, $\frac{\alpha F^2}{4\gamma} \ll 1$ the conductivity follows a simple Ohm's law. At high fields, equation 3.29 reaches the equation 3.27. Some of the other mechanisms for de-

trapping, which include direct tunneling (DT), phonon-assisted tunneling (PAT), and Poole-Frenkel (PF) emission, are all sketched in Figure 3.7 for clarity and completeness [144].

3.4 COMSOL Computations for Inclusion of Multi-Dimensional and Thermal Analyses

An issue of increasing concern, as power levels scale up, is device reliability. In particular, recent work by our group has shown crack formation in the SiC at the SiC/metal interface [21] in a variety of different device configurations and structures. It was hypothesized that the underlying cause of the observed cracks was either the result of large current densities at the SiC/metal interface during operation, which could then also lead to localized hot spots, or the effect of high electric fields at the contact-SiC interface. Regardless of the origin, experimental optical microscope images confirm that the cracks form primarily near the surface and at points of greatest field enhancement [21].

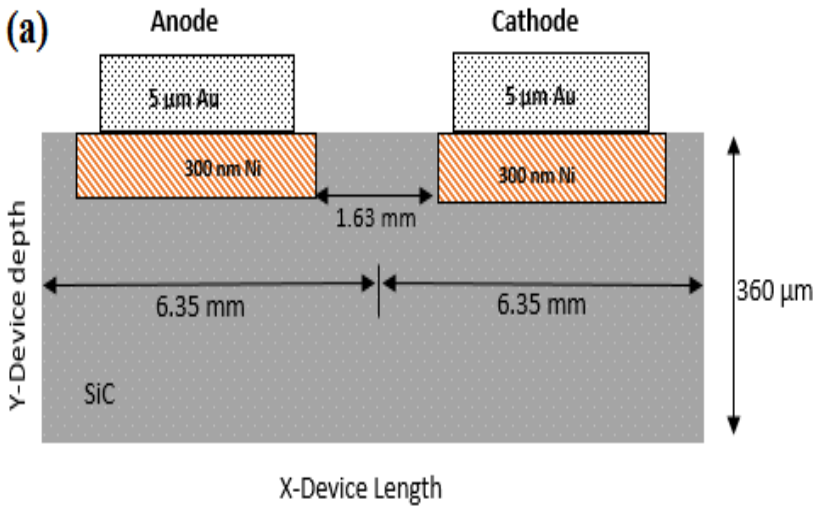

Figure 3.8. Schematic of the basic geometry of the 4H-SiC PCSS, as reported in Mauch et al. [21].

A typical SiC-based PCSS structure is shown in Figure 3.8. The electric fields and voltage distributions are inherently two-dimensional (2D), at least. Hence, a more appropriate analysis requires a two-dimensional (if not a three-dimensional) study. This aspect is discussed in this section. The 2D analysis and simulations in this dissertation research have been carried out using COMSOL, a commercial software. This is a multi-physics simulation tool that embeds and allows for the integration of electrical responses, and thermal aspects including temperature increases due to device self-heating, and allows for the inclusion of other aspects, such as fluid flow, etc.

High electric field driven device failures are well known. Detrimental effects can arise from the production of hot electrons [28] having sufficient energy to generate an electron-hole avalanche by impact ionization and to increase the local temperatures. Thermal expansion could then lead to high stress or even cracking in the vicinity of the hot spots. For completeness, a second, though not so well recognized, mechanism under high field operation is associated with the inverse piezoelectric effect (IPE) [29, 30]. The basic source is the piezoelectric nature of a material that leads to strain under externally applied electric fields. The internal strain can create defects causing eventual degradation and increases in device resistance, due to time-dependent trap generation. This aspect would certainly be detrimental to photoconductive operation, since low ON-state resistance values are typically desired. However, it may be mentioned that there are differences between the hot electron (HE) scenario and the IPE. For example, at higher temperatures, the electron mean free path (which is dictated by phonon scattering) typically becomes shorter. Hence, a higher electric field (i.e., higher device bias voltage) is then necessary to drive hot electrons beyond the impact ionization threshold, thus weakening the role of hot electrons. However, in the case of the IPE, higher temperatures would make it easier to cause

stress and crack formation, as these processes are governed by Arrhenius-type activation energy barriers. In the present context though, the IPE is not expected to be very significant, since the piezoelectric constants for SiC are not large. However, there could be a role, if localized temperatures are not contained.

In any event, regardless of the exact mechanism, it is clearly beneficial to be able to mitigate the peak electric fields, or at least to re-shape their distribution towards greater uniformity with suppression of spatially localized peaks. Only then could one achieve the full performance potential of SiC devices for high power applications. One specific aim in the context of the observed SiC failures would be to reduce the peak electric field values in the neighborhood of the metal-semiconductor interface with non-negligible carrier densities. Proper design of the edge terminations is necessary to reduce the well-known field crowding at the edges.

The two-dimensional (2D) electrostatics for field and potential distributions across the SiC PCSS structure were based on solutions of the Poisson equation using the COMSOL Multiphysics software. COMSOL Multiphysics™ is a commercially available software package, which evolved from the FEMLAB Finite Element Analysis (FEA) tools [145]. It provides a CAD interface to define the geometry, a sophisticated mesh generation capability, and a wide array of numeric solver and post-processing tools.

3.4.1 COMSOL Description and Details

In addition to its general partial differential equation (PDE) solver capability, COMSOL offers application specific modules, each tailored to solving specific types of physics and engineering problems including Chemical Engineering, Acoustics, Earth Science, and many

others. These modules, in turn, contain application modes, which specify the form of the governing PDE to be solved, and allow the user to specify all coefficients, boundary conditions, and initial conditions. The coefficients may be functions of the spatial coordinates, functions of the dependent variable for which we are solving, or, in the case of a multi-physics model, may be dependent on the output of another coupled application mode. The Semiconductor Module has been used in this work. The Semiconductor Module allows for detailed analysis of semiconductor device operation at the fundamental physics level. The module is based on the drift-diffusion equations, using isothermal or nonisothermal transport models. COMSOL uses different solver algorithms for stationary or time dependent problems, both of which can simulate linear or nonlinear models. There is also an eigenvalue solver for the study of natural harmonic oscillations.

Many of the most interesting problems to be solved are non-linear. One can easily define such a model, and COMSOL will automatically use its non-linear solver. The COMSOL nonlinear solver uses a modified Newton method. The user must supply an initial state, $\boldsymbol{U_0}$, for the dependent variable. A linearized model is formulated around the initial state, in the form:

$$J(U_0).U = B(U_0), \tag{3.30}$$

where U is the vector of dependent variable values at the nodes, U_0 is the initial state of U, B is a vector that depends on boundary conditions, and J is often referred to as the system stiffness matrix or the system Jacobian matrix. If this were a linear problem, we would simply solve for the vector U. Since U_0 is not an exact solution, the residual error is:

$$R(U) = J(U_0).U - B(U_0). \tag{3.31}$$

The iterative Newton method can be applied in the usual way, expanding *R(U)* in a Taylor series, dropping all but the first order term, and setting it equals to zero. The resulting equation can be solved for the Newton step δU,

$$J(U_0 + \delta U) = - R(U_0) , \tag{3.32}$$

where $R(U_0)$ is calculated by setting U in Eq. (3.31) equal to U_0, and noting that the Jacobian $\frac{d}{dU} R(U)$ is in fact the system Jacobian $J(U_0)$. The next iteration is then computed as $U_1 = U_0 + \delta U + \lambda$. If the damping factor λ is one, then this is the traditional Newton method; however COMSOL will reduce the damping factor and will recompute U_1 if the relative error is larger than the previous value. The purpose of this damping factor is to make the process converge for a broader range of initial value. COMSOL will compute the relative error, E, for the new iteration U_1 as:

$$J(U_0).E = - R(U_1). \tag{3.33}$$

The term Multiphysics refers to problems defined by a coupled system of differential equations with more than one dependent variable. When using COMSOL to solve such problems, this generally means creating the corresponding model using two or more of the application specific modules. The coupling is specified by symbolically defining the PDE terms and boundary conditions. The COMSOL software will solve all the equations as one fully coupled system.

Here in this dissertation research, a 2D triangular mesh with manual refinement was used, with maximum and minimum mesh sizes set to 0.2 and 0.002 μm, respectively. This finite element COMSOL Multiphysics model was also used to determine the internal device heating.

The current flow leading to power dissipation represented the heat source. Boundary conditions used for the calculations were: (i) Zero charge condition for all the exterior boundaries (i.e., $n.D$ =0 where D is electric displacement, and n the unit normal); (ii) Charge conservation [i.e., $n.(D_1\text{-}D_2)$=0] for interior boundaries with zero surface charge; and (iii) Potentials V_K = 0 and V_A were set for the cathode and anode contacts, respectively.

Temperature changes due to device operation were analyzed using the COMSOL Heat Transfer module. The governing equation upon neglecting viscous heating and pressure-work terms is:

$$\rho\, C_p \frac{\delta T}{\delta t} - \nabla.(\mathrm{k}\nabla T) = Q - \rho\, C_p\, \boldsymbol{u}.\nabla T \quad , \tag{3.34}$$

where k is the thermal conductivity ($Wm^{-1}K^{-1}$), ρ is the mass density (kgm^{-1}), C_p is the specific heat capacity at constant pressure ($JKg^{-1}K^{-1}$), T is the absolute temperature (K), Q the heat source term (Wm^{-3}), and $\boldsymbol{u}$ the velocity vector. If both radiation and convection effects are excluded, equation (3.34) simplifies to:

$$\rho\, C_p \frac{\delta T}{\delta t} - \nabla.(\mathrm{k}\nabla T) = Q \ , \tag{3.35}$$

Thermal boundary conditions were assigned, as discussed by Menozzi et al. [146]. The bottom surface was maintained at 293° K, while the top SiC surface and the remaining exterior model boundaries were considered adiabatic. The power dissipation value across the SiC was taken to be $E\,J$ (W/m^2), with E being the electric field values at the interface and J the PCSS current density. The later was calculated as $n_s\, q\, \upsilon(E)$ with $\upsilon(E)$ being the field-dependent electron drift velocity.

CHAPTER 4

SIMULATION RESULTS AND DISCUSSION

4.1 Introduction

Simulation results were obtained for the current density *J* through the 4H-SiC samples as a function of the applied bias, based on the theory presented in the previous chapters. In performing the calculations, values of the current density *J* and electric field *F(0)* at the cathode (as a boundary condition) were chosen and held fixed. Diffusion was neglected, so the entire current was assumed to arise from electron drift. Equation (3.24) was then used to obtain the spatial profile of the internal electric field for a set of chosen *J, F(0),* and the other parameters selected for trap densities, cross-sections, field-dependent functions $R_{iip}(F)$, $R_{ci}(F)$, $R_{ek}(F)$, etc. The electron density *n* needed for the numerical evaluation of equation (3.23) was obtained from the chosen current density *J* as: $n = J/[q\, v_n(F)]$, with equation (3.24) being used for computations of the drift velocity $v_n(F)$. Vertical contacts at the top and bottom ends on opposite surfaces at a distance of 0.454 mm were assumed, in keeping with the experimental data from the samples.

4.2 Simulation Results of Steady State Current-Voltage Response

4.2.1 Non-Irradiated SiC Samples

Figure 4.1 shows results of the *J-F* calculations, with *F* being the average electric field from a SiC sample that was received from CREE Corporation. This was not irradiated, or annealed, and represents an "as is" sample. In addition to numerical simulations, the actual

experimental data for the silicon carbide sample (say, denoted as SiC2) is also included, in order to compare the accuracy of the simulation results. The experimental measurements were obtained by a group at Texas Tech University. The two curves appear to be in fairly good agreement with the electric field, spanning values from about 10 kV/cm to 170 kV/cm. The boundary condition for the electric field at the cathode works out to be: $|F(0)| = 0.1$ V/m. The current density J ranges over several orders of magnitude from roughly 5×10^{6} A/m^2 to 1 A/m^2.

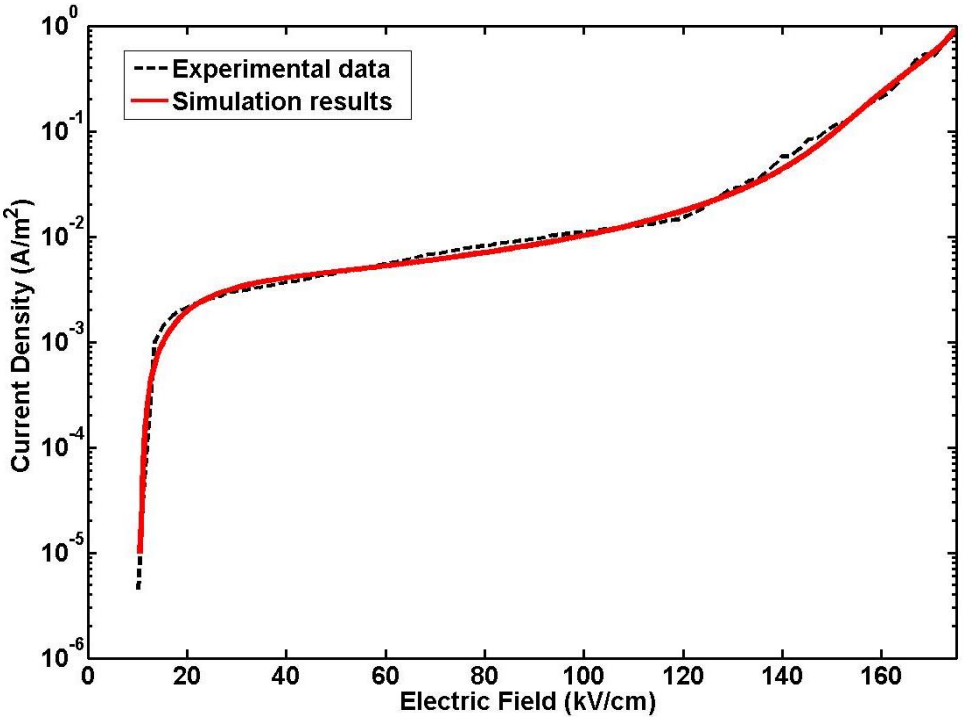

Figure 4.1. Comparison between the simulation *J-F* results and the experimental data for semi-insulating 4H-SiC for sample without irradiation.

The fit between the data and the simulation results was achieved by using three sets of traps in the 4H-SiC material with densities of $N_{T1} = 4.5\times10^{19}$ m^{-3}, $N_{T2} = 6.5\times10^{20}$ m^{-3}, and $N_{T3} = 4.5\times10^{18}$ m^{-3}. Of these, traps 1 and 3 were assumed to have a repulsive potential. Table 4.1 shows these simulated results. Trap energy values derived from the comparison between simulation results

and the data were 0.263 eV, 0.333 eV, and 0.383 eV, below the conduction band-edge, as illustrated in Figure 4.2.

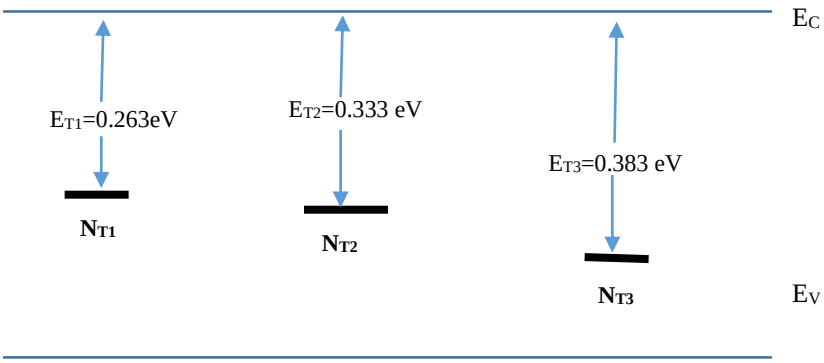

Figure 4.2. Schematic diagram of the traps in the SiC material.

Table 4.1: Simulation results for the trap densities and the locations below the conduction band-edge

Trap	**Trap Density/ m^{-3}**	**Type of the trap**	**Gap between the trap and the conduction band / eV**
Trap1	4.5×10^{19}	Repulsive Potential	0.263
Trap2	6.5×10^{20}	Attractive Potential	0.333
Trap3	4.5×10^{18}	Repulsive Potential	0.383

Comparison of data has yielded the values for the field dependent rates and functions.

- The low-field electron capture cross-sections for the traps were taken to be $c_n = 10^{-17}$ m^2.
- The field-dependent ratio factor was taken to have the form $R_C = [exp(a|F|)-1]$, where $a = 8\times10^{-7}$ m/V.
- The field dependence of $R_E = exp(b|F|)$ yielded $b \sim 8\times10^{-7}$ m/V.

- The threshold field for band-to-trap ionization for the three defect levels were 1.4×10^7 V/m, 1.65×10^7 V/m, and 1.75×10^7 V/m.
- The impact-ionization factor was assumed to be $R_{iip}(F)= a_1 \exp(b_1 |F|)$, and the curve fitting to the data yielded $a_1 = 10^8$ and $b_1 = 10^{-6}$ m/V for traps 1 and 3, and $a_1 = 5\times10^8$ and $b_1 = 10^{-6}$ m/V for trap 2. This is shown in Table 4.2.

Table 4.2: Impact-ionization parameters for the three traps

Trap	**$R_{iip}(F)= a_1 \exp(b_1 \|F\|)$ m/V**	**Threshold Field V/m**
Trap1	$10^8 \exp(10^{-6} \|F\|)$	$E_{t1}=1.4\times10^7$
Trap2	$5\times10^8 \exp(10^{-6} \|F\|)$	$E_{t2}=1.65\times10^7$
Trap3	$10^8 \exp(10^{-6} \|F\|)$	$E_{t3}=1.75\times10^7$

Results obtained for the internal electric fields within the SiC2 sample are discussed next. Two different device current densities from Fig. 4.1 were chosen: a relatively low value of -4.54×10^{-3} A/m^2 (for average 50 kV/cm field) and a higher current density of -7.29×10^{-2} A/m^2 (at an average field of 150 kV/cm). The negative sign is simply the result of our chosen orientation, with the anode at x = 0.454 mm and the cathode at x=0. The internal electric field profile is indirectly indicative of the spatial electron distribution and is influenced by internal processes, such as band-to-trap ionization.

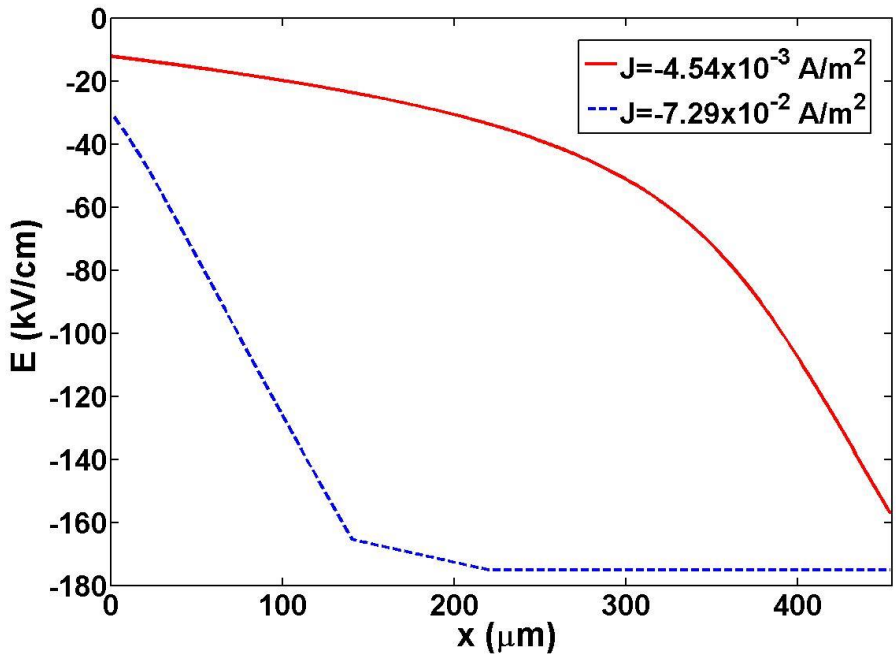

Figure 4.3. Calculated internal electric field profiles for the SiC2 sample at two steady-state current densities of -4.54×10^{-3} A/m^2 and -7.29×10^{-2} A/m^2.

In going toward the anode, the electric field magnitude shown in Figure 4.3 increases and reflects the decreasing free electron density with position. Electrons are injected from the left (cathode) side, and gradually reduce in density toward the anode side, due to capture by one of the three trap sites. The condition of a spatially constant current density J [$= n\, q\, v_n(F)$] value in the steady-state for a given bias requires reductions in free electron density n, as the electric field magnitudes (and hence the drift velocities) increase.

Furthermore, for the -4.54×10^{-3} A/m^2 curve in Figure 4.3, the slope of the electric field progressively becomes larger, with distance implying a higher charge density towards the anode. The higher charge density is associated with a larger population of occupied traps. Since two repulsive defects were assumed here, with their capture rates increasing with local electric field, more such traps would be filled by electrons toward the anode side, due to the higher driving

fields. Thus, for this scenario, the contribution of a negative charge at the filled traps toward the anode side outweighs the smaller free electron density in this region to yield an overall higher net charge density. This situation is representative of low levels of electron flow in a trap-filled, semi-insulating semiconductor. Figure 4.4 shows the electron density variation at given current density values. As was predicted from the Electric field plots in Figure 4.3, electron density decreases when going towards the anode. Here, the density at the anode is not shown.

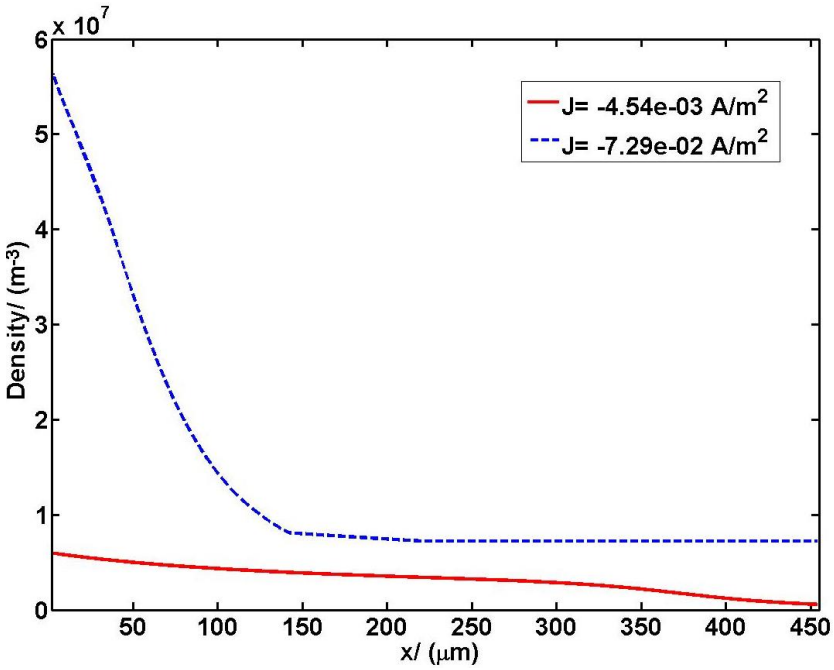

Figure 4.4. Calculated Electron density variation for the SiC2 sample at two steady-state current densities of -4.54×10^{-3} A/m^2 and -7.29×10^{-2} A/m^2.

At the higher current density of -7.29×10^{-2} A/m^2, on the other hand, the values and shape of the electric field profile are somewhat different. The electric field magnitude is again an increasing function of distance from the cathode. As before, the free electron densities are lower over regions of higher field magnitudes, since the drift velocities are higher. However, a sharp change in slope is seen at around the 150 micron location, when the electric field reaches -1.65×10^{7} V/m. This field corresponds to the threshold for the trap-to-band impact ionization

chosen in our model for trap N_{T2}, which is the most populous. Beyond this spatial point, the free electron density begins to increase, as trap-to-band ionization begins to contribute.

Also, as shown in Figure 4.3, the electric field crosses the chosen threshold for trap-to-band ionization from N_{T3} at about 220 μm, for this applied bias. As a collective result, the current density in the SiC sample begins to increase dramatically at high biasing and leads to a high sample conductance. In addition, at this high applied biasing level, the electric field profile ceases to increase extensively beyond 220 μm.

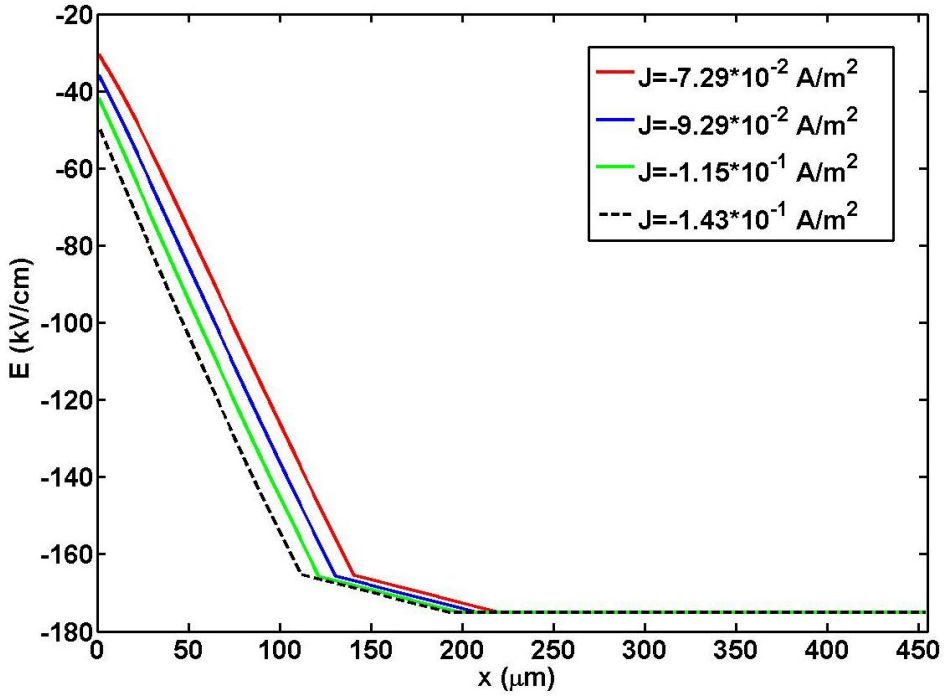

Figure 4.5. Calculated internal electric field profiles for the SiC2 sample at different current densities.

Upon increasing the applied bias, as revealed in Figure 4.5, the threshold for the trap-to-band ionization begins to be reached closer to the cathode and the "knee" in the spatial field distribution shifts to the left. As a result, while the electric field values below the knee increase, the spatial integral of the electric field beyond the knee has a relatively modest or incremental

change. The overall result is that increases in the voltage drop across the sample at biasing are significantly slower, while the current density rises quickly. The net effect is the rapid upswing in the *J-F* characteristic seen in Figure 4.1 beyond an average field of 130 kV/cm.

Although the simulations were in good agreement with the data (as shown in Figure 4.1) and were used to extract important parameters, it must be stressed that the values obtained are not entirely unique. Due to the relatively large number of parameters involved, it would be possible to obtain slightly different sets of values that could also yield a relatively close agreement with the steady-state *J-F* curve for the SiC sample. A sensitivity analysis could be carried out to determine the robustness of the results and to identify the model parameters that have the most significant effect on the electrical response. However, the intent here was more to develop a comprehensive physics-based model that would include a variety of processes and mechanisms spanning a large range of electric fields. Furthermore, since a simple one-dimensional model was used, a more rigorous and accurate two-dimensional approach would probably lead to slight differences in the parameter set needed to curve fit the data.

4.2.2 Electron-Irradiated SiC Samples

Simulations for the irradiated samples were also carried out to probe and understand the response. External irradiation by electron beam created traps in the material, with a goal of lowering the resistance, increasing the holdoff voltage, and lowering the device current throughput at any applied voltage. Such silicon carbide samples were denoted as SiC1. Current densities are expected to be much lower due to the higher trap densities caused by the 3.5 hour, 1 MEV electron irradiation. Results comparing the predictions from the simulations with experimental data are shown in Figure 4.6.

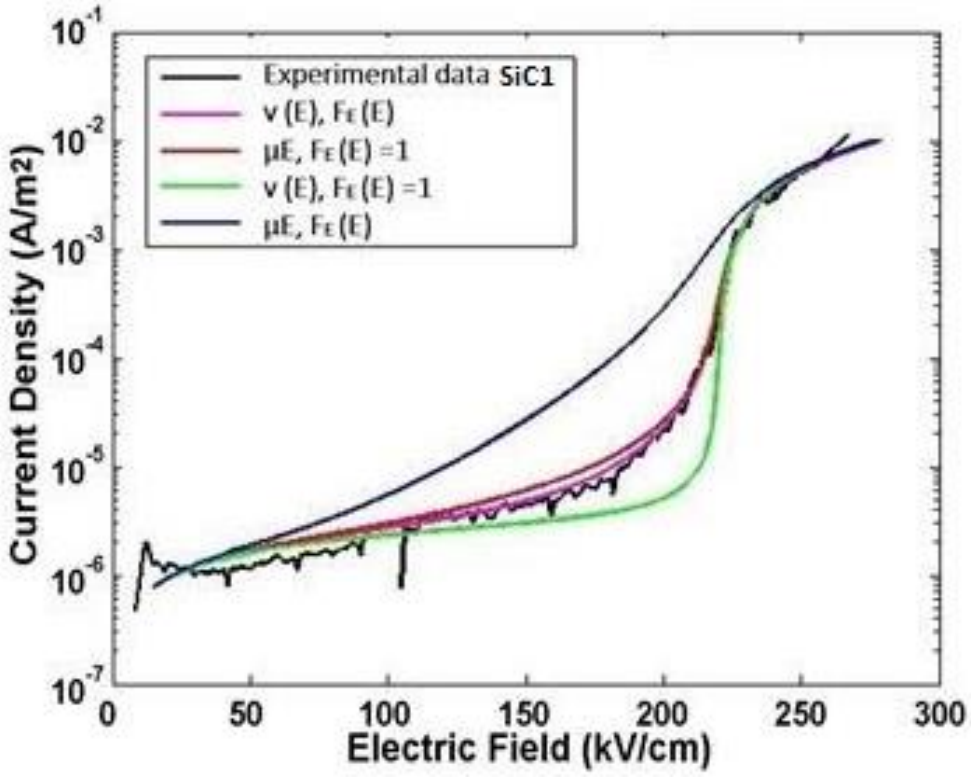

Figure 4.6. Comparison between the simulation *J-F* results and experimental data for semi-insulating 4H-SiC SiC1 sample subjected to the 1MeV irradiation. Simulation results were obtained for different cases, as discussed in the text.

Four different cases were simulated:

- Case 1 used *Velocity* = μF and $R_E(F) = 1$
- Case 2 used *Velocity* = μF and $R_E(F)$
- Case 3 used $v(F)$ and $R_E(F) = 1$
- Case 4 used $v(F)$ and $R_E(F)$

Thus, two of them used the full velocity-field characteristic of equation 3.24 as denoted by $v(F)$ in Figure 4.6, and two were obtained on a simpler mobility-based, linear $v(F) = \mu F$ characteristic. Additionally, two of the four calculations shown did not include field-dependent detrapping, and this was denoted by $R_E(F) = 1$, while the two remaining curves included this process were denoted by $R_E(F)$. Of the four simulation results, the plot that incorporated both a

field-dependent drift velocity and carrier detrapping (case 4) provided the best match with the data.

Figure 4.6 shows reasonably close agreement with the data for the SiC1 sample, based on two deep trap levels having energies E_{T1} and E_{T2} of 1.07 eV and 1.09 eV, respectively, below the conduction band edge. The corresponding densities used for the calculations were $N_{T1} = N_{T2} = 2.55\times10^{19}$ m^{-3}. Use of the simpler linear drift-velocity model without any high-field saturation resulted in excessively higher currents. Using the field dependent velocity alone was also not adequate. Without inclusion of carrier detrapping, along with the full velocity-field characteristics equation, the predicted currents were much lower than the observed data.

A significant feature for the irradiated sample SiC1 is the presence of a near-constant low-level current density of around 10^{-5} A/m^2 for fields below ~80 kV/cm. Electrically active defects are known to strongly enhance the leakage currents [147], and it has been speculated that trap-assisted tunneling [148, 149] can be an important transport process in such situations. Trap assisted tunneling (TAT) of electrons through a two-step process [150, 151] has previously been used to study the capture and emission times near interface traps [152] in ultrathin MOSFETs and erasable programmable read-only memories [153], and in gate dielectric stacks [154]. In addition, the multi-phonon tunneling process [155] can also be expected to be operative and can contribute to the leakage current at low voltages. In the present analyses for the SiC1 sample, both elastic trap-assisted-tunneling and the multi-phonon processes were included, using the theory described in detail in one of our previous reports [156]. The deep levels in the irradiated sample SiC1 facilitated electronic transfers to the semiconductor via the trap states. However, for SiC2, the shallow levels meant that a much larger tunneling distance would be needed, at any

given electric field, for the cathode Fermi level to be energetically lined up close to the trap, thereby facilitating the transition.

The present analysis shows that the main difference in the electrical response upon irradiation stems from the deep levels generated by the electron-beam bombardment. Though the trap densities for the irradiated SiC1 sample were not excessively large, a significant reduction in current, over the SiC2 sample, was nonetheless predicted. Furthermore, processes such as the trap-to-band ionization were found to be insignificant and played no role in shaping the *J-F* characteristic for the sample with deep traps. This is understandable, since much stronger electric fields would likely be required to produce the requisite high energy tail in the electron distribution function for impact ionization.

A final comment pertains to the phenomena of double-injection and bipolar transport which have been well studied in the past [157]. These processes are known to be associated with filamentary currents, instabilities, and S-shaped negative differential characteristics [158]. However, since such detrimental effects were not observed in the SiC samples, at least up to the ~11.5 kV voltage range studied, the prospect of double-injection and bipolar transport would appear to be improbable. Physically, the latter could arise from band-to-band impact ionization. However, this would seem unlikely since the SiC bandgap is too large to facilitate band-to-band impact ionization over the range of the electric fields applied in the experiments. A more rigorous and definitive assessment, though, would require calculations of the electron distribution function at the fields used here for SiC, either through the Monte Carlo or the Boltzmann schemes.

The possibility of hole-injection at the anode contact, which could be an alternative route to bipolar transport, requires that barrier heights at the contacts for electrons and holes are

roughly similar. In the situation of comparable barrier heights, electrons collected at the anode thermalize and exchange energy with the metallic reservoir. As a result, colder electrons in the metal contact could transition above the Fermi level by acquiring energy, and could effectively create a hole for injection back into the semiconductor. However, the barrier height for electrons (φ_{Bn}) has been reported to be in around 0.8 eV for Ohmic contacts [159], from which an estimate of ~2.5 eV can be made for the hole barrier height φ_{Bp}. Since these two values are quite dissimilar, hole injection at the contacts is unlikely for the SiC samples with Ohmic contacts. Nonetheless, as a simple test, forced hole injection was included into the simulations. The results (not shown) led to s-shaped negative differential *J-E* characteristics. Since this behavior is not observed in the experimental data, the presence of holes can be rejected.

4.3 Simulations with High-k Dielectrics and Metal Overhang in SiC Samples for Reduced Electric Field Profiles and Improved Reliability

An issue of increasing concern as power levels scale up is device reliability. In particular, recent work by Mauch et al. has shown crack formation in the SiC at the SiC/metal interface [21] in a variety of different device configurations and structures. It was hypothesized that the underlying cause of the observed cracks was either the result of large current densities at the SiC/metal interface during operation, which could then also led to localized hot spots, or the effect of high electric fields at the contact-SiC interface. Regardless of the origin, experimental optical microscope images confirm that the cracks form primarily near the surface and at points of greatest field enhancement [21].

It is clearly beneficial to be able to mitigate the peak electric fields, or at least re-shape their distribution towards greater uniformity with suppression of spatially localized peaks. Only

then can one achieve the full performance potential of SiC devices for high power applications. One specific aim in the context of the observed SiC failures would be to reduce the peak electric field values in the neighborhood of the metal-semiconductor interface with non-negligible carrier densities. Proper design of the edge terminations is necessary, in order to reduce the well-known field crowding at the edges. Toward this end, a combination of two strategies is proposed. The first makes use of an extension of the metal contact to shape the potential, an idea originally proposed in the context of silicon planar diodes [31]. The concept is similar to the field plates used to mitigate the IPE in GaN High Electron Mobility (HEMT) structures [32], which was also implemented in a number of other instances for GaAs- and GaN-based devices [35, 36]. The extension of metal contacts should reduce the maximum electric field by offering an extended surface for termination of the field lines, thus effectively spreading the electric field over a larger distance, instead of having a concentrated field flux at the end-tip of the metal contact.

Effectively, this would then lower the field crowding at the metal contact edge and modify the field distribution. It may be mentioned for completeness that the metal contact extensions would typically come at the cost of additional parasitic capacitance. Although this might be an issue for the frequency response of transistors or amplifiers, in the present context of a PCSS, this is of no relevance. Nonetheless, for completeness, the capacitances of all four structures shown in Figure 1.2 were calculated. The values were obtained to be 3.2 pF, 1.4 pF, 6.4 pF, and 10.3 pF for the configurations of Figures 1.2(a), 1.2(b), 1.2(c) and 1.2(d), respectively. As expected, the use of the high-*k* dielectric does increase the capacitance somewhat, but the values still remain fairly negligible.

The second feature involves the use of high-*k* dielectric materials to cover the surface of the SiC PCSS to further mitigate the fields and thus also to reduce any potential for localized

heating. A schematic (not to scale) of the proposed structure and simulated geometry is shown in Figure 1.2 (c). It consists of a thin HfO_2 layer acting as a high-*k* dielectric, with the metal in contact with the SiC and also present on the HfO_2 surface as an overhang. The basic PCSS dimensions and shape without any metal overhang or surface dielectric layer are shown in Figure 1.2 (a). The sizes chosen in the figure correspond to the devices tested in a recent report by Mauch et al. [21]. The figure shows a 300 nm thick Ni-doped SiC layer just below the contacts to reduce the contact resistance of the PCSS. Figure 1.2 (b) shows the use of a metal overhang on top of the SiC material, with the metal extension of length *L* at each side. Next, the use of a similar mesa-structure, but with HfO_2 as a high-*k* dielectric sandwiched between the metallic contact extension and the SiC bulk, is depicted in Figure 1.2 (c). An alternate structure employing HfO_2 is shown in Figure 1.2 (d). It is similar to that of Figure 1.2 (c), but the metal extensions lie over a thin HfO_2 layer that spans the entire length between the two electrodes.

The high-*k* dielectric can transmit or extract electric flux more efficiently. Hence, the peak fields (especially at the edges) can be expected to decrease due a combination of both the extended metal-plate overhang structure and the HfO_2 material. In addition, since HfO_2 is an insulator with a bandgap of about 5.5 eV, it presents a potential barrier to electronic transfer from SiC. Hence, carriers generated in SiC would be contained and possibilities of current flow and spillage into HfO_2 would be minimal. Furthermore, the higher bandgap of HfO_2, in comparison to SiC, would ensure that no photo-absorption would take place within the oxide dielectric layer. Other high-*k* dielectrics, inorganic materials such as PZT [$Pb(Zr_{0.53}Ti_{0.47})O_3$] and Barium Strontium Titanate were not considered since they could present potential problems associated with hysteresis. On the other hand, high-*k* materials such as HfO_2 or Ta_2O_5 are relatively hysteresis-free [36], and hence, HfO_2 was chosen for numerical evaluations.

It may seem that the use of a field plate merely changes the location of the high electric field point to the field plate edge. However, as seen from Figures 1.2 (c) and 1.2 (d), this would not create any problem. The terminating points at the plate edge lie over HfO_2 material. Hence, the use of a high-*k* dielectric will mitigate the high fields, since we are not simply proposing a field plate in itself, but rather the utilization of a high-*k* dielectric as well. Also, given the high bandgap of HfO_2, carrier generation would not occur in the HfO_2 material. Hence, the usual problems associated with regions of high currents and voltages, such as hot electron effects, impact ionization, electro-migration, etc. would not occur. Furthermore, the IPE would not be an issue in HfO_2 because of the non-crystalline nature of the material. The IPE requires cumulative build-up of electric fields, while the non-crystalline arrangement would work to randomize and destroy any cumulative and collective effects.

As part of this dissertation research contribution, calculations of electric field distributions in a SiC PCSS structure with metal contacts employing contact extensions on a high-*k* HfO_2 dielectric have been carried out, with the goal of assessing reductions in the peak electric fields. For completeness, analysis of thermal heating in a lateral PCSS structure with such modified geometries after photoexcitation is also included.

Results of simulations based on the COMSOL Multiphysics tool for electric field distributions in the OFF-state are discussed first. Figure 4.7 shows the electric field magnitude along the SiC surface between the anode and the cathode in the absence of any photoexcitation. Results for the device structure as shown in Figure 1.2 (a) are given first. The anode voltage was set at 10 kV. Two sharp peaks can be seen in Figure 4.7 (a); these occur at the ends of the two contacts facing each other. The magnitude is predicted to be quite large at about 7.5 MV/cm. In actual testing, as reported by Mauch et al. [21], voltages as high as 40 kV were applied in some

instances for testing. However, since this peak in Figure 4.7 (a) is concentrated at just a very small region, it might not necessarily lead to avalanching or breakdown since the total energy (which depends on the non-local path-integral of the overall electric field) has to reach levels above the ionization threshold for 4H-SiC. In addition, during the actual ON-state of the PCSS, the voltage drop across the load resistor would reduce the fields within SiC. However, the continued presence of high electric fields, even in the OFF-state, can be detrimental due to their potential for gradual defect creation. Thus, from a reliability standpoint, lowering peak fields, which could trigger slow degradation, becomes an essential precaution.

Results for the electric field with metal extensions of L=0.5 mm at both the anode and cathode ends on top of a t=4 μm thick SiC layer [as shown in Figure 1.2 (b)] are given in Figure 4.7 (b). Though the general trends and structure remain unchanged, the magnitudes are much lower. The peak field is now seen to have dropped down to about 3.2 MV/cm. However, with the use of a high-k HfO_2 dielectric layer of t=4 μm thickness and metal extensions of L=0.5 mm at both metal contacts, the electric field magnitude is predicted to drop down even further, to about 2.6 MV/cm. This is roughly at a 34.6% level (i.e., a 65.4% reduction) relative to the peak value of Figure 4.7 (a), and is quite significant.

It is thus expected that hot electron effects, possible IPE, as well as thermal heating and hot-spot generation can be significantly mitigated through the two-pronged strategy for the PCSS. Given that the use of a metal extension leads to field re-distribution and the mitigation of the peak magnitude, calculations were next performed to gauge the extent of this reduction with changes in length L and the thickness (t) of the HfO_2 (or SiC) layer immediately below the metal.

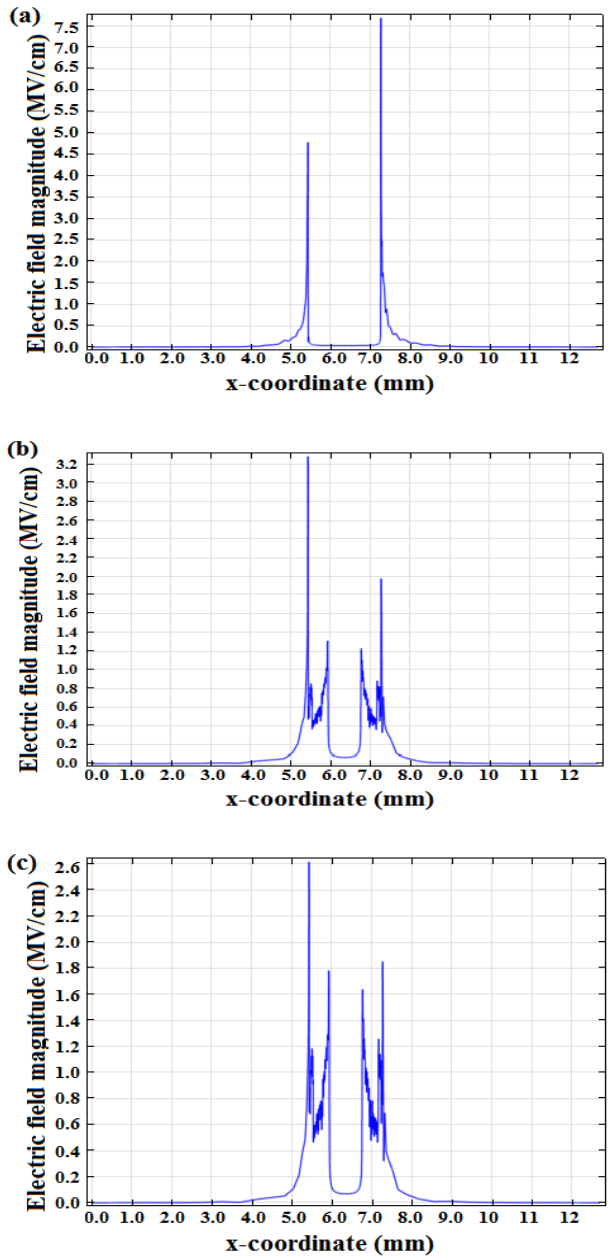

Figure 4.7. Electric field magnitude versus anode-cathode distance for different situations in the absence of any photoexcitation. A cathode-anode bias of 10 kV was applied. (a) The basic device structure, (b) mesa structure with metal extensions of L= 0.5 mm at both the anode and cathode ends on a 4 μm SiC layer, and (c) mesa structure having a 0.5 mm metal extension above a sandwiched HfO_2 layer.

Qualitatively, one expects the operable device voltage to increase with increasing of L as the electric field profiles are lowered. However, such lowering of the electric field profiles

cannot continue as the overhang lengths are continually reduced. With increased overhang, the anode-to-cathode distance shrinks. Hence, beyond a certain point, the electric field will begin to creep up and will start increasing past a local minima. Ideally, the overhang length corresponding to the minimum peak field would be the maximal extent of the metallic contacts. A secondary issue with regards to increasing the metal overhang is that any benefits of a reduced field magnitude come at the expense of lower optical throughput at the top surface. Reduced throughput lowers the electron-hole creation within the active SiC-PCSS structure, and hence the optical conversion efficiency.

Of additional interest is the role of thickness *t* and any optimization that might be made possible. An increase in thickness (*t*) can be expected to reduce the fields within the electrically active region of the device. However, a larger thickness of the under-layer (say HfO_2) below the metal could reduce the carrier drift velocities and collection efficiencies at the electrodes, since electric field penetration into the semiconductor falls off with distance. First, in principle, double-(or stepped) metal plate structures could perhaps be some of the more appropriate possibilities that could be attempted for field mitigation. However, such advanced strategies are expected to produce only incremental gain that would come at the expense of non-trivial increases in fabrication complexity. Hence, a study into such varied structures is beyond the present scope, and perhaps is not entirely warranted. Second, optical absorption leading to surface plasmon polaritons at the overhang would not efficiently transfer energy into the SiC. This is unlike the case of enhanced absorption by nanoparticle based plasmonic structures [160].

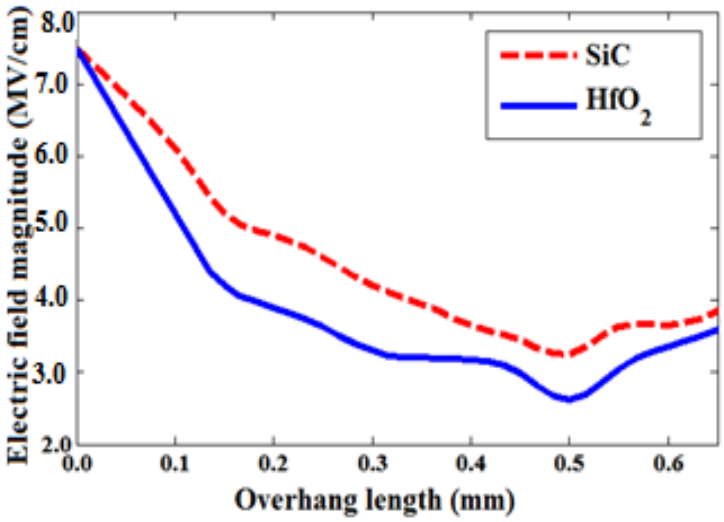

Figure 4.8. Results for the peak electric field magnitude as a function of the metal extension length *L*. The two plots shown correspond to the metal overhang above either SiC or HfO_2 as shown in Figure 1.2 (b) and 1.2(c). A thickness of t=4 μm below the metal overhang was chosen for both the SiC and HfO_2 calculations.

Figure 4.8 shows the results for the peak electric field magnitude as a function of the metal extension length *L*. The structures of Figures 1.2 (b) and 1.2 (c) were used, and a uniform mesa thickness of t=4 μm was chosen for these calculations. The two curves shown correspond to the metal overhang above SiC and HfO_2, respectively. From the figure, an initial drop in the peak electric field magnitude is seen to occur in both cases. But this is then followed by gradual increases roughly beyond 0.5 mm. So, from a practical standpoint, metal extensions of about L=0.5 mm at both the cathode and anode sides for this geometry and structure would be optimal. For HfO_2, the peak field is predicted to be reduced from roughly 7.5MV/cm down to 2.5 MV/cm, which is about 33% of the untreated structure.

Based on this result of an optimal length *L* of 0.5 mm for the case of a HfO_2 layer, variation of the fields with thickness *t* was probed next. However, for completeness, the two slightly different structures incorporating HfO_2 as shown in Figures 1.2(c) and 1.2 (d) were used. One had a HfO_2 layer of uniform thichness *t* spanning the entire length between the anode-to-

cathode, as in Figure 1.2 (d). The other consisted of a mesa-structure with the HfO_2 layer spanning only a distance *L* from each electrode as shown in Figure 1.2(c). Figure 4.9 reveals the peak electric field magnitudes as a function of the oxide thickness *t* for both cases. The result indicates that a uniform HfO_2 layer produces a fairly significant and consistent reduction in the peak electric field. As compared to the original untreated configuration, electric field strengths at only about ~34% are predicted. With the mesa structure, the plot of Figure 4.9 shows that HfO_2 is not as efficient at reducing the fields unless a thickness of at least 2.5 microns is employed. Given that a mesa design with a thicker HfO_2 layer would take longer to grow the oxide and would also involve more processing, the thin HfO_2 layer (say 0.5 μm) uniformly spaning the electrodes might be a better option. However, it must be pointed out that this electrostatic analysis did not include other possible effects, such as the formation of interface defects at the HfO_2-SiC interface or the band-bending normal to the interface that could occur. A complete analysis of such interfacial properties is beyond the present scope and would require approaches based on density functional theory [161,162].

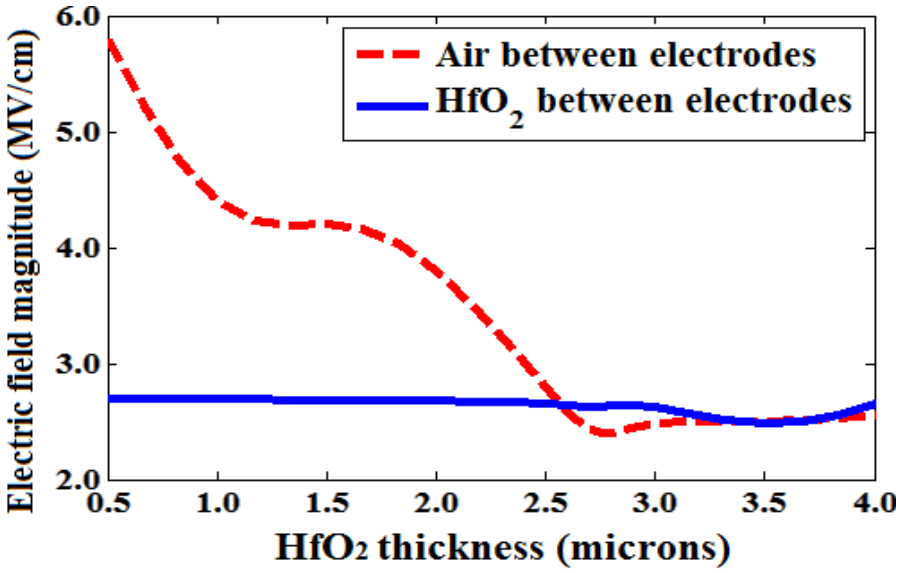

Figure 4.9. Peak electric field magnitudes as a function of the oxide thickness *t*. The two curves represent structures with the HfO_2 layer covering the entire region between the electrodes and a partial mesa coverage. A contact metal extension of L = 0.5 mm on each of the anode and cathode sides was used for both structures.

For completeness, the issue of device heating was studied to probe the potential for temperature increases in the modified structures. Only a limited number of studies have been devoted to the power dissipation and the thermal behavior of photoconductive switches [163, 164]. These have typically focused on high-power devices where thermal management poses challenges to the overall system design. A more recent report has also looked at heating in the metallization due to picosecond excitation pulses [165]. Calculations were performed for an electric pulse with duration that is typical for the SiC PCSS devices being used and tested within our group. The actual pulses have a rise time of about 2.5 ns and an ON time of ~6.5 ns, followed by an exponential decay. Here, an exponential decay time of 10 ns was assumed for the simulations, in keeping with the experiments. For these thermal calculations, the maximum average conductivity within the PCSS following photoexcitation was set at 3 S/m, in keeping with experimental measurements. This value can change somewhat depending on the incident photoexcitation flux or laser wavelength, but our choice represents a reasonable selection for conductivity based on data from several SiC PCSS samples. The aim was to compute the temperature profile within SiC at a 20 kV bias for the case of a metal overhang of length L = 0.5 mm with a uniform 0.5 μm HfO_2 layer extending between both electrodes.

A very simple and crude estimate of the temperature rise after an 8 ns time interval can be obtained from equation 3.35. Ignoring diffusive thermal transport at the nanosecond time scales, $\Delta T \sim Q\,(\Delta t)/[\rho\, C_p] = \sigma E^2(\Delta t)/[\rho\, C_p]$, where the power density source term is represented by σE^2. For values in the present SiC context: $\Delta T \sim 4.5\,(2x10^8)^2(8x10^{-9})/[3210x750] \sim$ 600K, which yields a net local temperature of about 900° K for a ~300° K ambient. This value is below the melting points of both the SiC (~3000° K) and the gold contacts (1330° K). Without the modified structures, the electric fields would have been much higher. However, in actual

practice, the use of the L = 0.5 mm metal overhang implies that laser generated electron-hole production in the SiC directly below the metal, and hence close to the contact with SiC, would be blocked off. Thus, over the ultrashort (~ns) time scales, values of the power density term Q near the contacts would actually be much smaller than the above estimate. The time interval for carrier drift across the 0.5 mm span below the metal extension, based on a saturation velocity of 10^5 m/s, is about 4.5 ns. Given the short duration (~8ns) of the overall laser pulse and the recombination centers deliberately incorporated in SiC to facilitate current decay and fast turn-off [21], the ~4.5ns delay associated with carrier drift to the metal-SiC edge is a fairly significant fraction (on the relevant nanosecond timescales) and should further help alleviate local heating.

Figure 4.10 shows the time evolution of the peak temperature across the SiC surface at a 20 kV bias with the L = 0.5 mm over a uniform 0.5 μm HfO_2 layer between electrodes. It may be pointed out that this calculation neglects the details of some of the physical processes, such as the emission and trapping dynamics, field-dependent ionization, contact injection via competing mechanisms, etc. In any case, the corresponding temperature distributions resulting from the numerical simulation were obtained at a 293° K ambient for the peak values over time, as given in Figure 4.10.

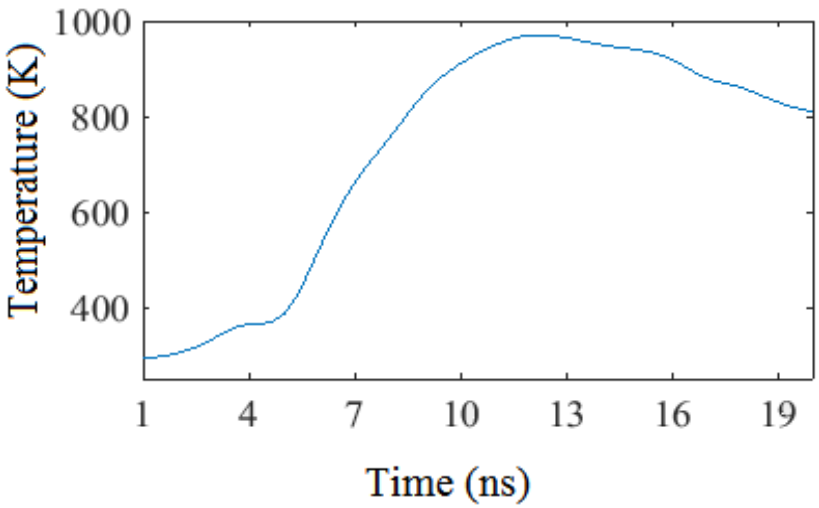

Figure 4.10. Calculated results of the peak temperature versus time in the PCSS at a 20 kV bias with L = 0.5 mm and a uniform 0.5 μm HfO_2 layer spanning between the electrodes.

The predicted temperature increase is seen to be about 980̊ K, and is well below the melting points for either SiC or gold. Thus, this result demonstrates that thermal heating for this modified structure should not cause excessive build-up of internal stresses or defects or other thermal degradation in the SiC PCSS.

CHAPTER 5

CONCLUSIONS AND SCOPE FOR FUTURE WORK

5.1 Concluding Summary

This dissertation presents an analysis of the steady-state, current-voltage response of semi-insulating 4H-SiC and calculations of electric field distributions within a SiC-based photoconductive switch with metal contacts employing contact extensions on a high-*k* HfO_2 dielectric.

In Chapter 1, an introduction of photoconductive switches and an outline of the dissertation objectives were given. Chapter 2 provides the background and a literature review. This chapter briefly discussed the theoretical principles of photoconductive switches, including characteristics of SiC material, classification of photoconductive switches, the transport in semi-insulation materials, and the other relevant issues for photoconductive switching, including single and double injection. In Chapter 3, the simulation methods used for the photoconductive switch analysis were presented, while Chapter 4 provided the results of those simulation models.

A model-based analysis of the steady-state, current-voltage response of semi-insulating 4H–SiC was carried out to probe the internal mechanisms and transport phenomena. Relevant physical processes, for example multiple defects, repulsive potential barriers to electron trapping, band-to-trap impact ionization, and field-dependent detrapping, were used for comprehensive numerical analyses. The objective was to make comparisons with available experimental data obtained from SiC samples with and without exposure to electron irradiation. The goals were to understand specific details of the observed *J-E* curve (e.g., variations in the slopes over different regimes) and to identify mechanisms over appropriate regimes potentially responsible for the

electrical conduction.

Results using the model matched the experimental data reasonably well over orders of magnitude variation in the current. A number of key parameters were also extracted in the process through comparing with the data. The measured results were explained in detail, with three comparatively shallow defects for the non-irradiated SiC sample, although some details, such as traps with a repulsive potential, field dependent emission, and trap-to-band ionization controlled by the local electric field, were required to explain the characteristics over the entire range sufficiently. For the irradiated sample, two deep traps were found to be necessary to fit the data, along with field-dependent emission. In addition, trap-assisted tunneling was found to be a vital process at low voltages. Moreover, for this case, impact ionization was shown to be insignificant, at least over the range of electric field values used in the experiments. However, this does not reduce the possibility of impact ionization, or even of hole-generation during an exposure of such photoconductive samples to low wavelength laser radiation. Finally, the possible presence of holes in the samples was rejected for the experimental voltage range. Though not shown here explicitly, results of our simulations with the forced inclusion of hole injection resulted in negative differential conductance. The possibility of hole conduction becomes unlikely, as this feature was not observed in the data.

Furthermore, calculations of electric field distributions within a SiC-based photoconductive switch were carried out to probe the effectiveness of strategies for mitigating the peak values, especially at the edges of metal contacts. Previous experimental reports on such SiC devices had shown a potential for device failure at the metal edges, due to field over-stressing. Two strategies were used in this calculation. Extended metal contacts were used to provide an extended surface for the termination of the field lines, and a high-*k* dielectric was

introduced and used above the bulk SiC. For completeness, analysis of thermal heating in a lateral PCSS structure with such modified geometries after photoexcitation was also included.

The simulation results show that peak electric fields, and hence the potential for device failure, can be mitigated by these strategies. A combination of the two approaches was shown to produce up to a ~67% reduction in peak fields. The reduced values were well below the threshold for breakdown in SiC material using biasing, as was found by other researchers. The field mitigation was shown to depend on the length of the metal overhang. For the device dimensions studied, this analysis suggests that using a HfO_2 cap layer as thin as 0.5 μm above the bulk SiC PCSS, together with a 0.5 mm metal extension, would be very effective. Though specific values for the metal extension and the HfO_2 layer thickness were obtained for a given device structure, the recipe is robust, so similar calculations could be carried out, as necessary, for obtaining the optimized values for other device sizes, in order to protect against field-related device failure. Finally, these calculations showed that, upon field mitigation, the internal temperature rise would also be controlled. A maximum value of 980 K was obtained here for an 8 ns electrical pulse at a 20 kV external bias. This is well below the limits for generating local stress or cracks or defects, thermal runaway associated with decreases in thermal conductivity with increasing temperature [74], or other deleterious high temperature effects [75].

5.2 Scope for Future Work

Based on the research work described in this dissertation, some of the other areas for further research and simulation aspects for future studies are briefly described as follows:

- Observing the transient behavior. This would open up the possibility to evaluate the 4H-SiC photoconductive switches.

- Carrying out two-dimensional (2-D) simulation for the steady-state. Since a simple one-dimensional model was used, a more rigorous and accurate two-dimensional approach would probably lead to slight differences in the parameter set needed to curve fit the data.
- Extending the 2D analysis to look at time-dependent decay in photocurrent that is probed by time-resolved microwave power reflectance (TRMPR) data. Such TRMPR measurements have been reported for SiC samples in the literature, and are available for comparison. Such a comparison would yield an independent assessment of trap energies and carrier lifetimes.
- Performing experimental measurements on SiC-based photoconductive switch with the extended metal contact and the high-*k* dielectric on top of bulk SiC. This would be the best way for confirmation of the COMSOL-based simulation results.

REFERENCES

[1] C. E. Weitzel, J. W. Palmour, C. H. Carter, Jr., K. Moore, K. J. Nordquist, S. Allen, C. Them, and M. Bhatnagar, *IEEE Trans. Electron Devices*, **43**, 1732, 1996.

[2] M.E.Levinshtein, S.L.Rumyantsev and M.S.Shur, *Properties of Advanced Semiconductor Materials*, Wiley – Interscience, 2001.

[3] R. J. Kumar, J. M. Borrego, R. J. Gutmann, J. R. Jenny, D. P. Malta, H. M. Hobgood, and C. H. Carter, Jr., *J. Appl. Phys.*, **102**, 013704, 2007.

[4] H. Morkoc¸, S. Strite, G. B. Gao, M. E. Lin, B. Sverdlov, and M. Burns, *J. Appl. Phys.*, **76**, 1363, 1994.

[5] G.M. Loubriel, F.J. Zutavern, A.G. Baca, H. P. Hjalmarson, T. A. Plut, W. D. Helgeson, O'Malley, M. H. Ruebush,, and D. J. Brown, *IEEE Trans Plasma Sci.* **25**, 124, 1997.

[6] D. Hashimshony, C. Cohen, A. Zigler, and K. Papadopoulos, "Switch opening time reduction in high power photoconducting semiconductor switches", *Opt. Lett.*, **124**, 443, 1996.

[7] D. H. Auston, "Picosecond optoelectronic switching and gating in silicon", *Appl. Phys. Lett.*, **26**, 101–103, 1975.

[8] G. J. Caporaso, Y.-J. Chen, and S. E. Sampayan, "The dielectric wall accelerator", *Rev. Accel. Sci. Technol.*, **2**, 1, 253–263, 2009.

[9] G. J. Caporaso, T.R. Mackie, S. Sampayan, Y. J. Chen, D. Blackfield, J. Harris, S. Hawkins, C. Holmes, S. Nelson, A. Paul, B. Poole, M. Rhodes, D. Sanders, J. Sullivan, L. Wang, J. Watson, P. J. Reckwerdt, R. Schmidt, D. Pearson, R.W. Flynn, D. Matthews, J. Purdy, "A compact linac for intensity modulated proton therapy based on a dielectric wall accelerator", *Phys. Med.*, **24**, 2, 98–101, 2008.

[10] J. R. Harris, D. Blackfield, G. J. Caporaso, Y.-J. Chen, S. Hawkins, M. Kendig, B. Poole, D. M. Sanders, M. Krogh, J. E. Managan, "Vacuum insulator development for the dielectric wall accelerator", *J. Appl. Phys.*, **104**, 2, 023301, 2008.

[11] J. W. B. Bragg, W. W. Sullivan, III, D. Mauch, A. A. Neuber, and J. C. Dickens, "All solid-state high power microwave source with high repetition frequency," *Rev. Sci. Instrum.*, **84**, 5, 054703, 2013.

[12] K. Shenai R. S. Scott B. J. Baliga, "Optimum semiconductors for high-power electronics", *IEEE Trans. Electron Devices* **36**: 1811-1823, 1989.

[13] M. Bhatnagar B. J. Baliga, "Comparison of 6H-SiC, 3C-SiC, and Si for power devices", *IEEE Trans. Electron Devices* **40**: 645-655, 1993.

[14] S. Dogan, A. Teke, D. Huang, and H. Morkoc, C. B. Roberts, J. Parish and B. Ganguly, M. Smith, R. E. Myers, and S. E. Saddow, "4H-SiC photoconductive switching device for use in high-power applications", *Appl. Phys. Lett.* **82**: 3107-3109, 2003.

[15] F. Zhao, M. M. Islam, P. Muzykov, A. Bolotnikov, and T. S. Sudarshan, *IEEE Electron Device Lett.* **30**, 1182, 2009.

[16] K. S. Kelkar N. E. Islam C. M. Fessler W. C. Nunnally, "Design and characterization of silicon carbide photoconductive switches for high field applications", *Journ. Appl. Phys.* **100**: 124905, 2006.

[17] N. Q. Zhang, B. Moran, S. P. Denbaars, U. K. Mishra, X. W. Wang, and T. P. Ma, *Phys. Status Solidi A* **188**, 213, 2001.

[18] K. Zhu D. Johnstone J. Leach Y. Fu H. Morkoc¸ G. Li B. Ganguly, "High power photoconductive switches of 4H SiC with Si3N4 passivation and n+-GaN subcontact, Superlattices and Microstructures", **41**: 264-270, 2007.

[19] For example, J. S. Sullivan and J. R. Stanley, *IEEE Trans. Plasma Sci*. **36**, 2528, 2008.

[20] For example, S. T. Pantelides, *Deep Centers in Semiconductors*, Gordon and Breach, New York/London, 1986.

[21] D. Mauch, W. Sullivan, III, A. Bullick, A. Neuber, and J. Dickens, ″High power lateral silicon carbide photoconductive semiconductor switches and investigation of degradation mechanisms,″ *IEEE Trans. Plasma Sci*., **43**, 2021-2031, 2015.

[22] K. Danno, D. Nakamura, and T. Kimoto, *Appl. Phys. Lett.*, **90**, 202109, 2007.

[23] G. Alfieri, E. V. Monakhov, B. G. Svensson, and M. K. Linnarsson, *J. Appl. Phys.*, **98**, 043518, 2005.

[24] M. A. Lampert P. Mark, in *Current Injection in Solids*, New York: Academic Press, 1970.

[25] A. Rose, *Phys. Rev.*, **97**, 1538, 1955.

[26] M. A. Lampert, A. Rose, and R. W. Smith, J. *Phys. Chem. Solids*, **8**, 464, 1959.

[27] N. F. Mott and R. W. Gurney, *Electronic Processes in Ionic Crystals*, Oxford University Press, London, 1940.

[28] N. Balkan (ed.), *Hot Electrons in Semiconductors Physics and Devices*, Oxford University Press, Oxford, 1998.

[29] A. A. Villanueva, J.A. del Alamo, T. Hisaka, K. Hayashi and M. Somerville, ″Degradation uniformity of RF power GaAs PHEMTs under electrical stress,″ *IEEE Transactions on Device and Materials Reliability*, **8**, 283-288, 2008.

[30] J. Joh, F. Gao, T. Palacios, and J. A. del Alamo, ″A model for the critical voltage for electrical degradation of GaN high electron mobility transistors,″ *Microelectronics Reliability*, **50**, 767-773, 2010.

[31] F. Conti and M. Conti, ″Surface breakdown in silicon planar diodes equipped with field plate,″ Solid State Electron., **15**, 93-105, 1972.

[32] D. Nagulapally, R. P. Joshi, and A. Pradhan, ″Simulation study of HEMT structures with HfO_2 cap layer for mitigating inverse piezoelectric effect related device failures,″ *AIP Advances*, **5**, pp. 017103/1-5, 2015.

[33] Y. Ando, Y. Okamoto, H. Miyamoto, T. Nakayama, T. Inoue, and M. Kuzuhara, *IEEE Electron Device Letters*, **24**, 289, 2003.

[34] A. Chini, D. Buttari, R. Coffie, S. Heikman, S. Keller and U. K. Mishra, *IET Electronics Letters*, **40**, 73, 2004.

[35] Y. F. Wu, A. Saxler, M. Moore, R. P. Smith, S. Sheppard, P. M. Chavarkar, T. Wisleder, U. K. Mishra, and P. Parikh, ″30 W/mm GaN HEMTs by field plate optimization,″ *IEEE Electron Device Letters*, **25**, pp. 117-119, 2004

[36] J. Shen, C.Y. Zhang, T.T. Xu, A.N. Jiang, Z.Y. Zhang, S. Wang, Q. Chen, ″Hysteresis-free HfO2 film grown by atomic layer deposition at low temperature,″ *Thin Solid Films*, **519**, pp. 7723-7726, 2011

[37] Beer, “Bestimmung der Absorption des rothen Lichts in farbigen Flüssigkeiten”, *Annalen der Physik und Chemie*, **86**, 78–88,1952

[38] C. H. Lee (ed), *Picosecond Optoelectronic Devices*, Academic Press Inc., Orlando, 1984.

[39] A. Rosen, F. J. Zutavern eds., *High Power Optically Activated Solid State Switches*, Artech House, Boston, 1994.

[40] G. Mourou, W. H. Knox, and S. Williamson, in *Picosecond Optoelectronic Devices*, edited by C. H. Lee (Academic, Orlando, 1984), pp. 219-248.

[41] M. C. Nuss and D. H. Auston, in *Picosecond Electronics and Optoelectronics II*, edited by F. J. Leonberger (Springer, New York, 1987), p. 72.

[42] J. Paslaski and A. Yariv, “Differential photoconductive sampling with a resolution independent of carrier lifetime”, *Appl. Phys. Lett.*, **55**, 1744-1746, 1989.

[43] D. Krokel, D. Grischkowsky, and M. B. Ketchen, "Subpicosecond electrical pulse generation using photoconductive switches with long carrier lifetimes", *Appl. Phys. Lett*., **54**, 1046-1048, 1989.

[44] M. Y. Frankel, S. Gupta, J. A. Valdmanis, and G. Mourou, "Picosecond pulse formation by transmission line discontinuities", *Electron. Lett.,* **25**, 1363-1365, 1989.

[45] Ximao Feng (2005), Photoexcitation and Photoionization of the Argon Atom and the Hydrogen Bromide Molecule (Doctoral dissertation, Western Michigan University). Reviewed from http://scholarworks.wmich.edu/dissertations

[46] A.Peled (ed), *Photo-Excited processes, diagnostics and applications*, Kluwer Academic Publishers, 2003.

[47] D. Vanmaekelbergh and L. van Pieterson, "Free Carrier Generation in Semiconductors Induced by Absorption of Subband-Gap Light", *Phys. Rev. Lett*., **80**, 821, 1998.

[48] J. G. Simmons and G. W. Taylor, Nonequilibrium "Steady-State Statistics and Associated Effects for Insulators and Semiconductors Containing an Arbitrary Distribution of Traps", *Phys. Rev*. B **4**, 502, 1971.

[49] Schmuttenmaer, Charles A. "Exploring Dynamics in the Far-Infrared with Terahertz Spectroscopy", *Chemical Reviews* **104** (4): 1759–1780, 2004.

[50] Nuss, Martin C.; Orenstein, Joseph "Terahertz time-domain spectroscopy". *Millimeter and Submillimeter Wave Spectroscopy of Solids*: 7–50, 1998.

[51] M. D. Pocha W. W. Hofer, High speed switching in photoconductors, in *High-Power Optically Activated Solid State Switches*, Eds.: A. Rosen and F. J. Zutavern, Chapter 3, Norwood: Artech House, 1994.

[52] R. L. Druce, W. W. Hofer, K. L. Griffin, J. H. Yee, G. H. Khanaka, and M. D. Pocha, "*Photoconductive Switching in Gallium Arsenide*," available from the National Technical Information Service, US department of Commerce, 5285 Port Royal Road, Springfield, VA 22161.

[53] R. P. Brinkman K. H. Schoenbach D. C. Stout V. K. Lakdawala G. A. Gerdin and M. M. Kennedy, "The Lock-on effect in electron-beam-controlled Gallium Arsenide switches", *IEEE Transactions on Electron Devices* **38**: 701-705, 1991.

[54] N. E. Islam, E. Schamiloglu, and C. B. Fleddermann, "Characterization of a semi-insulating GaAs photoconductive semiconductor switch for ultrawide band high power microwave applications", *Applied Physics Letters* **73**, 1988-1990, 1998.

[55] C. H. Lee, "Picosecond optoelectronic switching in GaAs", *Applied Physics Lett.* **30,** 84-86, 1977.

[56] M. D. Pocha R. L. Druce, “35-kV GaAs subnanosecond photoconductive switches”, *IEEE Trans. Electron Devices* **37**: 2486-2492, 1990.

[57] K. S. Kelkar N. E. Islam C. M. Fessler W. C. Nunnally, “Silicon carbide photoconductive switch for high-power, linear-mode operations through sub-band-gap triggering”, *Journ. Appl. Phys.* **98,** 093102, 2005.

[58] G. Mourou W. Knox, “High-power switching with picosecond precision”, *Appl. Phys. Lett.*, **35**: 492–495, 1979.

[59] W. C. Nunnally R. B. Hammand, “80-MW photoconductor power switch”, *Appl. Phys. Lett.* **44**, 980-982, 1984.

[60] P. K. Benicewicz A. J. Taylor, “Scaling of terahertz radiation from large-aperture biased InP photoconductors”, *Opt. Lett.* **18,** 1332-1334, 1993.

[61] T. Hattori, S. Arai, K. Tukamoto, “Ultrafast electron dynamics in GaAs and InP studied by time-resolved terahertz emission spectroscopy”, *J. Appl. Phys. Part 1*, **43,** 7546-7551, 2004.

[62] C. Baker, I. S. Gregory, W. R. Tribe, I. V. Bradley, M. J. Evans, M. Withers, P. F. Taday, V. P. Wallace, E. H. Lin- field, A. G. Davies, M. Missous, *Appl. Phys. Lett.* **83**, 4113, 2003.

[63] M. Suzuki M. Tonouchi, “Fe-implanted InGaAs terahertz emitters for 1.56 μm wavelength excitation”, *Appl. Phys. Lett.* **86**: 051104, 2005.

[64] J. Mangeney, L. Joulaud, P. Crozat, J.-M. Lourtioz, J. Decobert, *Appl. Phys. Lett.* **83**, 5551, 2003.

[65] F. Davanloo, C. B. Collins, and F. J. Agee, “High-Power Photoconductive Semiconductor Switches Treated With Amorphic Diamond Coatings”, *IEEE Transactions on Plasma Science*, **30**, 1897-1904, 2002.

[66] M. S. Mazzola et al. “GaAs photoconductive closing switches with dark resistance and microsecond conductivity decay”, *Appl. Phys. Lett.*, **54**: 20–22, 1989.

[67] M. S. Mazzola, K. H. Schoenbach, V. K. Lakdawala, and S. T. Ko, “Nanosecond optical quenching of photoconductivity in a bulk GaAs switch”, *Appl. Phys. Lett.*, **55**, 2102-04, 1989.

[68] M. S. Mazzola, K. H. Schoenbach, V. K. Lakdawala, and R. A. Roush, "Infrared quenching of conductivity at high electric fields in a bulk, copper-compensated, optically activated GaAs switch," *IEEE Trans. Electron Dev.* **37**, 2499-2505, 1990.

[69] K. Schoenbach R. Germer V. Lakdawala K. Schmitt S. Albin, “Concepts for electron-beam and optical control of bulk semiconductor switches”, *Proc. SPIE*, **735**: 85-94, 1987.

[70] K. H. Schoenbach, V. K. Lakdawala, R. Germer, and S. T. KO, "An optically controlled closing and opening semiconductor switch, " *J. Appl . Phys.* **63**, 2460-2463, 1988.

[71] F. J. Zutavern G. M. Loubriel M. W. O'Malley L. P. Shanwald W. D. Helgerson D. L. McLaughlin B. B. McKenzie, "Photo conductive semiconductor switch experiments for pulsed power applications", *IEEE Transactions on Electron* Devices **37**: 2472-2477, 1990.

[72] C. James C. Hettler J. C. Dickens, "Design and evaluation of a compact silicon carbide photoconductive semiconductor switch", *IEEE Transactions on Electron Devices* **58**: 508-511, 2010.

[73] W. C. Nunnally, "High Power Microwave Generation Using Optically Activated Semiconductor Switches", *IEEE Transactions on Electron* Devices **17** 2439, 1990.

[74] R.P. Joshi, P.G. Neudeck and C. Fazi, "Analysis of the temperature dependent thermal conductivity of silicon carbide for high temperature applications", *Journal of Applied Physics*, **88**, 265, 2000.

[75] V. M. Dwyer, A. J. Franklin, and D. S. Campbell, "Thermal failure in semiconductor devices", *Solid State Electronics* **33**, 553, 1990.

[76] S. M. Sze, *Physics of Semiconductor Devices*, 2nd edition, Wiley, New York, 1981.

[77] M. Bickermann, D. Hofmann, T. L. Straubinger, R., Weingartner, and A. Winnacker, "On the Preparation of V-Doped Semi-Insulating SiC Bulk Crystals," *Mat. Sci. Forum*, vols. **389-393**, 139-142, 2002.

[78] C.M. Zetterling and Institution of Electrical Engineers. "Process Technology for Silicon Carbide Devices". *Emis Processing Serie*s, 2. INSPEC, The Insti-tution of Electrical Engineers, 2002.

[79] S. P. Sheng M. G. Spencer X Tang P. Z. Zhou K. Wongchotigul C. Taylor G. L.Harris, "An investigation of 3C-SiC photoconductive switching devices", *Mater. Sci. Eng. B*, **46**: 147–151, 1997.

[80] A. A. Lebedev, "Deep level centers in silicon carbide: A review", *Semiconductors* **33**: 107-130, 1999.

[81] H. Matsunami, T. Kimoto, "Step-controlled epitaxial growth of SiC: High quality homoepitaxy", *Materials Science and engineering*, **20**, 3, 125-166, 1997.

[82] A. Powell, J. Jenny, S. Muller, H McDonald, V. Tsvetkov, R. Lenoard, and C. Carter Jr., *International Journal of High Speed Electronics and Systems* **16,** 751, 2006.

[83] M.Bickermann, D.Hofmann, T.L.Straubinger, R.Weingartner and A.Winnacker, "Preparation of semi-insulating Silicon Carbide by Vanadium doping during PVT bulk crystal

growth", Conference Proceedings of the 4th European Conference on Silicon Carbide and Related Materials, Linkoping, Sweden, September 2002.

[84] G. Pensl F. Ciobanu T. Frank M. Krieger S. Reshanov F. Schmid M. Weidner, "SiC material properties", *International Journal of High Speed Electronics and Systems*, **15**: 705 – 745, 2005.

[85] M. Bockowski, "Review: Bulk growth of gallium nitride: challenges and difficulties", *Crystal Research Technology*, **42**: 1162 – 1175, 2007.

[86] D. C. Look Z. Q. Fang B. Clafin, "Identification of donors, acceptors and traps in bulk – like HVPE GaN", *Journal of Crystal Growth*, **281**: 143–150, 2005.

[87] R. P. Vaudo X. Xu A. Salant J. Malcarne G. R. Brandes, "Characteristics of semi-insulating, Fe-doped GaN substrates", *Physica Status Solidi A*, **200**, 18–21, 2003.

[88] A. Y. Polyakov N. B. Smirnov A. V. Govorkov A. V. Markov S. J. Pearton N. G. Kolin D. I. Merkurisov V.M. Boiko C. R. Lee I. H. Lee, "Properties of Fe-doped, thick, freestanding GaN crystals grown by hydride vapor phase epitaxy", *Journal of Vacuum Science Technology B*, **25**: 436-442, 2007.

[89] W. Hwang and K. C. Kao, *Solid-St. Electron*, 15, 523, 1972.

[90] M. A. Lampert, "Simplified Theory of Space-Charge-Limited Currents in an Insulator with Traps", *Phys. Rev.* **103**, 1648, 1956.

[91] K. L. Ashley and A. G. Milnes, "Double Injection in Deep-Lying Impurity Semiconductors", *J. Appl. Phys.* **35**, 369, 1964.

[92] M. A. Lampert, "Double Injection in Insulators", *Phys. Rev.* **125**, 126, 1962.

[93] M. A. Lampert and A. Rose, "Volume-Controlled, Two-Carrier Currents in Solids: The Injected Plasma Case", *Phys. Rev.* **121**, 26, 1961;

[94] A. M. Barnett and A. G. Milnes, "Filamentary Injection in Semi-Insulating Silicon", *J. Appl. Phys.* **37**, 4215, 1966.

[95] B. K. Ridley, "Specific Negative Resistance in Solids", *Proc. Phys. Soc.*, **82**, 954-966, 1963.

[96] K. Aydin, V. E. Ferry, R. M. Briggs, H. A. Atwater, "Broadband polarization-independent resonant light absorption using ultrathin plasmonic super absorbers", *Nature Communications*, **2**, 517, 2011.

[97] J. He C. Fan J. Wang Y. Cheng P. Ding E. Liang, "Plasmonic nanostructure for enhanced light absorption in ultrathin silicon solar cells", *Advances in Optoelectronics*, **2012**: 592754, 2012.

[98] R. B. Dunbar T. Pfadler L. Schmidt-Mende, "Highly absorbing solar cells", *Optics Express A*, **20**: 177-189, 2012.

[99] R. E. A. Saleh and M. C. Teich, *Fundamentals of Photonics*, New York: Wiley, 1991.

[100] M. S. Unlu S. Strite, "Resonant cavity enhanced photonic devices", *Journ. Apl. Phys*. **78**: 607-639, 1995.

[101] K. Kishino M. S. Unlu J. I. Chyi J. Reed L. Arsenault H. Morkoc, *IEEE J. Quantum Electron*, **27**:, 2025-2034, 1991.

[102] E. Iverson and D. L. Smith, "Mathematical modeling of photoconductor transient response", *IEEE Transactions on Electron Devices* **34**, 2098-2107, 1987.

[103] C. T. Sah, L. Forbes, L. L. Rosier and A. F. Tasch, JR., "Thermal and optical emission and capture rates and cross sections of electrons and holes at imperfection centers in semiconductors from photo and dark junction current and capacitance experiments", *Solid State Electronics* **13**, 759-788, 1970.

[104] T. F. Boggess, JR., A. L. Smirl, S. C. Moss, I. W. Boyd and E. W. Vanstryland, "Optical limiting in GaAs", *IEEE J. Quantum Electron*, **21**, 488-494, 1985.

[105] G. C. Valley and A. L. Smirl, "Theory of transient energy transfer in gallium arsenide", *IEEE J. Quantum Electron*, **24**, 304-310, 1988.

[106] Y. P. Varshni, "Band to band radiative recombination in group IV, VI and III-V semiconductors(I)", *Physica Status Solidi*, **19**, 459-514, 1967.

[107] M. Takeshima, "Auger recombination in InAs, GaSb, InP ans GaAs", *J . Appl. Phys.*, **43**, 4114-4119, 1972.

[108] M. S. Demokan and M. S. Ozyazici, "High speed optoelectronic gallium arsenide switch triggered by mode locked laser pulses", *Int. J. Electronics*, **55**, 699-727, 1983.

[109] D. V. Lang and R. A. Logan, "A study of deep levels in GaAs by capacitance spectroscopy", *J. Electronic Mater.*, **4**, 1053-1066, 1975.

[110] G. F. Neumark and K. Kosai, "Deep levels in wide bandgap III-V semiconductors", *Semiconductor and Semimetals*, Academic Press Inc., **19**. 1-74, 1983.

[111] W. Maes, K. De Meyer and R. Van Overstraeten, "Impact Ionization in Silicon: A Review and Update", Solid-State Electronics, **33**, 6, 705-718, 1990.

[112] J. Bude, K. Hess, and G. J. Iafrate, “Impact ionization in semiconductors: Effects of high electric fields and high scattering rates”, *Physical Review B* **45**, 10958-10964, 1992.

[113] Kwan C. Kao, *Dielectric Phenomena in Solids: with emphasis on physical concepts of electronic processes*, Elsevier Academic Press, London, 2004.

[114] M. V. Fischetti, “Model for the generation of positive charge at the Si-SiO2 interface based on hot-hole injection from the anode”, *Phys. Rev*. **31**B, 2099, 1985.

[115] P. Samanta, “Calculation of the probability of hole injection from polysilicon gate into silicon dioxide in MOS structures under high-field stress”, *Solid-State Electronics*, **43,** 1677-1687, 1999.

[116] Yee-Chia Yeo, Qiang Lu, “MOSFET gate oxide reliability, Anode hole injection model and its applications”, *International Journal of High speed electronics and Systems*, **11**, 3, 2001.

[117] Kalus Schuegraf and Chenming Hu, “Hole Injection SiO2 Breakdown Model for very low voltage lifetime extrapolation”, *IEEE transactions on electron devices*, **41**, 5, 1994.

[118] Kalus Schuegraf and Chenming Hu, “Hole injection oxide breakdown model for very low voltage lifetime extrapolation”, **31**, *IEEE IRPS*, 7-12, 1993.

[119] G. H. Dohler and H. Heyszenau, *Phys. Rev. B* **12**, 641, 1975.

[120] C. Popescu and H. K. Henisch, *Phys. Rev. B* **14**, 517, 1976.

[121] R. H. Bube, *J. Appl. Phys.* **33**, 1733, 1962.

[122] Z. M. Li, S. P. McAlister, W. G. McMullen, C. M. Hurd, and D. J. Day, *J. Appl. Phys.* **67**, 7368, 1990.

[123] A. V. Dmitriev and A. B. Evlyukhin, *Semicond. Sci. Technol.*, **9**, 2056, 1994.

[124] S. Kang and C. W. Myles, *Phys. Status Solidi A* **181**, 219, 2000.

[125] N. Derhacobian and N. M. Haegel, *Phys. Rev. B* **44**, 12754, 1991.

[126] Willing and J. C. Maan, *J. Phys.: Condens. Matter* **8**, 7493, 1996.

[127] G. Lucovsky, *Solid State Commun*. **3**, 299, 1965.

[128] H. K. Sacks and A. G. Milnes, *Int. J. Electron*. **28**, 565, 1970.

[129] R. P. Joshi, *J. Appl. Phys.* **74**, 1810, 1993.

[130] M. Lax, *Phys. Rev.* **119**, 1502, 1960.

[131] L. Reggiani, L. Varani, V. V. Mitin, and C. M. Van Vliet, *Phys. Rev. Lett*. **63**, 1094, 1989.

[132] A. Palma, J. A. Lopez-Vianueva, and J. E. Carceller, *J. Electrochem. Soc.* **143**, 2687, 1996.

[133] J. Frenkel, "On Pre-Breakdown Phenomena in Insulators and Electronic Semi-Conductors", *Phys. Rev*., **54**, 647, 1938.

[134] Rosencher, V. Mosser, and G. Vincent, *Phys. Rev. B,* **29**, 1135, 1984.

[135] S. D. Ganichev, E. Ziemann, W. Prettl, I. N. Yassievich, A. A. Istratov, and E. R. Weber, *Phys. Rev. B,* **61**, 10361, 2000.

[136] L. Kamocsai and W. Porod, *J. Appl. Phys*. **69**, 2264, 1991.

[137] D. J. Robbins, *Phys. Status Solidi B,* **98**, 11, 1980.

[138] H. Lv, Y. Zhang, Y. Zhang, and L. A. Yang, *IEEE Trans. Electron Devices*, **51**, 1065, 2004.

[139] D.L. Scharfetter and H. K. Gummel, "Large-signal analysis of a silicon Read diode oscillator", *IEEE Transactions on Electron Devices*, **36**, 1, 64-77, 1969.

[140] W. P. Ballard and R. W. Christy, *J. Non-Cryst. Solids*, **17**, 81, 1975.

[141] Andreas Schenk, *Advanced Physical Models for Silicon Device Simulation,* Springer New York, 1998.

[142] M. Ieda, G. Sawa, and S. Kato, "A Consideration of Poole-Frenkel Effect on Electric Conduction in Insulators," *J. Appl. Phys*., **42**, 3737, 1971.

[143] W. Vollmann, "Poole-frenkel conduction in insulators of large impurity densities", *Phys. Stat. Sol*. **22**, A, 195, 1974.

[144] Oleg Mitrofanov and Michael Manfra, "Poole-Frenkel electron emission from the traps in AlGaN/GaN transistors", *J. Appl. Phys.* **95**, 6414, 2004.

[145] Gregg Guarino (2010), Finite Element Modeling and simulation of photoconductive and Ballistic semiconductor nanodevices (Doctoral dissertation, University of Rochester). Reviewed from http://www.lle.rochester.edu/media/publications/documents/theses/Guarino.pdf

[146] R. Menozzi, G. A. Umana-Membreno, B. D. Nener, G. Parish, G. Sozzi, L. Faraone, and U. K. Mishra, ″Temperature-dependent characterization of AlGaN/GaN HEMTs: thermal and

source/drain resistances,″ *IEEE Transactions on Device and Materials Reliability*, **8**, 255-264, 2008.

[147] J. Robertson, "High dielectric constant gate oxides for metal oxide Si transistors", *Rep. Prog. Phys*. **69**, 327, 2006.

[148] D. J. DiMaria and E. Cartier, "Mechanism for Stress-Induced Leakage Currents in Thin Silicon Dioxide Films", *J. App. Phys*. **78**, 3883, 1995.

[149] G. Jegert, A. Kersch, W. Weinreich, U. Schroder, and P. Lugli, *Appl. Phys. Lett*. **96**, 062113, 2010.

[150] A. Ghetti, M. Alam, J. Bude, D. Monroe, E. Sangiorgi, and H. Vaidya, *IEEE Trans. Electron Devices* **47**, 1341, 2000.

[151] X. R. Cheng, Y. C. Cheng, and B. Y. Liu, "Nitridation-enhanced conductivity behavior and current transport mechanism in thin thermally nitrided SiO_2", *J. Appl. Phys*. **63**, 797, 1988.

[152] A. Palma, A. Godoy, J. Jimenez-Tejada, J. Carceller, and J. Lopez-Villanueva, *Phys. Rev. B* **56**, 9565, 1997.

[153] J. Lee, G. Bosman, K. R. Green, and D. Ladwig, *IEEE Trans. Electron. Dev*. **49**, 1232, 2002.

[154] L. Vandelli, A. Padovani, L. Larcher, R. G. Southwick III, W. B. Knowlton, and G. Bersuker, *IEEE Trans. Electron. Devices* **58**, 2878, 2011.

[155] M. Herrmann and A. Schenk, "Field and high-temperature dependence of the long term charge loss in erasable programmable read only memories: Measurements and modeling", *J. Appl. Phys*. **77**, 4522, 1995.

[156] P. Maleeswaran, D. Nagulapally, R. P. Joshi, and A. Pradhan, *Journ. Appl. Phys*. **113**, 184504, 2013.

[157] M. A. Lampert and A. Rose, *Phys. Rev*. **121**, 26, 1961.

[158] W. H. Weber and G. W. Ford, "Space-charge recombination oscillations in double-injection structures," *Appl. Phys. Lett*. **18**, 241, 1971.

[159] S. Y. Han and J. L. Lee, "Effect of interfacial reactions on electrical properties of Ni contacts on lightly doped n-type 4H-SiC," *Journal of The Electrochemical Society*, **149**, G189-G193 2002.

[160] V. G. Kravets, S. Neubeck, A. N. Grigorenko, and A. F. Kravets, ″Plasmonic blackbody: Strong absorption of light by metal nanoparticles embedded in a dielectric matrix,″ *Phys. Rev. B*, **81**, pp. 165401/1-9, 2010

[161] Z. Wang, S. Tsukimoto, M. Saito, K. Ito, M. Murakami, and Y. Ikuhara, ″Ohmic contacts on silicon carbide: The first monolayer and its electronic effect,″ *Phys. Rev. B*, **80**, pp. 245303/1-12, 2009;

[162 X. T. Trinh, K. Szasz, T. Hornos, K. Kawahara, J. Suda, T. Kimoto, A. Gali, E. Janzen, and N. T. Son, ″Negative-U carbon vacancy in 4H-SiC: Assessment of charge correction schemes and identification of the negative carbon vacancy at the quasicubic site,″ *Phys. Rev. B*, **88**, pp. 235209/1-13, 2013.

[163] R. P. Joshi, P. Kayasit, N. Islam, E. Schamiloglu, C. B. Fledderman, and J. Schoenberg, ″Simulation studies of persistent photoconductivity and filamentary conduction in opposed contact semi-insulating GaAs high power switches,″ *J. Appl. Phys.*, **86**, pp. 3833-3843, 1999.

[164] P. Kayasit, R. P. Joshi, N. E. Islam, E. Schamiloglu, and J. Gaudet, ″Transient and steady state simulations of internal temperature profiles in high-power semi-insulating GaAs photoconductive switches,″ *J. Appl. Phys.*, **89**, pp. 1411-1417, 2001.

[165] B. Vermeersch, G. Pernot, H. Lu, J. H. Bahk, A. Gossard, and A. Shakouri, ″Picosecond Joule heating in photoconductive switch electrodes,″ *Phys. Rev. B*, **88**, p. 214302/1-7, 2013.

APPENDICES

VITA

Rajintha Tiskumara

Department of Electrical and Computer Engineering

Old Dominion University, Norfolk, VA

Email: rtisk001@odu.edu

Rajintha Tiskumara received her Bachelor degree in Physics from University of Peradeniya, Sri Lanka in 2010. She joined the Department of Physics at Old Dominion University in Norfolk, VA, USA as a graduate student in 2011 and completed her Masters degree in Physics in 2013. Rajintha began her PhD study in Department of Electrical and Computer Engineering at Old Dominion University in 2013.